Electroabsorption modulators used for all-optical signal processing and labelling

Xu, Lin; Jeppesen, Palle; Mørk, Jesper

Publication date:
2004

Document Version
Publisher's PDF, also known as Version of record

Electroabsorption modulators used for all-optical signal processing and labelling

Lin Xu
徐 林

Ph. D. thesis, November 2004

Research Center COM
Technical University of Denmark

The work presented in this thesis was carried out within the framework of the Danish Technical Research Council STVF (Statens Teknisk-Videnskabelige Forskningsråd) financed project SCOOP (Semiconductor COmponents for Optical signal Processing), which involves the company Intel Copenhagen ApS and the Optoelectronics and Systems Competence Areas at the Research Center COM, Technical University of Denmark.

Abstract

This thesis concerns the applications of semiconductor components, primarily electroabsorption modulators (EAMs), in optical signal processing and labelling for future all-optical communication networks.

An introduction to electroabsorption modulators is given and several mechanisms that form the basis of electroabsorption are briefly discussed including Franz-Keldysh effect, Quantum-Confined Stark Effect (QCSE) and Quantum-Confined Franz-Keldysh effect. QCSE is found to be more effective for absorption modulation than FKE at room temperature due to the quantum confinement of electrons and holes. Experimental investigations on electrical-to-optical (e/o) modulation of the EAM are presented. From the measured power transfer curves, static extinction ratios larger than 20 dB were obtained for wavelengths in the C-band. It is also shown that the insertion loss and static extinction ratio decrease with the signal wavelength, indicating that an optimum wavelength can be found as a trade-off between the on-off ratio and the signal-to-noise ratio. The chirp property and the small signal bandwidth for electrical-to-optical modulation of the EAM are investigated. It is found that the measured chirp α–parameter ranges from –0.4 to 0.8 depending on the reverse bias; the higher the bias, the smaller the chirp becomes. Negative chirp may be achieved by sacrificing the extinction ratio and the output power. The small signal bandwidth was measured to be as large as 24 GHz.

Cross absorption modulation (XAM) in an EAM is discussed including an introduction to the carrier effects and a simple model that simulates the carrier dynamics. Based on this model the static characteristics of an EAM under optical excitation are investigated theoretically; the results demonstrate the capability of an EAM used for wavelength conversion and 2R regeneration. The optical-to-optical (o/o) modulation bandwidth and frequency chirp are experimentally investigated. It is found that the o/o modulation bandwidth drastically depends on the quantum well depth while the e/o modulation bandwidth is mainly influenced by the electrical bonding pad size. A device having a small pad and shallow wells shows 24 GHz bandwidth for both e/o and o/o modulation. In the o/o chirp measurements very small chirp α–parameters are obtained. Depending on the operating wavelength and the bias the chirp α–parameter ranges from –0.6 to 0.2. It is also found that

higher bias voltages and shorter wavelengths are preferred to obtain a small or negative chirp α–parameter.

The principle of EAM-XAM based wavelength conversion is discussed and a wavelength conversion experiment at 40 Gb/s is presented. The influence of some operation parameters, including pump light power, reverse bias of the converter and probe light wavelength, is experimentally investigated for the wavelength-converted light, including its chirp performance. As a result of this investigation, a higher pump power (up to 20 dBm) and a relatively larger reverse bias (-2.5 V) are preferred for obtaining both larger extinction ratio and lower chirp of the converted signal. A multi-wavelength conversion scheme (8 × 40Gb/s) is demonstrated, where the receiver sensitivity for the back-to-back case is –33 dBm and the average power penalty for the eight converted channels is 9.2 dB. The best channel at 1555.7 nm has a power penalty of 8 dB. The wavelength dependence of the power penalty is explained by studying the impact of the extinction ratio and the average power of the converted signal on the Q parameter. Physical explanations for the optimum pump power and device length is given by considering impacts on the extinction ratio, average power and pulse width of the wavelength-converted signal. Other wavelength conversion schemes such as fibre-based cross phase modulation (XPM) and optical filtering, fibre-based Kerr switch, fibre-based four-wave-mixing (FWM) and semiconductor optical amplifier (SOA)-based cross gain modulation (XGM), are briefly discussed. As a result of the comparison, it is suggested that fibre-based solutions have relatively lower power penalties and have great potential for ultra-high speed operation while single semiconductor devices can so far operate at 40 Gb/s and are more attractive in terms of compactness, stability and integration. An important advantage of the EAM-based wavelength conversion scheme is that the frequency chirp of the converted signal is very small, which is desirable for long distance transmission and optical labelling systems.

An all-optical demultiplexing experiment from 160 Gb/s to 10 Gb/s using a single EAM with a very simple waveguide structure is presented. All 16 demultiplexed tributary channels are error free with an average receiver sensitivity of –25.3 dBm. An improvement of up to 6 dB in the receiver sensitivity by regeneration of the demultiplexed channel by an additional EAM acting as a saturable absorber is also demonstrated. A discussion of 2R regeneration based on a non-linear intensity transfer function is given. It is reiterated that a 2R regenerator can not reduce the

BER but can inhibit its accumulation. The non-linear transfer function of an EAM is frequency dependent and the main improvement from an EAM-based regenerator is the enhancement of the ER and the suppression of the noise in a space bit.

Applications of EAMs in optical label processing using various orthogonal labelling schemes are discussed.

Through EAM-based wavelength conversion label encoding and recognition are realised for two-level labelled signals consisting of a 10 Gb/s Amplitude Shift Keyed (ASK) payload and a 2.5 Gb/s Differential Phase Shift Keyed (DPSK) label. The receiver sensitivities for the payload/label in back-to-back case and after label encoding are –25.6/-28.1 dBm and –23.7/-21 dBm, respectively. Using an EAM for optical label insertion and a MZ-SOA for optical label erasure and payload regeneration in the ASK(10 Gb/s)/ Frequency Shift Keying (312 Mb/s) orthogonal modulation format, the complete functionality of a network node including two-hop transmission and all-optical label swapping is experimentally demonstrated. The cascaded transmission and label swapping result in 1.9 dB power penalty for the payload and 1.8 dB penalty for the label. Operating as external modulators, two EAMs are used to encode and erase the optical label in the return-to-zero (RZ)-DPSK/ASK and non-return-to-zero (NRZ)-DPSK/ASK format. We experimentally demonstrated label encoding, transmission over a 50 km SMF link, and label erasure of a 40 Gb/s RZDPSK modulated payload with an orthogonal 2.5 Gb/s ASK label. The penalties for the payload and label due to labelling and transmission are 4.5 dB and 2 dB, respectively. A similar experiment was carried out for a NRZDPSK/ASK labelled signal. Compared to the RZDPSK/ASK scheme, NRZDPSK/ASK has a smaller spectrum width and the labelling penalty for the payload is 2.7dB larger while the label performance is almost the same.

The modulation cross talk between the ASK payload and the DPSK label is theoretically analysed. As a result it is found that for a noiseless ASK/DPSK system with an infinite ASK extinction ratio, error free detection of the label can be obtained when the payload bit rate is at least 73 times larger than that of the label in case of balanced detection. For the single-ended DPSK receiver an even larger bit rate ratio (~130) is needed. Since real DPSK systems work at a relatively high bit rate this condition is normally not met. To solve this problem, instead of using a moderate ASK extinction ratio, we introduced a base band coding scheme named mark-insertion coding for the ASK payload and using this coding scheme

we realised label swapping based on a RZASK payload at 40 Gb/s and a DPSK label at 622 Mb/s using an EAM as the label swapper.

A new polarization modulation scheme is proposed and various signal-processing functions based on Polarization Shift Keying (PolSK) modulation format are demonstrated. Polarization modulation is implemented by a normal Mach-Zednder Modulator operating in a special but simple way. Detection and erasure of polarization information are realised by a device that is comprised of a polarization controller and a polarization beam splitter. A new orthogonal labelling scheme based on a 40 Gb/s DPSK payload and a 2.5 Gb/s PolSK label is proposed and experimentally demonstrated. The most striking feature of this new labelling format is that there is no modulation crosstalk between the payload and the label, in contrast with all previous orthogonal modulation formats. Swapping penalties are 0.15 dB and 0.6 dB for the payload and the label respectively. Penalties due to swapping and 40 km SMF transmission are 2.2 dB and 2.9 dB for the payload and the label respectively.

Abstract (in Danish)

Denne afhandling omhandler anvendelser af halvlederkomponenter, primært elektroabsorptionsmodulatorer (EAMs), til optisk signalbehandling og optisk mærkning i fremtidens optiske kommunikationsnetværk.

Der gives en introduktion til elektroabsorptionsmodulatorer og flere mekanismer, der ligger til grund for elektroabsorption, er kort beskrevet inklusive Franz-Keldysh effekt, Quantum-Confined Stark effekt (QCSE) og Quantum-Confined Franz-Keldysh effekt. Det vises, at QCSE er mere effektiv til absorptionsmodulation end FKE ved stuetemperatur på grund af kvanteindespærring af elektroner og huller. Eksperimenter med elektrisk til optisk (e/o) modulation af en EAM præsenteres. På grundlag af den målte effektoverføringskarakteristik opnås statistiske udslukningsforhold, som er større end 20 dB for bølgelængder i C-båndet. Det vises også, at både tab og udslukningsforhold mindskes ved mindre bølgelængden, hvilket indebærer, at en optimal bølgelængde kan findes som et kompromis mellem udslukningsforhold og signal-støj-forhold. Chirp egenskaberne og den lille signalbåndbredde for elektrisk til optisk modulation af EAMen er også undersøgt. Det vises, at den målte chirp a-parameter varierer mellem -0.4 og 0.8 afhængigt af forspændingen i spærreretningen; jo højere forspænding des mindre bliver chirp. Negativ chirp kan opnås ved at ofre dæmpningsforhold og udgangseffekt. Småsignal båndbredden blev målt til 24 GHz.

Krydsabsorptionsmodulation (XAM) i en EAM diskuteres inklusive en introduktion til ladningsbæreeffekter og en simpel model til simulering af ladningsbærerdynamik. På grundlag af denne model undersøges den statiske karakteristik af en EAM under optisk ekscitation; resultaterne viser, at en EAM er en mulig komponent til brug for bølgelængdeskift og 2R regenerering. Den optiske til optiske (o/o) modulationsbåndbredde og frekvenschirp undersøges eksperimentelt. Det vises, at o/o modulationsbåndbredden afhænger kraftigt af kvantebrøndsdybden, mens e/o modulationsbåndbredden hovedsageligt er influeret af den elektriske bondingkontakts størrelse. En komponent med lille bondingkontakt og lav kvantebrønd havde en båndbredde på 24 GHz for både e/o og o/o modulation. I o/o chirp målingerne observeres meget små a-parametre. Chirp a-parameteren variere mellem –0.6 og 0.2 afhængigt af bølgelængden. Det vises også, at højere forspænding og

kortere bølgelængde er at foretrække, når der ønskes en lille negativ chirp a-parameter.

Princippet bag EAM-XAM-baseret bølgelængdekonvertering diskuteres, og et bølgelængdekonverteringseksperiment ved 40 Gb/s præsenteres. Det bølgelængdekonverterede lys samt chirp-egenskaberne undersøges med hensyn til pumpelyseffekt, forspænding i spærreretningen af konverteren samt probelysets bølgelængde. Som resultat af disse undersøgelser vises det, at en højere pumpeeffekt (op til 20 dBm) og en relativ stor forspænding i spærreretningen (-2.5 V) skal benyttes for at opnå både stort udslukningsforhold og lavere chirp af det konverterede signal. Et multi-bølgelængde koncept (8 * 40 Gb/s) demonstreres, hvor modtagerfølsomheden i ryg-mod-ryg konstellation er 33 dBm og den gennemsnitlige strafeffekt for de otte konverterede kanaler er 9.2 dB. Den bedste kanal ved 1555.7 nm har en strafeffekt på 8 dB. Strafeffektens bølgelængdeafhængighed forklares ved at undersøge indflydelsen af udslukningsforhold og middeleffekt af det konverterede signal på Q-parameteren. Fysiske forklaringer på den optimale pumpeeffekt og komponentlængde gives ved at betragte indvirkningen af udslukningsforhold, middeleffekt og pulsbredde af det bølgelængdekonverterede signal. Andre eksempler bølgelængdekonvertering beskrives kort, såsom fiberbaseret krydsfasemodulation (XPM) efterfulgt af optisk filtrering, fiberbaseret Kerr-switching, fiberbaseret firebølgeblanding (FWM) og krydsforstærknings modulation i en halvleder optisk forstærker (SOA). Resultatet af sammenligningen viser, at fiberbaserede løsninger har relativt små strafeffekter og stort potentiale for ultra-højhastigheds funktion, mens halvlederkomponenter kan fungere op til 40 Gb/s og er mere attraktive med hensyn til stabilitet, størrelse og integration. En vigtig fordel ved EAM-baseret bølgelængdekonvertering er, at chirpen af det konverterede signal er lille, hvilket er ønskeligt ved langdistance transmission og i systemer med optisk mærkning.

Et optisk demultipleksnings eksperiment fra 160 Gb/s til 10 Gb/s baseret på en EAM med en meget simpel bølgelederstruktur præsenteres. Alle 16 demultipleksede kanaler er fejlfri med en gennemsnitlig modtagerfølsomhed på –25.3 dBm. En forbedring på op til 6 dB i modtagerfølsomhed ved regenerering af de demultipleksede kanaler er også vist ved at benytte en ekstra EAM, der fungerer som en mætbar absorber. En diskussion af 2R regenerering baseret på en ulineær effektoverføringskarakteristik gives. Det benyttes, at en 2R regenerator ikke kan reducere BER, men kan forhindre akkumulation af yderligere

fejl. Den ulineære overføringskarakteristik af EAMen er frekvensafhængig, og den største forbedring fra en EAM-baseret regenerator er forøgelsen af udslukningsforholdet samt undertrykkelsen af støj i nul-bit.

Anvendelsen af EAMer til optiske mærkningsprocesser ved hjælp af forskellige ortogonale mærkningsmetoder diskuteres.

Gennem bølgelængdeskift baseret på en EAM, realiseres mærkningskodning og -genkendelse for signaler, som er mærkede i to niveauer bestående af en 10 Gb/s Amplitude Shift Keyed (ASK) nyttelast og et 2,5 Gb/s Differential Phase Shift Keyed (DPSK) mærke. Modtagerens følsomhed for både nyttelast og mærke i ryg-mod-ryg konstellation og efter mærkningskodning er henholdsvis –25,6 / -28,1 dBm og –23,7 / -21 dBm. Ved brug af en EAM til at indsætte et optisk mærke og en MZ-SOA til at slette mærket igen og til at regenerere nyttelasten af det ortogonale ASK (10 Gb/s) / Frequency Shift Keying (FSK) modulationsformat, er den komplette funktionalitet af et netværksknudepunkt blevet demonstreret eksperimentelt, inklusive to-hop transmission og udskiftning af det optiske mærke. Den dobbelte transmission og mærkeskiftet giver 1,9 dB i strafeffekt for nyttelasten og 1,8 dB strafeffekt for mærket. Ved at bruge dem som eksterne modulatorer, er to EAMer brugt til at kode og slette det optiske mærke i formaterne return-to-zero (RZ)-DPSK/ASK og non-return-to-zero (NRZ)-DPSK/ASK. Vi demonstrerer eksperimentelt mærknings kodning, transmission over et 50 km langt SMF link, og mærkningssletning for en 40 Gb/s RZDPSK moduleret nyttelast med et ortogonalt moduleret 2,5 Gb/s ASK mærke. Strafeffekterne for nyttelast og mærke grundet mærkning og transmission er henholdsvis 4,5 dB og 2 dB. Et lignende eksperiment blev foretaget for et NRZDPSK/ASK mærket signal. Sammenlignet med RZDPSK/ASK løsningen, har NRZSPSK/ASK et smallere spektrum og strafeffekterne for nyttelasten er 2,7 dB større, medens mærkets opførelse er næsten den samme.

Modulations krydstalen mellem ASK nyttelast og DPSK mærke er analyseret teoretisk. Som resultat er det fundet, at for et støjfrit ASK/DPSK system med uendelig stort ASK udslukningsforhold, kan man opnå fejlfri detektion, når nyttelastens bit hastighed er mindst 73 gange større end mærkets bit hastighed, og når man bruger balanceret detektion. Hvis man bruger en enkelt arm i DPSK modtageren, kræves der et endnu større bit hastigheds forhold. Da virkelige DPSK systemer arbejder med en relativt høj bit hastighed, er denne betingelse sjældent opfyldt. For at løse dette problem, indførte vi ASK nyttelasten - i stedet

for et moderat ASK udslukningsforhold - et basisbånds kodningsformat kaldet mark-indsættelses kodning. Ved brug af dette kodningsformat samt en EAM som mærkeskifter, opnåede vi mærkeskift for en RZASK nyttelast på hastigheden 40 Gb/s og et DPSK mærke ved 622 Mb/s.

En ny polarisations modulations metode er foreslået, og forskellige funktioner indenfor signalbehandling baseret på Polarization Shift Keying (PolSK) modulations formatet er demonstreret. Polarisations modulationen blev tilvejebragt med en normal Mach-Zehnder modulator, som dog udnyttes på en speciel, men simpel måde. Detektion og sletning af polarisations informationen er gennemført ved hjælp af en komponent, hvori der indgår en polarisations kontrol og en polarisations stråle deler. Et nyt ortogonalt mærknings system baseret på en 40 Gb/s DPSK nyttelast og et 2,5 Gb/s PolSK mærke er foreslået og demonstreret eksperimentelt. Det mest overraskende ved dette mærknings format er, at der ikke er nogen modulations krydstale mellem nyttelast og mærke, i modsætning til alle tidligere modulationsformater. Strafeffekter hidrørende fra udskiftning af mærke er henholdsvis 0,15 dB og 0,6 dB for nyttelast og mærke. Strafeffekter hidrørende fra udskiftning af mærke og transmission gennem 40 km SMF er henholdsvis 2,2 dB og 2,9 dB.

Resumé

Lin Xu was born in Chongqing, China on January 18, 1975. He received the B.Sc. and M.Sc. degrees in electrical engineering from Beijing University of Posts and Telecommunications, Beijing, China in 1996 and 1999, respectively. From 1999-2001 he was a project manager of submarine cable systems at the International Cable Department of China Telecom where he took part in the international submarine cable project APCN2 (Asia Pacific Cable Network 2). In the autumn of 2001 he began to pursue the Ph.D. degree at the Research Center COM, Technical University of Denmark, Lyngby, Denmark, within the framework of the STVF (Statens Teknisk-Videnskabelige Forskningsråd) financed project SCOOP (Semiconductor COmponents for Optical signal Processing). This Ph.D. project involved system investigations of newly developed semiconductor devices for optical communications, and was completed in November 2004.

Resumé (in Danish)

Lin Xu blev født I Chongqing, Kina, den 18. Januar 1975. Han fik sin B.Sc. og M.Sc. titler som elektrisk ingeniør fra Beijing University of Posts and Telecommunications, Beijing, Kina, henholdsvis i 1996 og 1999. Fra 1999 til 2001 var han projekt ledere af systemer af undervands kabler ved det internationale undervands projekt APCN2 (Asia Pacific Cable Network 2). I efteråret 2001 begyndte han at læse til en Ph.d. grad ved Research Center COM, Dansk Tekniske Universitet, Lyngby, Danmark, omkring det STVF (Statens Teknisk-Videnskabelige Forskningsråd) finansieret projektet SCOOP (Semiconductor COmponents for Optical signal Processing). Hans Ph.d. projekt omhandler systemforskning af nyt udviklet semiconductor componenter for optisk kommunikation, og var afsluttet i November 2004.

Preface

This Ph.D. project was initiated in 2001 and completed in 2004. In this period a large number of persons have contributed to my work in many ways, to whom I am full of gratitude.

First of all, I wish to thank my supervisors Palle Jeppesen, Jesper Mørk and Leif K. Oxenløwe for the opportunity they provided and for their considerate guidance, patient teaching and encouragement.

I am very grateful to all my colleagues in the SCOOP project, Jørn Hvam, Sune Højfeldt, Francis Romstad, Andrea Tersigni, Filip Öhman, and Svend Bischoff for close teamwork and inspiring discussions. Special thanks are due to Kresten Yvind and Lotte J. Christiansen for supplying various devices that were used in most of my experiments. I would also like to thank Jesper Hanberg and Karsten Hoppe at Intel Copenhagen ApS.

I appreciate the help of my colleagues at the System Competence Area, Anders T. Clausen, Christophe Peucheret, Torger Tokle, Jorge Seoane, Andrei Siahlo, Pablo V. Holm-Nielsen, Kim S. Berg, Peter Andreas Andersen, Beata Zsigri, Darko Zibar and Michael Galili, with whom I have enjoyed and benefited from extensive and fruitful collaborations.

I would also like to acknowledge Lone Bjørnstjerne, Janne Witt Bengtsen and Aline Møller for helping me with all kinds of untechnical issues.

Finally, my sincere thanks go to my compatriots and friends, Haiyan Ou, Chi Zhang, Li Chang, Yitao Ren, Yan Guo, Jianfeng Zhang, Yan Geng, Kun Gao, Xu Peng, Wenzhong Shen, Hongwen Li and Hongyuan Cheng for their generous and considerate help to my family and for the happy time we had together.

Lin Xu
November 2004

此书三载成

文林著其名

致恩敬双亲

吾念长兄情

妻功当居首

儿立学尊行

Ph.D. publications

I. N. Chi, L. Xu, L. K. Oxenløwe, T. Tokle and P. Jeppesen, " 2R regenerator based on high non-linear dispersion-imbalanced loop mirror ", *Optics Communications*, Issue 206/4-6 pp. 295-300, 2002

II. L. Xu, N. Chi, J. Mork, L.K. Oxenlowe and P. Jeppesen, "Precise measurement of EAM chirp α-parameter and theoretical analysis of effective chirp under large signal modulation", *International Conference on Telecommunications 2002*, paper A013.

III. Nan Chi, Lin Xu, Kim S. Berg, Torger Tokle and Palle Jeppesen, "All-optical Wavelength Conversion and Multi-channel 2R Regeneration Based on Highly Nonlinear Dispersion-Imbalanced Loop Mirror", *IEEE Photonics Technology Letters*, Vol. 14, No. 11, pp. 1581-1583, 2002.

IV. L. Xu, L.K. Oxenløwe, N. Chi, J. Mørk, P. Jeppesen, K. Hoppe and J. Hanberg, "Experimental characterisation of wavelength conversion at 40Gb/s based on electroabsorption modulators", *IEEE Lasers and Electro-Optics Society 2002,* paper MM3.

V. L. Xu, L.K. Oxenløwe, N. Chi, F. P. Romstad, K. Yvind, J. Mørk, P. Jeppesen, K. Hoppe and J. Hanberg, "Bandwidth and chirp characterisation of wavelength conversion based on electroabsorption modulators", *European Conference on Optical Communication 2002*, paper P1.26.

VI. N. Chi, L. Xu, L. Chritiansen, K. Yvind, J. Zhang, P. Holm-Nielsen, C. Peucheret, C. Zhang, P. Jeppesen, "Optical label swapping and packet transmission based on ASK/DPSK orthogonal modulation format in IP-over-WDM networks", *Optical Fiber Communication Conference and Exposition 2003*, paper FS2, 2003.

VII. N. Chi, J. F. Zhang, P. V. Holm-Nielsen, L. Xu, I. T. Monroy, C. Peucheret, K. Yvind, L. J. Christiansen, P. Jeppesen, "Experimental demonstration of cascaded transmission and all-optical label swapping of orthogonal IM/FSK labelled signal", *IEE Electronics Letters*, Vol. 39, No. 8, pp. 676-678, 2003.

VIII. J. Mork, L. Oxenlowe, S. Hojfeldt, F. Romstad, K. Yvind, L. Xu, F. Ohman, L. J. Christiansen, A. Tersigni, K. Hoppe, M. Lobel, and J. Hanberg, "Optical signal processing using electro-absorbers", *Proc. ECIO'03 - 11th European Conference on Integrated Optics, Prague, Czech Republic,* April 2003 (invited).

IX. L. Xu, N. Chi, L.K. Oxenløwe, K. Yvind, J. Mørk, P. Jeppesen and J. Hanberg, "Optical label encoding using electroabsorption modulators and investigation of chirp properties", *Journal of Lightwave Technology*, Vol. 21, No. 8, pp. 1763-1769, 2003

X. N. Chi, C. Mikkelsen, L. Xu, J.F. Zhang, P.V. Holm-Nielsen, H.Y. Ou, J. Seoane, C. Peucheret, P. Jeppesen, "Transmission and label encoding/erasure of

orthogonally labelled signal using 40 Gbit/s RZ-DPSK and 2.5 Gbit/s IM label", *IEE Electronics Letters*, Vol. 39, No. 18, pp. 1335-1337, 2003.

XI. N. Chi, L. J. Christiansen, P. Jeppesen, I. T. Monroy, P. V. Holm-Nielsen, C. Peucheret, K. Yvind, L. Xu, J. Zhang, "Optical label switching in telecommunication using semiconductor lasers, amplifiers and electro-absorption modulators," in *Laser Optics'2003*, paper WeR3-05, St.Petersburg, Russia, 2003

XII. L. Xu, N. Chi, L.J. Christiansen, K. Yvind, L.K. Oxenløwe, J. Mørk and P. Jeppesen, "160 to 10 Gb/s all-optical demultiplexing using a single electroabsorption modulator", *European Conference on Optical Communication 2004*, paper We1.5.3, 2004.

XIII. L. Xu, N. Chi, K. Yvind, L.J. Christiansen, L.K. Oxenløwe, J. Mørk, P. Jeppesen and J. Hanberg, "7 × 40 Gb/s base-rate RZ all-optical broadcasting utilizing an electroabsorption modulator", *Optics Express*, vol. 12, No. 3, pp. 416-420, 2004.

XIV. L. Xu, N. Chi, K. Yvind, L.J. Christiansen, L.K. Oxenløwe, J. Mørk, P. Jeppesen and J. Hanberg," 8×40 Gb/s RZ all-optical broadcasting utilizing an electroabsorption modulator", *Optical Fiber Communication Conference and Exposition 2004*, paper MF71, 2004.

XV. L. J. Christiansen, L. Xu, K. Yvind, F. Öhman, L. Oxenløwe, and J. Mørk, "2R Regeneration in Concatenated Semiconductor Optical Amplifiers and Electroabsorbers", *European Conference on Optical Communication 2004*, paper Mo3.4.3, 2004.

XVI. N. Chi, L. Xu, J.F. Zhang, P. V. Holm-Nielsen, C. Peucheret, C. Mikkelsen, H. Ou, J. Seoane, P. Jeppesen, "Orthogonal optical labeling based on a 40 Gbit/s DPSK payload and a 2.5 Gbit/s IM label", *Optical Fiber Communication Conference and Exposition 2004*, paper FO6.

XVII. N. Chi, P. V. Holm-Nielsen, L. Xu, J. F. Zhang, T. Tokle, and P. Jeppesen, "Cascaded transmission, packet switching and all-optical wavelength conversion for a 40 Gb/s RZ payload with a 10 Gb/s serial-bit label", to be published in *Electronics Letters*.

XVIII. N. Chi, L. Xu, J. F. Zhang, P. V. Holm-Nielsen, C. Peucheret and P. Jeppesen, "Optical Label Switching of 40 Gb/s Payloads Using Orthogonal ASK/DPSK Modulation Format", submitted to *J. Lightwave Technol*.

XIX. N. Chi, L. Xu, J. F. Zhang, P. V. Holm-Nielsen, C. Peucheret, Y. Geng and P. Jeppesen, "Transmission and Optical Label Swapping for 4x40 Gb/s WDM signals deploying orthogonal ASK/DPSK labeling", submitted to IEEE *Photonics Technology Letters*.

XX. L. Xu, N. Chi, L.K. Oxenløwe, J. Mørk, and P. Jeppesen, "A new orthogonal labelling scheme based on a 40 Gb/s DPSK payload and a 2.5 Gb/s PolSK label", submitted to IEEE *Photonics Technology Letters*.

Contents

1

Introduction

The thirst for information and the need to “always be connected” is spawning a new era of communications. This new era will drive the need for higher bandwidth technologies in order to keep pace with increasing processor performance, driven by Moore's Law. The solution is optical communications that potentially have a bandwidth of about 15 THz. With the rapid developments in the last decade of the twentieth century optical communications has become a field that impacts everyone on the earth. It is the tie that today binds us together better than any previous age.

The development of fibre-based telecommunication systems in the 1990’s focused on increasing their transmission capacity. This was done first by increasing the signal modulation speed from 155 Mb/s to 622 Mb/s, to 2.5 Gb/s and then 10 Gb/s, finally to 40 Gb/s, today’s modulation speed. Since it is impossible for a single-wavelength laser to utilize the enormous bandwidth provided by optical fibres, multiple single-wavelength laser transmitters are typically multiplexed and transmitted on a single fibre. This scheme, which was developed in the mid 1990’s, is called Wavelength-Division-Multiplexing (WDM). A triple-band Dense-WDM (DWDM) optical communication system with 273 wavelengths covering S- (1491.88-1529.55 nm), C- (1529.94-1569.59 nm) and L- (1570.01-1611.79 nm) bands, where each wavelength carries 40 Gb/s data and is transmitted over a fibre link of 117 km, has been demonstrated [1]. Thus, the total transmission capacity of a single fibre reaches 10.9 Tb/s.

Optical time division multiplexing (OTDM) provides another way of increasing the capacity of transmission systems. The individual data channels at the base rate (e.g., 10 Gb/s) are at the same wavelength and separated in time. They are interleaved to form a high bit rate data stream. The use of higher channel bit rates is expected because of the significant reduction in WDM channel count, terminal footprint, and power consumption. The reported capacity record of a single-wavelength OTDM transmission system was 1.28 Tb/s [2]. In this demonstration optical

pulses had widths of about 250 fs and the line bit rate was achieved by fibre-based time interleaving from a base rate of 10 Gb/s up to 640 Gb/s and then by polarization multiplexing from 640 Gb/s to 1.28 Tb/s.

A combination of WDM and OTDM is expected to make a more cost-effective use of the bandwidth provided by fibres. Employing the forward error correction (FEC) and hybrid Er-doped fibre amplifier (EDFA)/Raman amplifiers, 3.2 Tb/s (40 × 80Gb/s) transmission over 1000 km [3] has been achieved. As for even higher channel bit rates, 19 × 160 Gb/s [4] and 10 × 320 Gb/s [5] transmissions over 40 km have been demonstrated.

The optical transmission systems discussed above belong to the physical layer of modern optical networks, which support the telephone and Internet data we use every day. A TCP/IP (Transmission Control Protocol/Internet Protocol) equivalent network protocol architecture consists of five layers. Each layer uses the services provided by the one below and provides services to the one above through its interfaces. The five layers are the application layer (e.g., web, email and telephone), the transport layer (TCP), the network layer (IP), the data link layer (Ethernet) and the physical layer (fibre transmission systems).

In today's optical networks, electronic devices such as switches and routers are interconnected by optical fibre links. A major limitation of these types of networks, often referred to as electro-optic networks, is the "electronic bottleneck". This electronic bottleneck is caused by the fact that the information transfer involves time-consuming processes of optical-to-electronic conversion, electronic signal processing, and electronic-to-optical conversion of data signals at intermediate network nodes. Additionally, all of the information carried on optical fibres must be processed at electronic data rates that are compatible with electronic circuitry (in the order of 40 Gb/s at present), thereby limiting the network throughput.

A new concept, called all-optical networking, has been developed to overcome these effects. Using this concept, information can be transmitted using optical signals and without optical-to-electronic conversion or vice versa. Networks constructed using this concept are called All-Optical Networks (AONs) [6]. In AONs, as the name indicates, information is transmitted entirely in optical form. There are no optical/electronic conversions within the network. One major advantage of AONs with respect to their electro-optic counterparts is their much higher bandwidth. Elimination of electronic/optical conversion reduces

delays, increases capacity, and improves flexibility of networks. In this regard, AONs are a natural solution to the ever-increasing demand for higher speeds and larger capacities. However, although AONs are advanced in nature, they do face various challenges that need to be addressed before AONs can be commercialized.

As one may expect a number of network functionalities, traditionally realized in the electrical domain, have to be implemented in an optical way, including wavelength conversion, demultiplexing, regeneration and optical packet switching.

Wavelength conversion addresses a good many key issues in WDM networks including interoperability, scalability, transparency, and network capacity. Strictly transparent networks offer seamless interconnections with full reconfigurability and interoperability. Wavelength conversion can be used to interface different networks. It can also ensure future seamless network evolution. In a wavelength-routed network wavelength conversion can be utilized to route and switch lightpaths while also ensuring added functionalities such as contention resolution and blockage removal, especially under dynamic traffic patterns. In the last several years various technologies of all-optical wavelength conversion have been proposed and investigated. Using four-wave-mixing (FWM) [7], cross phase modulation (XPM) in a non-linear optical loop mirror (NOLM) [8-12] or XPM-induced polarization rotation [13], fibre-based schemes have shown great potential for high-speed operation (up to 160 Gb/s [13]). Semiconductor optical amplifier (SOA) based solutions have been studied theoretically as well as experimentally [14,15] and it has been demonstrated that wavelength conversion can be realized in simple waveguide structures through cross gain modulation (XGM) [16,17] and FWM [18-20]. XPM in SOAs can be used in interferometer configurations to overcome the speed limitation imposed by the slow carrier recovery time, such as Michelson interferometer [21], Mach-Zehnder interferometer (MZI) [22-24] and ultra-fast non-linear interferometer (UNI) [25]. Wavelength conversion at speeds up to 160 Gb/s has been reported using MZI [24].

All-optical demultiplexing is one of the basic functions of high-speed OTDM systems. An optical demultiplexer selects one tributary channel out of the OTDM data steam for detection by a photodiode. This function can be achieved with an optical gate that can be switched on or off by an optical control signal. Fibre-based demultiplexers, either configured as a NOLM [2,26,27] or using XPM and optical filtering [28,29], have shown

ultra-high speed operation up to 1.28 Tb/s [2]. Various SOA-based solutions have been demonstrated, either based on four-wave-mixing [30,31] or using various interferometers such as symmetric MZI [32-34] or gain transparent UNI [35].

Optical packet switching and optical labelling will be indispensable for future IP-oriented all-optical networks. Traditional telephone networks only require optical cross-connects at network nodes. A cross-connect is really a circuit switch device, which switches connections or lightpaths. In contrast, the Internet based on the TCP/IP protocol is a packet-switched network. The data to be sent, called payload, is modulated on an optical carrier and then assigned an address code called label. At network nodes in AONs, optical routers accommodate the IP protocol by performing several label processing functions in optical domain, such as label encoding, erasure, reinsertion and recognition. Two approaches that have been extensively studied are the serial label [36-37] and the optical sub-carrier multiplexed label [38-41]. With serial coding a fixed bit rate label is multiplexed at the head of the IP packet with the two separated by an optical guard-band. For optical sub-carrier multiplexed labels a base band signal is modulated onto an RF sub-carrier and then multiplexed with the IP packet on the same wavelength. Recently a new optical labelling approach, known as orthogonal modulation format [42], has been proposed as a competitor to the above two schemes, where the payload and label are modulated on the amplitude and phase/frequency respectively and can be detected independently of each other [43].

In realizing wavelength conversion and demultiplexing, fibre-based solutions, although having great potential for high speed, are less attractive in terms of compactness and stability than semiconductor solutions. As to SOA-based interferometers, a complex push-pull switching mechanism has to be employed to counteract the effect associated with slow relaxation of the refractive index change induced by XGM or XPM. Alternatively, electroabsorption modulators (EAMs) have attracted intense attention due to its various advantages, such as low chirp, simple structure, compactness and suitability for integration. In the last several years, various functions have been realized using EAMs as summarised in Table 1.1 and 1.2.

Device		Bit rate (Gb/s)	Wavelength (nm)	Extinction ratio (dB)	Bias Vb/Vpp (V)
EAM-DFB	EAM-DFB[44-47]	10 [44] 40 [45-47]	1560-1610 [44] 1546 [45] 1310 [47]	15 [44] 12 [45] 9.77 [47]	Vpp 3 [45] Vb -0.9 [47]
	TW-MQW-EA-DFB[48]	40	-	-	-
DFB-SOA-EAM	DFB-SOA-EAM[49]	2.5	1545-1560	13	Vpp 2.4
	8-channel DFB-SOA-EAM[50]	2.5	1552.5-1567.8	17	Vb -2
SOA-EAM	SOA-EAM[51]	40	1545-1560	10	Vpp 2
	SSC-EAM-SOA-EAM-SSC[52]	40	-	13	Vpp 2.5
EAM-DBR	EAM-DBR[53] EAM-DBR-SOA[54-55]	2.5 [55]	1530-1570[55]	10	Vpp 3
Polarization-insensitive EAM	Tensile-strained MQW EAM [56,57*]	10 [57]	~ 1550 [57]	30 [57]	Vb -3
	Bulk EAM [58**]	40	1530-1550	10	Vpp 2.5

DFB:Distributed feedback, DBR: Distributed Bragg reflector, TW: Travelling-wave, SSC: Spot-size-converter, MQW: Multiple quantum well, Vb: bias, Vpp: Peak-to-peak voltage, * PDL<0.5 dB, **PDL<0.6 dB

Table 1.1. Optical modulators using EAMs.

Traditionally EAMs are used for optical intensity modulators, which are often integrated with lasers to reduce the coupling loss. As shown in Table 1.1, EA-DFB modules have shown a wide wavelength tuning range from 1560 to 1610 nm at 10 Gb/s [44] and modulation at 40 Gb/s has been demonstrated [e.g., 45-47]. EA can also be integrated with DBR lasers; modulation at 2.5 Gb/s has been reported with a 40 nm tuning range [55]. EA-SOA modules can realize lossless external modulators as demonstrated in [52]. Based on single EAMs polarization insensitive modulators have been manufactured using bulk EAMs [58] or tensile-strained MQW EAMs [56-57].

In addition to its traditional role EAMs have manifested its versatility in optical signal processing as shown in Table 1.2. Typical results are as follows. Using cross absorption modulation (XAM) (or XPM) in an EAM, single channel wavelength conversion at 40 Gb/s [81] (or 80 Gb/s [64]) has been realized. Demultiplexing has been achieved through several EAM-based schemes, such as 160 to 10 Gb/s by use of a twin-EAM or a travelling-wave (TW)-EAM [69,70], and 320 to 10 Gb/s through a photodiode (PD)-EAM [73]. Based on XAM in a single EAM all-optical demultiplexing has been demonstrated from 160 to 40 Gb/s [76] or from 40 to 10 Gb/s [75]. Other applications include 3R regeneration at 40 Gb/s

using an optical regenerator consisting of two EAMs [81], generation of optical pulses at 40 GHz with a pulse width of 4 ps by a TW-EAM [85], and 10 GHz clock recovery from a 160 Gb/s data stream using a MQW EAM [86].

Wavelength Conversion

Device	Mechanism	Bit rate (Gb/s)	Probe Wavelength (nm)
MQW-EAM	XAM [59-61,81] XAM/WDM-OTDM Conversion [61]	10 [60]	1540-1560
		20 [59,61]	1530-1560 [59]
		40 [81]	1556.5 [81]
Bulk [62,63], MQW [64]	XPM+DI	40 [62], 80 [64]	1545 [62], 1555 [64]

OTDM Demultiplexing

Device	Mechanism	Bit rate (Gb/s)	Sensitivity (dBm)
EAM/an optical PLL [65]	Optical gate controlled electrically	20 to 10	-
TW-MQW-EAM [66]		20 to 10	-28.5
EAM [67,68]		160 to 40	-21.7 to -23.5 [68]
Twin-EAM [69,70]		160 to 10	-21 (after 300km) [69]
TW-MQW-EAM [71]		160 to 10	-30.5
PD-TW-MQW-EAM [72,73]	O/E conversion, optical gate controlled electrically	160 to 10 [72] 320 to 10 [73]	-23.3 [72] -18 [73]
MQW-EAM [74,75]	XAM	40 to 10	-33.5 [75]
SC-EAM [76]		160 to 40	-
EAM [77,78]	FWM	80 to 10	BER 1.8×10^{-8} [78]

Regeneration

Device	Mechanism	Bit rate (Gb/s)	Type
EAM [79-81,83]	Regenerative wavelength conversion	10 [79, 83] 20 [80] 40 [81]	3R
EAM [82]		10	2R

Short Pulse Generation

Device	Mechanism	Repitition rate (Gb/s)	Pulse width (ps)
EAM [68,84]	Non-linear absorption	20 [84], 40 [68]	1.8* [84], 5 - 5.5 [68]
Twin-EAM [67,70]		40	< 3 [67], 3.2 [70]
TW-EAM [85]		40	4

Clock Recovery

Device	Mechanism	Line rate (Gb/s)	Clock rate (GHz)
Single EAM[65,78,83,86] Twin-EAM[69]	Phase comparator	10 [83]	10 [83]
		20 [65]	10 [65]
		160 [69,78,86]	10 [69, 86], 40 [78]

MQW: Multiple quantum well, XAM:Cross absorption modulation, DI: Delayer interferometer, PLL: Phase locked loop, TW: Travelling-wave, PD: Photodiode, SC: Self-cascading.
* With fibre-based regeneration

Table 1.2. Optical signal processing using EAMs.

As discussed above EAMs can realize various functions needed for future all-optical networks and the schemes of using EAMs are multifold. Understanding of the fundamentals, characterizations and system investigations of EAMs are therefore very meaningful.

The purpose of this thesis is to investigate the properties of high-capacity systems employing various kinds of optical signal processing. This includes investigations of wavelength conversion, demultplexing, regeneration and optical labelling based on orthogonal modulation format, at a bit rate of 40 Gb/s or beyond. The devices to be investigated and employed in the systems experiments will primarily be semiconductor devices, i.e., EAMs.

The thesis is organised as follows. In chapter 2 we give an introduction to EAMs and then discuss the principle of electrically controlled absorption modulation. Experimental characterizations of electrical-to-optical modulation are presented including the static power transfer curves, frequency chirp and dynamical modulation response. Chapter 3 is dedicated to optical-to-optical modulation in an EAM, where a cross absorption modulation model is given together with the simulated static characteristics and experimental characterizations of the frequency chirp and small signal bandwidth. Wavelength conversion using an EAM is discussed in Chapter 4. We present our experimental studies on single and multi-channel wavelength conversions up to 40 Gb/s. An analysis of the optimum operation of an EAM-based wavelength converter and a comparison with other schemes are given subsequently. In Chapter 5 we present our experimental investigations of all-optical demultiplexing employing a single EAM with a simple waveguide structure at up to 160 Gb/s. An analysis of the optimum operation of an EAM-based demultiplexer and a discussion of 2R regeneration using an EAM or a dispersion imbalanced loop mirror (DILM) are given afterwards. Starting with an introduction to optical-label-switched network and orthogonal modulation, Chapter 6 presents our experimental investigations of several optical labelling schemes, including Amplitude Shift Keying (ASK)/Differential Phase Shift Keying (DPSK) labelling, ASK/Frequency Shift Keying (FSK) labelling and DPSK/ASK labelling. EAMs are used here for label encoding, erasure and swapping. In the last section of Chapter 6 we give an analysis of the modulation cross talk present in previous labelling schemes, and then we propose a new coding scheme for the ASK payload to mitigate this cross talk. Based on this coding scheme optical label swapping based on a 40 Gb/s return-to-zero

ASK payload and a 622 Mb/s DPSK label is experimentally demonstrated. A new labelling format using Polarization Shift Keying (PolSK) is proposed in Chapter 7, where we present our experiments with optical label swapping and transmission in DPSK(40Gb/s)/PolSK(2.5Gb/s) format. Finally, Chapter 8 summarises and concludes the thesis.

2

Electroabsorption Modulator

In optical communication systems information is encoded into a digital optical signal by turning the light on and off. This is the process of the optical intensity modulation that is widely used in various optical links of today and is referred to as the intensity modulation (IM) or amplitude shift keying (ASK) in the literature. The intensity modulation is implemented in an optical modulator that modifies one or more characteristics of an optical signal for the purpose of conveying information. There are basically three kinds of IM modulators that have been put into commercial use, i.e., the directly modulated diode (DM), the lithium niobate based Mach-Zehnder interferometer ($LiNbO_3$ OR LN-MZI) and the electroabsorption modulator (EAM).

The directly modulated laser diodes have several advantages such as easy modulation being obtained by changing the injection current, and no insertion loss associated with external modulators. Such systems are simple and compact in configuration, which leads to stability. However, the large frequency chirp associated with the direct modulation of laser diodes operating at a few GHz has become a serious problem in high-speed long-distance optical-fibre systems [87]. It is found that 1550 nm lightwave systems are limited to distances below 100 km even at a bit rate of 2.5 Gb/s because of the frequency chirp [88]. Still, higher bit rates (up to 10 Gb/s) and longer distances at 2.5 Gb/s can be achieved by use of some compensating techniques, such as negative dispersive fibres [89,90], fibre gratings [91,92] and light injection [93]. These schemes, however, increases the system complexity and cost. To overcome the drawback of DMs external modulators are developed, a successful example of which is the LN-modulator. The LN-modulator has a structure of MZI and the lithium niobate is chosen because of its high electrooptic coefficients. The chirp-free or chirp-tuneable modulation can be realised by a LN-modulator at a bit rate up to 40 Gb/s [94,95]. As a competitor to the LN-modulator, an EAM realizes the direct amplitude modulation by changing

the absorption of the light propagating in the EAM waveguide. EAMs have various superb characteristics such as low wavelength chirp, broad wavelength range, low drive voltage and compactness. In addition, EAMs also can be monolithically integrated with a Distributed Feedback Laser (DFB) or Distributed Bragg Reflector Laser (DBR), which makes it possible to achieve high optical output, compactness and high reliability in systems.

In this chapter we will first give an introduction to EAMs and then discuss the principle of electrically-controlled absorption modulation. Finally, experimental characterization of electrical-to-optical (e/o) modulation characteristics will be presented including static power transfer curves, frequency chirp and dynamical modulation responses.

2.1 Introduction to EAMs

An EAM is basically a reverse-biased p-i-n diode. The choice of the material an EAM is made of depends on the operating wavelengths. Particularly, systems working near 850 nm may use the InGaAs (well) /GaAs (barrier) or GaAs/AlGaAs material system and systems near 1310 nm or 1550 nm may be realized using InGaAsP/InP, InGaAsP/InGaAsP, or InGaAlAs/InP [96]. A schematic structure of the EAM developed under the SCOOP project and employed for most of our experiments reported in this thesis is shown in Fig. 2.2.

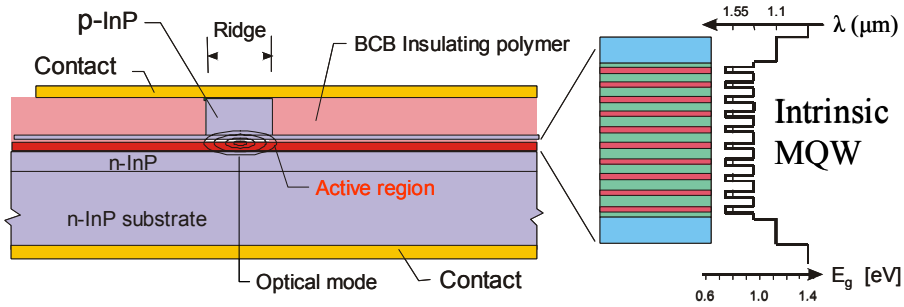

Fig. 2.1. Structure of the EAM.

Two metal bonding pads attached on the top and bottom are used for conducting the electrical signals. Based on the InP substrate the n-type,

intrinsic and p-type layers are grown. The intrinsic layer contains multiple quantum wells made of InGaAsP. The electric field is restricted within the area under the ridge due to the usage of the insulating polymer (BCB). The ridge structure also limits the horizontal distribution of the guided mode due to the refractive index discontinuity at the interface between p-InP and BCB. To the right is shown the intrinsic region, showing that the intrinsic layer contains multiple quantum wells. The depicted conduction band edge of the active region suggests the separation confinement for carriers and photons in the vertical direction, namely that carriers are confined in wells and photons are confined by the heterostructure. As a result of the transverse confinement, the high interaction efficiency between electric and optical fields is achieved.

The practical use of a single EAM chip requires a specially designed set-up, as shown in Fig. 2.2.

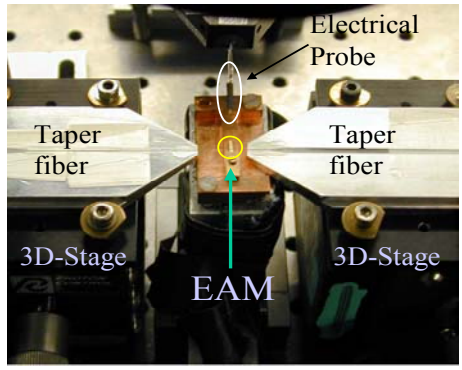

Fig. 2.2. Set-up for the EAM.

The EAM is fixed on a temperature-controlled platform. A microwave probe or metal needles are utilised to guide the electric signals onto the bonding pads of the device. Light is coupled into and out of the EAM with two taper fibres on both sides. Two 3-dimensional stages, upon which the taper fibres are fixed, can be used to optimize the coupling between fibres and the device.

2.2 Principle of electroabsorption modulation

When a light beam is incident on the EAM it is absorbed by the medium provided that the photon energy is larger than the bandgap. If the absorption edge can be adjusted by an external electrical signal, then the light absorption and consequently the intensity of the optical output will follow the change of the modulating electrical signal. This is the classical operation principle of an EAM.

The fundamental mechanism of electroabsorption is the electric field dependence of optical absorption near the optical band edge [97,98]. In bulk semiconductors, the resultant shift and broadening of the band edge absorption is usually known as the Franz-Keldysh effect (FKE) [99,100], in honour of Franz and Keldysh who first reported the ground breaking theoretical studies in 1958. A number of theories were developed as explanations of the FKE [101-103] and FKE is commonly explained as electric field-assisted tunnelling of electrons through the Coulomb barrier away from the hole, which leads to the filed-dependent exponential absorption tail that extends to energies below the bandgap. As an example, Fig. 2.3 shows the calculated absorption spectrum for bulk GaAs [103]. The detuning energy is the energy difference between the incident photons and the bandgap. With no field there is ideally no absorption below the bandgap as indicated by the black line. When an electric field (1×10^5 V/cm) is applied, an absorption tail (pink line) is generated. This tail gives rise to absorption of incident photons whose energy is lower than the bandgap.

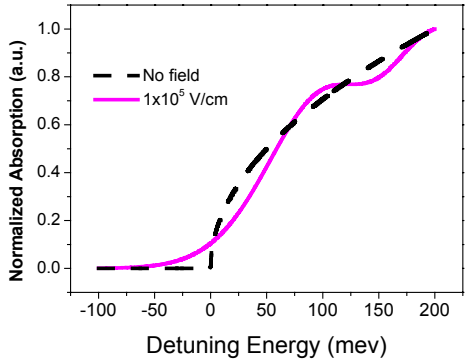

Fig. 2.3. Absorption spectra for bulk GaAs under zero filed (black) and a field of 10^5 V/cm (pink).

In relatively pure semiconductors, especially at low temperature, the absorption edge in direct-gap semiconductors can be dominated by the exciton absorption resonances corresponding to the creation of an electron and hole in a hydrogenic orbit. When the effect of the Coulomb correlation of electron and hole is properly included, a Stark shift of the exciton resonance to lower energies is expected under external electric field [104]. However, for fields of the order of a few times the classical ionization field, the resonance is severely broadened because field ionization drastically reduces the exciton life-time and the resonance shift is limited to ~10% of the binding energy (the energy required to separate the electron and hole that constitute an exciton) [104]. This effect limits the modulation efficiency of the Franz-Keldysh modulator.

In MQW semiconductor structures large shifts in band edge absorption was observed for electric fields perpendicular to the layers [105]. The shifts can extend the exciton binding energy and yet the exciton resonances remain well resolved. Extended room-temperature measurements confirm the existence of exciton resonances up to 10^5 V/cm. This mechanism is known as quantum-confined stark effect (QCSE) [103,106,107]. In contrast with the Franz-Keldysh effect that is independent of crystal size, the QCSE requires the quantum confinement in the thin semiconductor layers. When applied perpendicular to the quantum well layers, electric fields pull the electrons and holes towards opposite sides of the layers resulting in an overall net reduction in energy of an electron-hole pair and a corresponding Stark shift in the exciton absorption. The walls of the quantum well impede the electron and hole from tunnelling out of the well. Because the well is narrow (~10 nm) compared to the three-dimensional exciton size the electron-hole interaction, although slightly weakened by the separation of electron and hole, is still strong, and well defined excitonic states can still exist [106]. Thus exciton resonances can persist to much higher fields than in the absence of this confinement, and large absorption shifts can be seen without excessive broadening [98].

A simplified model [103] describing the absorption spectrum in the presence of applied filed was proposed by neglecting the exciton effects in quantum well. This model, known as Quantum-Confined Franz-Keldysh effect (QCFK), provides very useful insight and establishes a connection between FKE and QCSE, even though it doesn't completely describe the absorption property. The calculated absorption spectrum for GaAs/AlGaAs with well width of 15 nm is shown in Fig. 2.4 (a) [103].

With no field the quantized absorption edge is 30 mev larger than the bandgap. This absorption edge moves towards longer wavelengths with the increased field, giving rise to optical absorption for photon energies below the zero field bandgap. Compared to the FKE, larger on-off ratios are expected due to the quantized absorption spectra and the associated shifts. With an increase in the well width the quantization effect fades and the absorption spectrum of the quantum well evolves towards that of bulk, as shown in Fig. 2.4 (b).

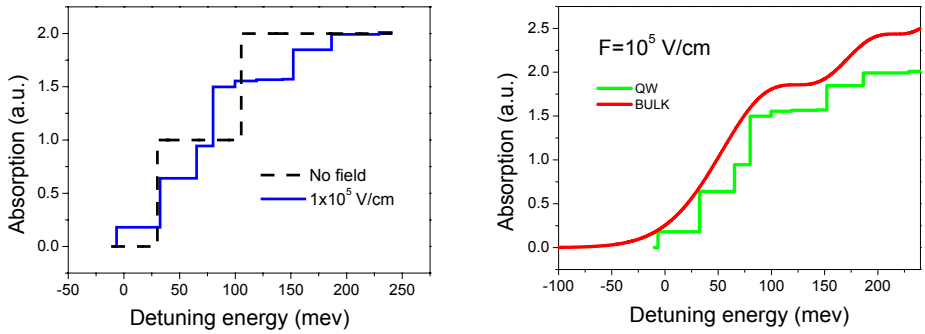

Fig. 2.4. (a) Absorption spectrum of GaAs/AlGaAs under various applied fields, (b) comparison of absorption spectra for bulk and QW structure (20nm well).

2.3 Experimental characterization

In this section experimental characterization of electrical-to-optical modulation characteristics of the EAM will be presented, including static power transfer characteristics, frequency chirp, small signal bandwidth, dynamical eye diagrams and transmission properties.

2.3.1 Static power transfer characteristics

The static modulation performance of an EAM is investigated with emphasis on impacts of the reverse bias and the operating wavelength on the static extinction ration and the insertion loss. The insertion loss is defined as the fibre-to-fibre loss under zero bias, including the loss

stemming from fibre-device coupling, reflection at the device facets and propagation in the device. The static ER is defined as the ratio (dB scale) of the output power under zero bias to that under a finite bias. The two parameters are easy to measure and provide a preliminary evaluation of the e/o modulation in an EAM. The insertion loss determines the optical power level at the output of the EAM. The static extinction ration approximately determines the on-off ratio of the modulated signal.

Fig. 2.5 (a) shows the measured static power transfer characteristics at various wavelengths, namely the output power versus the reverse bias with an input power level of 7 dBm. Fig. 2.5 (b) shows the insertion loss and the static extinction ratio at a reverse bias of –4 V for wavelengths ranging from 1530 to 1600 nm.

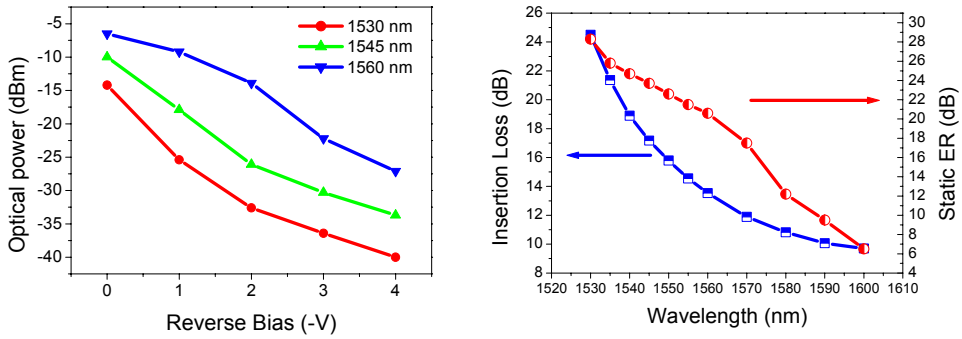

Fig. 2.5. (a) Output power versus reverse bias at various wavelengths, (b) insertion loss and static ER at –4 V versus wavelength.

It is noted that larger reverse biases lead to lower output powers for all wavelengths due to the increased absorption. Variation of the effective reverse bias by the applied electrical signal leads to the change of the output power, i.e., intensity modulation, as illustrated in Fig. 2.5(a). It is also clearly seen that shorter wavelengths have larger insertion loss. This is explained by the fact that even with no field applied on the EAM there is still residual absorption, which is inversely proportional to the operating wavelength. The blue line in Fig. 2.5(b) gives a more explicit picture, showing a monotonic decrease of the insertion loss with the increase in wavelength. For wavelengths ranging from 1530 nm to 1560 nm the measured static extinction ratios are larger than 20 dB, with the maximum of 28.3 dB at 1530 nm and the lowest of 20.6 dB at 1560 nm.

As will be shown later in this thesis this feature enables a large tuning wavelength range as well as the multiple channel all-optical wavelength conversion.

2.3.2 Frequency chirp and small signal bandwidth

The chromatic dispersion of optical fibres and the chirp α-parameter of optical modulators are believed to have significant impacts on transmission systems because the interplay between the chirp of the modulated pulses and fibre dispersion may broaden pulses, leading to peak power reduction, pulse deformation and inter-symbol interference (ISI). It is therefore of significant interest to investigate the chirp property of an EAM. The chirp α-parameter of an EAM is defined as [108]:

$$\alpha = \Delta n / \Delta k \tag{2.1}$$

where Δn and Δk are the relative changes of the real and imaginary parts of the refractive index, respectively. Based on Eq. (2.1) a new definition is proposed, which is directly related to the emitted light characteristics [108]:

$$\alpha(t) = 2\frac{d\phi / dt}{1/P \times (dP/dt)} \tag{2.2}$$

where ϕ and P are the instantaneous phase and optical power of the generated optical pulse, respectively.

Several chirp measurement methods have been proposed. Differential absorption spectra allow finding of the chirp α-parameter via Kramers-Krőnig relations [109,110]. However, since light chirping is one of the intrinsic properties of the modulated pulses direct measurements of the emitted light characteristics are preferred. The sideband-to-carrier ratio measurement of chirped light spectra is a direct method that can be used for most types of external modulators or directly modulated lasers [111,112]. This method, however, does not give the sign of the chirp α-parameter. Another direct method is to observe the broadening of a pulse propagating in a fibre [113], chirp is then given by time-domain measurements. A major drawback of the method is that it requires measurements with many different lengths of optical fibre [114].

A fibre response method proposed by Devaux [114] enables the simple and fast measurement of low chirp α-parameter in the –10 to 10 range. Measurements are performed in the frequency domain with small modulation depth. We use this method for our chirp investigation.

The experimental set-up for chirp measurement is shown in Fig. 2.6, which can also be used to measure the small signal bandwidth by removing the fibre. A cw laser beam at 1547 nm (DFB) is injected into the reverse biased EAM where it is modulated through the QCSE as controlled by the rf voltage from the Network Analyser (NA). The e/o response is measured by choosing S_{21} option in the NA. The S_{21} mode of a NA measures the frequency response of the transmission coefficient of the device under test (DUT) by scanning the modulation frequency; the definition can be found in [115]. By transmitting the modulated light over 70 km of standard SMF fibre, the e/o chirp can be evaluated.

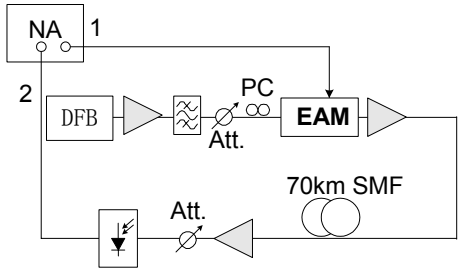

Fig. 2.6. Experimental set-up for chirp and small signal bandwidth measurements.

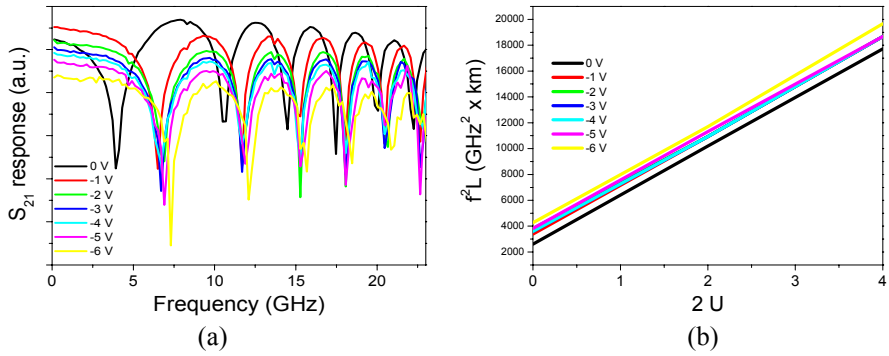

Fig. 2.7. (a) Measured S_{21} response and (b) the corresponding f^2L.

The measured S_{21} response is shown in Fig. 2.7 (a) at various reverse biases from 0 to –6 V. Sharp resonance frequencies are observed as

indicated by the dips in the Fig. 2.7(a). This phenomenon originates from interferences between carrier and sideband wavelengths. The chirp information is hidden in the positions of those dips as governed by [114]:

$$f_u^2 L = \frac{c}{2D\lambda^2}(1 + 2u - \frac{2}{\pi}\arctan(\alpha)) \tag{2.3}$$

where f_u denotes the resonance frequency at dip number u, c light velocity, D fibre dispersion, λ wavelength, and α the chirp parameter. The calculated product of response frequency squared and length ($f_u^2 L$) is shown in Fig. 2.7 (b), where the slopes of the lines determine the fibre dispersion and the crossing points with y-axis determine the chirp α-parameters at corresponding reverse biases. As indicated by Eq. (2.3), this method gives *arctan(α)* rather than α itself. The uncertainty becomes important only when *arctan(α)* comes close to the asymptotic value of ±π/2, corresponding to an approximate α-parameter range from –10 to 10. However, since EAMs usually have very small chirp, high accuracy is expected. Indeed, an uncertainty of ±0.01 of the measured chirp α-parameter has been reported in [114].

The final result of the measured chirp α-parameter is shown in Fig. 2.8 as a function of the reverse bias.

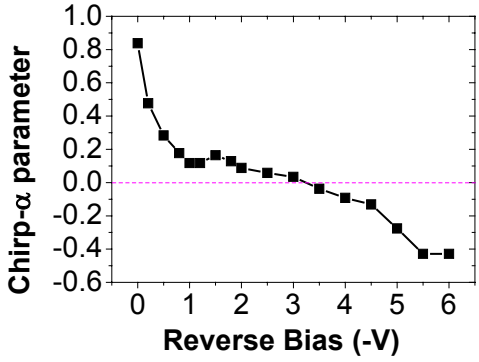

Fig. 2.8. Chirp α-parameter versus reverse bias.

It is found that the chirp α-parameter has a very strong dependence on the reverse bias, changing from 0.8 to –0.4 as the reverse bias varies from 0 to –6 V. The bias-dependence of the chirp parameter shown in Fig. 2.8 is in good agreement with the result in [116], where an EAM that is also

developed under SCOOP project was measured on using a heterodyne technique. Hence, using only one parameter (one value) can't precisely describe the chirp property of EAM. It is found in [117] that the pulse chirp at high intensities is dominant in terms of the eye-opening after transmission. A 3 dB rule is thus proposed to define an effective chirp parameter by averaging the chirp parameter from the peak to the 3 dB intensity point of the pulse. This definition is a good approximation but does not apply if the chirp parameter varies greatly in the averaging region. Therefore, to get a comprehensive knowledge of the chirp property of an EAM, the chirp-bias curve is still preferred.

Compared to direct modulation of laser with typical chirp parameter of 4-6 [96], the EAM has smaller chirp and therefore enables longer transmission distance. For transmission in anomalous dispersion region, a negative chirp α-parameter is desirable since it counteracts the fibre dispersion such that the pulse broadening is suppressed [118]. However, as seen from Fig. 2.8, the negative chirp is obtained by operating in the larger bias range, which results in lower output power and poorer ER.

By removing the fibre from the setup, the small signal bandwidth is directly measured. Depending on the size of contact pad and quantum well width, the small signal bandwidth can be as large as 24 GHz. More discussion will be given in the next chapter, where electrical-to-optical modulation is compared with optical-to-optical modulation in terms of modulation bandwidth and frequency chirp.

2.3.3 Dynamical characteristics

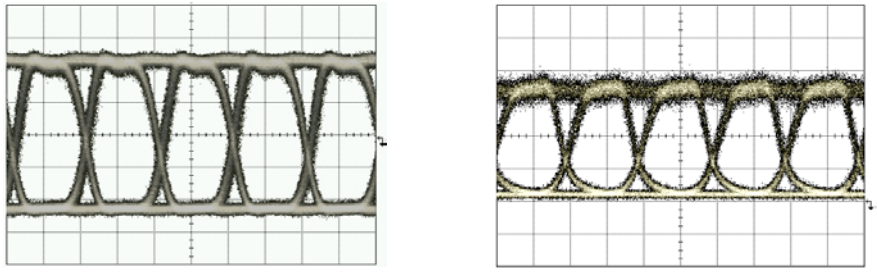

(a) (b)

Fig. 2.9. Eye diagrams at 10 Gb/s of (a) the electrical signal and (b) the modulated signal.

The eye diagrams of the electrical signal and the modulated signal at 10 Gb/s are shown in Fig. 2.9. The signal wavelength is 1550 nm and the peak-to-peak modulation voltage is 3 V. The input and average output powers are 7 and –12 dBm, respectively. Clear and open eyes are observed and the measured extinction ratio is about 15 dB at a reverse bias of –1.5 V. The modulated signal is transmitted along a 50 km SMF without dispersion compensation with a power penalty of 0.8 dB compared to the back-to-back case.

2.4 Summary

In this chapter we gave an introduction to the EAM. The ridge on the active layer and the compositions of the active layer forms the transversal confinement for both carriers and photons, which is helpful to get high modulation efficiency.

Several mechanisms that form the basis of electroabsorption were briefly discussed including Franz-Keldysh effect, Quantum-Confined Stark Effect and Quantum-Confined Franz-Keldysh effect. QCSE is found to be more effective in the absorption modulation than FKE at room temperature due to the quantum confinement of electrons and holes.

Experimental investigations on e/o modulation of the EAM were presented. From the measured power transfer curves, static extinction ratios larger than 20 dB were obtained for wavelengths in the C-band. It is also noted that the insertion loss and the static extinction ratio decrease with the signal wavelength, indicating an optimum wavelength considering the trade-off between the on-off ratio and the optical signal-to-noise ratio.

We also investigated the chirp property and the small signal bandwidth for electrical-to-optical modulation of the EAM. It is found that the measured chirp α–parameter ranges from –0.4 to 0.8 depending on the reverse bias; the higher the bias, the smaller the chirp becomes. Negative chirp may be achieved by sacrificing the extinction ratio and the output power. The small signal bandwidth was measured to be as large as 24 GHz, which will be discussed in more detail in the next chapter together with the optical-to-optical bandwidth.

Finally the dynamical response of an EAM was studied by evaluating the eye diagram of the modulated signal at 10 Gb/s. The extinction ratio

was found to be 15 dB with a modulation swing of 3 V. The modulated signal was then transmitted over a 40 km SMF and the power penalty due to the transmission was 0.8 dB.

3

Optical-to-optical modulation in an EAM

We have discussed the electrical-to-optical (e/o) modulation characteristics of an EAM in the last chapter, which forms the basis for the major practical use of the EAM, namely as an external modulator. In this chapter we study the optical-to-optical (o/o) modulation characteristics of the EAM, which can be used for all-optical signal processing such as wavelength conversion and demultiplexing for future optical networks. Starting with an introduction of the carrier effects in an EAM we will first discuss the principle of the o/o modulation by introducing a theoretical model that simulates the carrier dynamics in the EAM. Based on this model, we will present the simulated static responses of an EAM under optical excitation. Then we will discuss our experimental investigations of the modulation bandwidth and the frequency chirp for the small signal modulation, which will be compared with that of the e/o modulation. A summary will be given in the end.

3.1 Introduction to the carrier effects

As discussed before, an electric field can alter the band gap or absorption edge of a MQW EAM through QCSE and consequently change the absorption coefficient, forming the basis for e/o modulation. Alternatively, instead of using an electric field as the external excitation, we can use a high-intensity light beam to modulate the absorption of another light beam, i.e., the o/o modulation or cross absorption modulation (XAM).

There are basically two carrier effects involved in the o/o modulation, i.e., the band-filling effect [119,120] and the field-screening effect [121-124] as schematically illustrated in Fig. 3.1. The band-filling effect originates from the stimulated absorption of an incident light wave that

elevates electrons from the valence band to the conduction band and results in an increase in the electron density for the conduction band and a decrease for the valence band; these changes of the carrier distributions lead to a reduction of the absorption, due to the "bleaches" of valence to conduction band transitions.

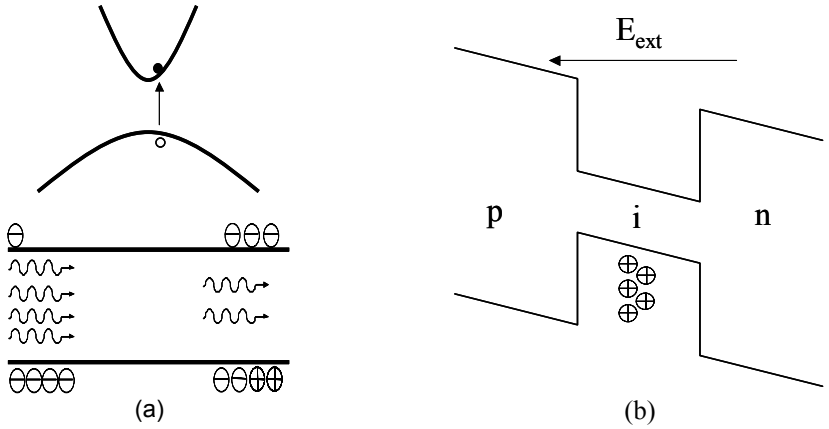

Fig. 3.1. Schematic of (a) band-filling and (b) field-screening effects.

The field-screening effect is shown in Fig. 3.1 (b). The photon-generated electrons and holes in the intrinsic layer are initially trapped in the quantum wells. Due to the relatively small effective mass electrons quickly escape out of the wells and are afterwards swept out of the active layer by the external field. In contrast, holes with larger effective mass have much smaller escaping rates than electrons and thus build up in the *i* region [121]. The build-up of positive charges screen the external field and change the field gradient according to the Gauss's law [122]. This effect leads to a reduction of the electrical field seen by some quantum wells and consequently less absorption.

3.2 Description of the model

The dynamics of the carrier distributions in the active region of the EAM is treated on the basis of semi-classical density matrix Eqs. [125-127] for the upper (conduction band) and lower (valence band) occupation probabilities $\rho_{c,k}$ and $\rho_{v,k}$ for electrons and holes, respectively.

The index k is the electron wavenumber and corresponds to the numbering of an inhomogeneously broadened set of two-level systems. The carrier distributions approach equilibrium due to carrier-carrier and carrier-phonon scattering, which are included through phenomenological relaxation terms. This approximation avoids the solution of a complicated many-body problem [128-130], and is justified for not too large deviations from Fermi distributions [131]. Introducing the slowly varying envelope function $A(z,t)$ (z is the spatial coordinate along EAM and t is time) for the electrical field $E(z,t)$

$$E(z,t) = A(z,t)e^{-iw_0 t} + A^*(z,t)e^{iw_0 t} \tag{3.1}$$

as well as for the atomic polarization $\rho_{cv,k}$, between the upper and lower states with index k,

$$\rho_{cv,k} = \sigma_{cv,k}(t)e^{-iw_0 t} \tag{3.2}$$

the density matrix Eqs. take the following form [132]:

$$\begin{aligned}\dot{\rho}_{\alpha,k} = &-\frac{\rho_{\alpha,k}(t) - f_{\alpha,k}(t)}{\tau_{1\alpha}} - \frac{\rho_{\alpha,k}(t) - f^{L}_{\alpha,k}(t)}{\tau_{h\alpha}} - \frac{\rho_{\alpha,k}(t) - f^{eq}_{\alpha,k}(t)}{\tau_{s}} \\ &-\frac{i}{\hbar}[d_k^*\sigma_{cv,k}(t)A^*(z,t) - d_k\sigma^*_{cv,k}(t)A(z,t)] + \Lambda_{\alpha,k}, \quad \alpha = c,v\end{aligned} \tag{3.3}$$

$$\dot{\sigma}_{cv,k} = -(i(\omega_k - \omega_0) + \frac{1}{\tau_2})\sigma_{cv,k}(t) - \frac{i}{\hbar}d_k[\rho_{c,k} + \rho_{v,k} - 1]A(z,t) \tag{3.4}$$

We have here employed the slowly varying envelope approximation, i.e., terms oscillating at $2\omega_0$ are neglected. The three first terms on the right hand side of Eq. (3.3) describe the relaxation of the carrier distribution function $\rho_{\alpha,k}$ towards equilibrium due to various scattering mechanisms. The first term represents carrier-carrier scattering with a characteristic time constant $\tau_{1\alpha}$ (~ 100 fs). This scattering mechanism leads to the equilibration of the carrier distribution towards a Fermi distribution function $f_{\alpha,k}(t)$ parameterized by a Fermi level $E_{f,\alpha}$ and a carrier temperature T_α. The second term describes equilibration of the carrier temperature towards the lattice temperature T_L due to electron-

phonon collisions with a characteristic time constant $\tau_{h\alpha}$ (~ 1 ps). The Fermi distribution function is defined by the instantaneous carrier density $N = N(t)$, and the lattice temperature T_L. The third term accounts for relaxation towards the thermal equilibrium $f_{\alpha,k}^{eq}$, which will be achieved in the absence of external pumping due to spontaneous radiative and non-rediative recombinations, with τ_s being the carrier lifetime. Finally the term $\Lambda_{\alpha,k}$ denotes pumping due to current injection, τ_2 is the relaxation time of the dipole and d_k is the dipole moment of the transition as given in, e.g., [125].

This model is basically developed for forward biased devices, which can be applied to a reversed-biased EAM with a modification of the carrier lifetime. The photo-generated carriers in an EAM are quickly swept out of the intrinsic region by the external electric field [133]. The carrier lifetime is thus dominated by a sweep-out time, τ_{so}, which replaces τ_s in Eq. (3.3). The sweep-out time of carriers represents the entire sweep-out process, including escape from wells, bulk transport away from wells and transport across the separate-confinement heterostructures. A simple carrier-density-dependent sweep-out time [134] is used for our model, which on a phenomenological level describes the increment of the sweep-out time at higher power levels. As shown in Eq. (3.5), the sweep-out time varies as a function of the carrier density, from 8 ps at low densities (τ_0) and to 25 ps at transparency (τ_{tr}), with reference to [134]. The mechanism that leads to a longer sweep-out time at higher carrier densities is the screening of the applied field by photon-generated carriers [121-124].

$$\tau_{so}(N) = \frac{\tau_0 \tau_{tr}}{\tau_{tr}(1 - \frac{N}{N_{tr}}) + \tau_0 \frac{N}{N_{tr}}} \tag{3.5}$$

The wave propagation equation for the slowly varying electrical field envelope can be derived from Maxwell's Eqs. [118]:

$$\frac{\partial A(z,t)}{\partial z} = -\frac{1}{v_g}\frac{\partial A(z,t)}{\partial t} + \frac{1}{2}(\Gamma g - \alpha_{\text{int}})A(z,t) \tag{3.6}$$

where A is the slowly varying complex electrical field amplitude, v_g the group velocity ($v_g=c/n_g$), Γ the optical field confinement factor, α_{int} the internal loss, g the gain (absorption).

Based on Eqs. (3.3-3.6) and after some manipulations we finally obtain the following set of simplified rate Eqs. [132]:

$$\frac{dN_{qw}}{dt} = \frac{I}{eV} - v_g g S(z,t) - \frac{N_{qw}}{\tau_{so}} \tag{3.7}$$

$$\frac{\partial S}{\partial z} + \frac{1}{v_g}\frac{\partial S}{\partial t} = (\Gamma g - \alpha_{\text{int}})S \tag{3.8}$$

$$g = g_l(N)(1 - \in S) \tag{3.9}$$

$$g_l(N) = a_N(n_{c,l} + n_{v,l} - N_0) \tag{3.10}$$

$$\in = a_N(\tau_{1c} + \tau_{1v}) \tag{3.11}$$

$$g = g_l(N)(1 - \in S) \tag{3.12}$$

$$a_N = \frac{\omega_0 |d_k|^2 \tau_2}{\hbar \varepsilon_0 n c} \tag{3.13}$$

In Eq. (3.7), N_{qw} is the total electron density in the conduction band of the quantum well, which is equal to the total hole density in the valence band since we assume the intrinsic region of EAM is undoped. In fact, charge imbalance could result from different sweep-out times [122], which is not treated in our model. I is the current due to the reverse bias, V the volume of the active region, e the electron charge. S is the photon density of the incident light, defined as [132]:

$$S(z,t) = \frac{2\varepsilon_0 n n_g |A(z,t)|^2}{\hbar \omega_0} = \frac{P \cdot v_g}{\hbar \omega_0 c A_m} \tag{3.14}$$

where P denotes the optical power, $\hbar$ the Planck's constant divided by 2π, ω_0 the wavelength, c the light velocity, A_m the mode cross-section supported by the EAM waveguide ($A_m=A_{ac}/\Gamma$, A_{ac} is the area of the active region [96]).

In Eq. (3.10), $n_{c,l}$ and $n_{v,l}$ are "local" carrier densities in conduction and valence band respectively, which are directly coupled into the incident optical field. Local carrier densities are calculated by:

$$n_{\alpha,l} = \frac{N_0}{1+\exp(\frac{E_{\alpha,0}-E_{f,\alpha}}{k_B T})} \quad , \quad \alpha = c, v \tag{3.15}$$

Where is k_B the Boltzman constant, T the temperature, $E_{c,0}$ ($E_{v,0}$) the photon energy measured from the conduction (valence) band edge into the band, $E_{f,\alpha}$ the quasi-Fermi levels of electrons (α=c) and holes (α =v) respectively. Assuming there is only one state in quantum wells for both conduction and valence bands, $E_{f,\alpha}$ is determined by the total carrier density N_{qw} [96].

$$E_{f,\alpha} = k_B T \ln[\exp(\frac{N_{qw}\pi\hbar^2 L_{qw}}{k_B T m_\alpha^*}) - 1] \quad , \quad \alpha = c, v \tag{3.16}$$

N_0 is the density of available states in the optically coupled region and is calculated by:

$$N_0 = \frac{m_r^*}{\pi\hbar^2 L_{qw}} \hbar\pi\gamma_2 \tag{3.17}$$

where m_r^* denotes the reduced effective mass, L_{qw} the width of the quantum well, γ_2 the inverse of the time constant τ_2 . An approximate separation of carriers is used here. Carriers are separated into two groups, namely, those that are coupled directly into the optical field and those that are not [132]. We have used a "hat" line-shape function to approximate the Lorentzian line-shape function for states broadening in the optically couple region [132].

The filed-screening effect and the QCSE are experientially included through fitting parameters by allowing the band-gap change due to the carrier density and the reverse bias [135].

3.3 Optical-to-optical modulation

Using the model described above we can now study the o/o modulation in an EAM. Due to the band-filling and the field-screening effects the gain or absorption coefficient is dependent on the carrier density, as shown in Fig. 3.2 (1550 nm). At low carrier densities the gain is negative corresponding to the net absorption. When the carrier density increases to about $0.8x10^{24}\ m^{-3}$, the device reaches a special state, where the stimulated absorption balances the radiative and non-radiative recombinations and the net gain or absorption is zero. This state is known as the transparent state, below which the incident light experiences the net absorption and the absorption coefficient (negative gain) monotonically decreases with the carrier density.

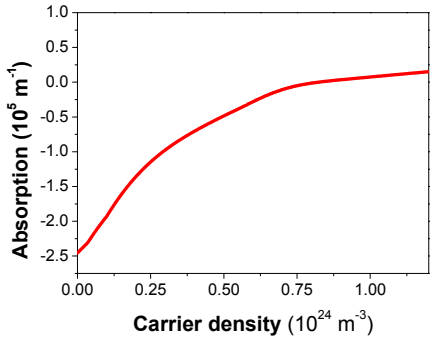

Fig. 3.2. Gain versus carrier density (1550 nm).

The dependence of the absorption coefficient on the carrier density can be viewed as an o/o modulation transfer curve, as elucidated in Fig. 3.3. Assuming the carrier density change is dominated by the absorption of pump and the device is fast enough to respond the incident pulse, then the carrier density simply follows the intensity variation of the pump, as indicated by the blue pulse labelled by *N* in Fig. 3.3. Mapping the carrier

density "pulse" (blue) to the absorption "pulse" (red, labelled by *g*) through the transfer curve, we then obtain the modulated probe signal.

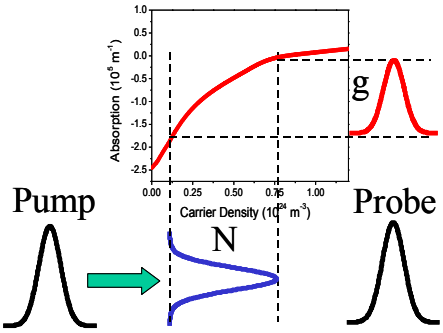

Fig. 3.3. Schematic of cross absorption modulation.

It is clear from Fig. 3.3 that the o/o modulation is an absorption modulation mediated by the carrier density. Through the o/o modulation a pump pulse opens a transmission window indicated by the red pulse, which can be used to either transfer the data information from the pump to the probe (wavelength conversion) or select from the probe one OTDM tributary channel overlapping with the *g*-window (demultiplexing).

3.4 Simulated static characteristics

In this section we present the simulated static characteristics for the o/o modulation. "Static" means that we use continuous waves (cw) at different power levels/wavelengths as the inputs of the EAM and study how the cw signals evolve along the device through the interactions with carriers.

In case of wavelength conversion, we use two power levels (10 and 20 dBm) to represent the mark signal (logic "1") and the space signal (logic "0") for the pump operating at 1540 nm. The initial extinction ratio of the pump is therefore 10 dB. The probe signal at 1550 nm has an initial power level of 10 dBm.

The evolution of the signals is depicted in Fig. 3.4, where the extinction ratios of the pump and the probe are displayed in red and black

dashed lines, respectively. It is found that during propagation in the EAM, the probe mark (solid black) travelling with the 20 dBm pump (solid red) experiences less absorption than the probe space (solid green), leading to an ever-increasing power level separation, i.e. an increase in the extinction ratio of the probe. This is due to the larger carrier density and correspondingly the less absorption in the presence of the pump mark. However, the extinction ratio of the probe saturates at a device length of 150 μm and maintains the maximum value for the remainder of the transmission. This feature can be understood by considering the power dissipation of the pump. During transmission the pump signal looses its power and becomes less effective in the carrier density modulation. When the pump power is so weak that no significant carrier density change is induced, the extinction ratio of the probe reaches its maximum. The flattening-out of extinction ratio of the probe suggests an optimum device length, since the rest part has no contribution to the extinction ratio improvement but only attenuates the signal.

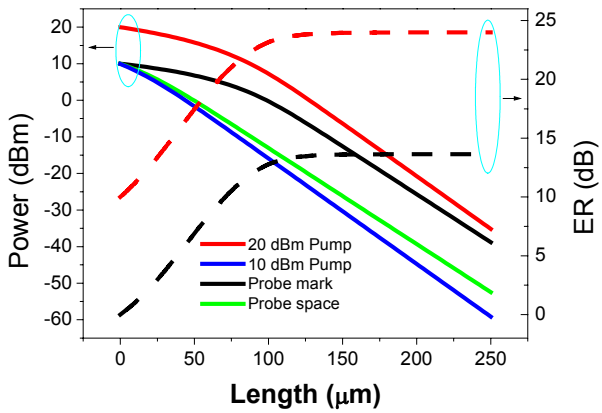

Fig. 3.4. Power and ER versus device length for wavelength conversion. Solid red, solid blue and dashed red traces denote the mark, space and ER of the pump, respectively; Solid black, solid green and dashed black traces are the mark, space and ER of the probe.

Fig. 3.4 also shows the extinction ratio improvement for the pump signal, as indicated by the red dashed line, suggesting 2R regeneration [134]. However, the presence of a cw probe in this calculation defies this justification. By switching off the cw probe, we can obtain the pure 2R regeneration of a data signal. The basic idea of EAM-based 2R regeneration is to use the non-linear absorption in EAM for ER

improvement and space noise suppression, originating from the dependence of absorption coefficient on the input power. This mechanism is elucidated in Fig. 3.5, where the dependences of the output power (blue) and the absorption (red) on the input power are shown.

As indicated by the red trance in Fig. 3.5, the signal of high power experiences less absorption than that of low power. Consequently, a non-linear power transfer curve is obtained, as suggested by the blue trace. Higher power generally leads to larger carrier density and then, according to the absorption-carrier density relation shown in Fig. 3.2, a smaller absorption coefficient results. The non-linear power transfer curve suggests a suppression of the space noise and an extinction ratio improvement. It is also found from Fig. 3.5 that the significant non-linearity occurs in a region of relatively higher powers (> 10 dBm).

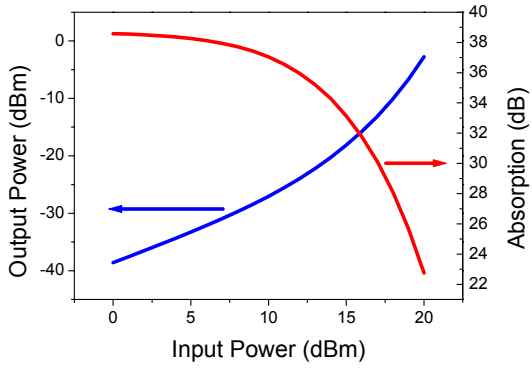

Fig. 3.5. The output power (blue) and the absorption (red) versus the input power.

In Fig. 3.6, we show the evolution of the power and the extinction ratio along the device. We consider two signals with the same initial extinction ratio of 10 dB but with different average powers. Signal A has an initial peak power of 20 dBm and a pedestal of 10 dBm. Signal B has an initial peak power of 15 dBm and a pedestal of 5 dBm.

For both signals the extinction ratio improvement is clearly seen, however the improvement saturates gradually due to the power loss. It is also noted that Signal A works in the highly non-linear region and has a longer effective interaction length and thus acquires a larger extinction ratio improvement than the one of lower power. These results indicate the benefits of using higher power provided that the device can survive. Finally, an optimum device length is suggested for a fixed average input

power since the extinction ratio stops increasing after reaching its maximum.

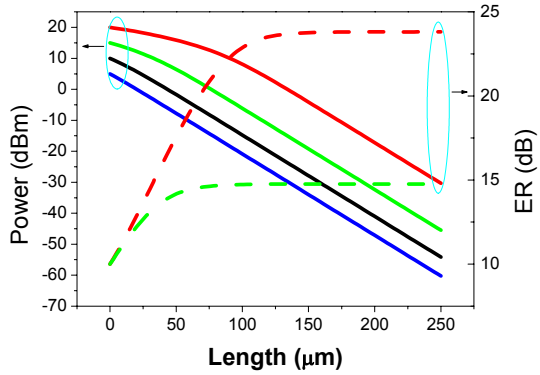

Fig. 3.6. Power and ER versus device length for regeneraion. Solid red, solid black and dashed red trances denote the mark, space, ER of Signal A; Solid green, solid blue and dashed green trances denote the mark, space, ER of Signal B.

3.5 Bandwidth and frequency chirp

In this section we present our experimental results on the o/o modulation bandwidth and the frequency chirp.

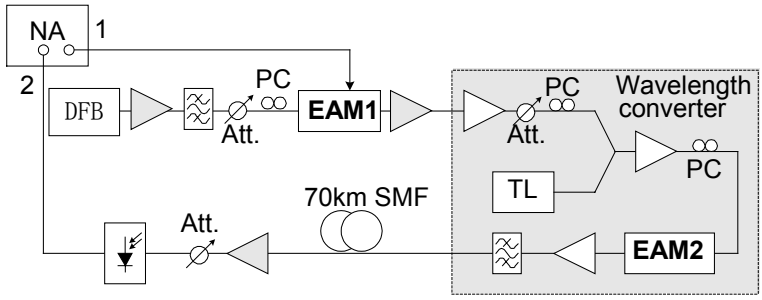

Fig. 3.7. Set-up for bandwidth and chirp measurement. NA: Network Analyser, DFB: Distributed feedback laser, Att.: Tuneable attenuator, PC: Polarization controller, TL: Tuneable laser, SMF: Single mode fibre.

The experimental set-up is shown in Fig. 3.7, and is based on an approach to small signal modulation of the EAM. In a conventional small

signal measurement, the EAM is electrically modulated around a dc bias by an rf signal with a small amplitude. In this experiment, the absorption of the EAM is modulated optically. This is achieved by letting a network analyser (NA) electrically modulate (e/o) the first EAM (EAM1 in Fig. 3.8), and then use this modulated light to modulate the absorption of EAM2. This technique allows for the assessment of the o/o bandwidth, which essentially determines the obtainable bit rate that may be wavelength converted and the switching window used for demultiplexing. Furthermore, when transmitting the modulated light over a length of fibre, the modulated sidebands of the optical spectrum will have different propagation speeds due to the dispersion of the fibre, which will lead to resonance dips in the frequency spectrum of the transmitted light. Thus, modifying the fibre-response method as discussed in chapter 2 for measuring the e/o chirp α-parameter, now allows for an evaluation of the chirp after wavelength conversion.

A cw laser beam at 1547 nm (DFB in Fig. 3.7) is injected into the reverse biased EAM1 where it is modulated through the QCSE as controlled by the rf voltage from the NA. The e/o frequency response curve is measured for reference. After this, the e/o light is amplified and combined with a tuneable cw source (TL) for wavelength conversion in EAM2. The e/o modulated light acts as the pump that saturates the absorption of the TL probe, and thus the modulation is transferred to the new TL wavelength. An optical filter blocks the original wavelength. The o/o response is determined from the measured frequency response curve by subtracting the measured e/o response. By transmitting the o/o light over 70 km of standard SMF fibre, the o/o chirp can be evaluated.

The o/o bandwidth is measured on three component types with different quantum well depths and different bonding pad sizes. It is stated in [136] that the wells in the valence band for InGaAsP compounds should be more than about 25 meV to avoid thermionic effect, and should be less than about 100 meV to achieve the high red-shift efficiency of QCSE. Hence, the components investigated here all have valence band well depths in the range of 25-100 meV, and conduction band well depths about twice that (larger barrier height of the conduction band preferred to efficiently confine electrons in wells). Depending on where in this valence band interval the components are, they are referred to as ‘shallow’, ‘medium’, or ‘deep’ well components [137]. The pad sizes very from ‘large’ (~15000 μm^2) over ‘small’ (~6000 μm^2) to ‘very small’ (~4000 μm^2). The type of the components under investigation is defined

as follows. Type 1: Deep wells, small pad, type 2: Shallow wells, large pad and type 3: Shallow wells, small pad. Fig. 3.8 shows the o/o frequency response curves for all three types with the bias and pump/probe power settings for optimised performance as an inset. The legend of Fig. 3.9 gives the type of the component, the reverse bias, and the pump/probe power. Since the modulation and the response is optical, the scale is shown in optical dB [dBo] (to convert to electrical dB [dBe], the scale should simply be multiplied by a factor of 2). The curves show that shallow wells are important for obtaining a high o/o bandwidth. Table 3.1 summarises the 3 dBe bandwidths and compares them to e/o bandwidths.

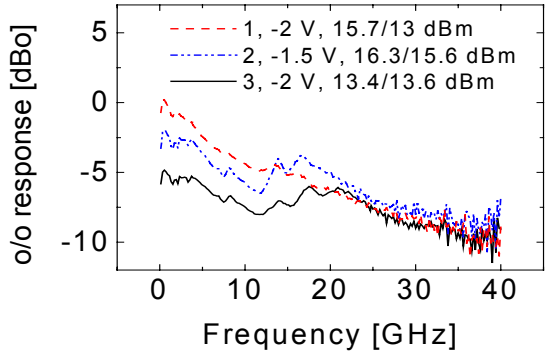

Fig. 3.8. Optical-to-optical frequency response from three different QW structures.

	Type 1	**Type 2**	**Type 3**
Q. W. depth	Deep	Shallow	Shallow
Pad Size	Small	Large	Small
E/o, -3 dBe	> 20 GHz	16 GHz	24 GHz
O/o, -3 dBe	5 GHz	19 GHz	24 GHz

Table 3.1. Summary of –3 dBe bandwidths for e/o and o/o small signal modulation.

The results in Table 3.1 show that the e/o modulation is much more dependent on the electrical pad capacitance of the device than is the case

for the o/o modulation. In case of e/o modulation the p-i-n structure can be approximated by a first-order RC lowpass filter, which is characterized by an effective capacitor C and an effective resistance R. The transfer function of such a system is given by [138]:

$$H(f) = \frac{1}{1 + i \cdot f / (2\pi RC)} \tag{3.18}$$

The 3 dB bandwidth is thus determined by the RC constant. Assuming the p-i-n structure forming a parallel plate capacitor, the effective capacitor C is then proportional to the pad size ($C=\varepsilon A/d$, ε is the dielectric constant, A the pad size, d the thickness of the active region). Hence, the larger the pad size, the lower the bandwidth.

On the other hand there is a very dramatic dependence on the well depths for the o/o modulation (e.g. deep wells: -3 dBe at 5 GHz, shallow wells: 24 GHz). A component of type 2 with a large pad capacitance can have its modulation bandwidth improved when using o/o modulation. This component has previously been shown to enable 80/10 all-optical demultiplexing, but could not perform 40/10 e/o demultiplexing.

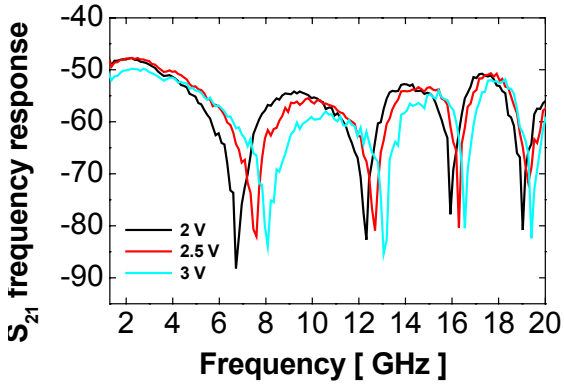

Fig. 3.9. The S21 response of the o/o modulated signal transmitted over 70 km SMF (measured on Type 3).

Fig. 3.9 shows the measured frequency response of the o/o light after transmission through 70 km of SMF fibre. From the positions of the deeps, α-parameters can be deduced (see Section 2.3.2). In this

experiment we investigate the influence of reverse bias and probe wavelength on chirp values of the wavelength-converted signal.

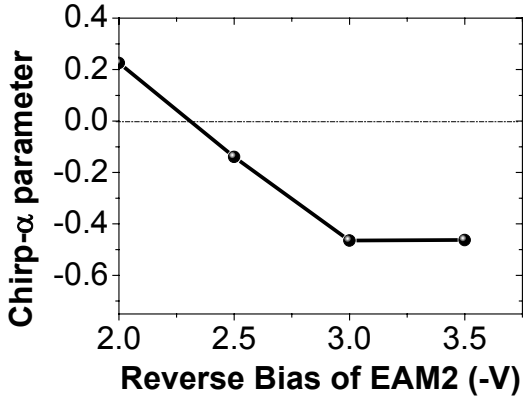

Fig. 3.10. Chirp-α parameter versus reverse bias.

With a fixed bias on EAM1, the transmission response at different EAM2 biases is measured; the results are shown in Fig. 3.10. The trend of a reduced α value with increased bias is clearly seen; zero chirp is obtained around –2.3 V.

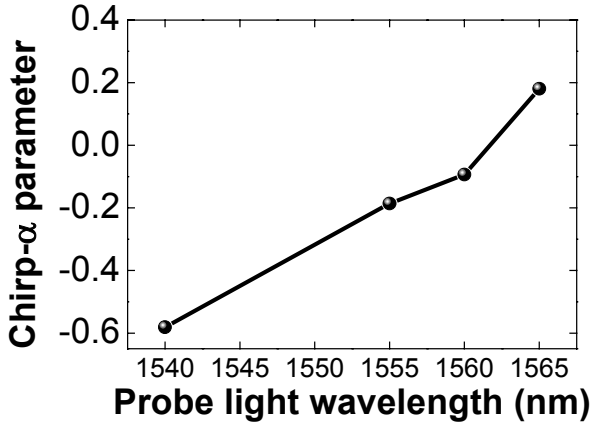

Fig. 3.11. Chirp-α parameter versus wavelength.

In Fig. 3.11, where the bias of EAM2 is –2.5 V and the original signal is fixed at 1546 nm, it is shown that shorter probe wavelengths have lower α values, and zero chirp is achieved around 1561.7 nm. From these

results it can be concluded that there is a possibility, by optimising the bias and the wavelength, to lower or achieve completely negative α by EAM-based wavelength conversion.

3.6 Summary

In summary, starting with an introduction to the band-filling effect and the field-screening effect we have in this chapter discussed the principle of the cross absorption modulation in an EAM and introduced a simple model. Based on this model the static characteristics of an EAM under optical excitation are investigated theoretically; the results indicate the capability of an EAM used for wavelength conversion and 2R regeneration.

The o/o bandwidth and frequency chirp are experimentally investigated. It is found that the o/o modulation bandwidth drastically depends on the quantum well depth while the e/o modulation bandwidth is mainly influenced by the electrical bonding pad size. A device of a small pad and shallow wells shows 24 GHz bandwidth for both e/o and o/o modulation. Given a large bonding pad and shallow wells for an EAM the modulation bandwidth can possibly be improved by o/o modulation. In the o/o chirp measurements very small and negative chirp α–parameters are obtained. Depending on the operating wavelength and the bias the chirp α–parameter ranges from –0.6 to 0.2. It is also found that higher biases and shorter wavelengths are preferred to obtain a small or negative chirp α–parameter. Our experimental investigations show an advantage of using XAM in an EAM for wavelength conversion; namely that the bandwidth of the component may be increased by optical modulation and that the chirp of the converted signal may be tuned at a quite low level. This finding strongly encourages the use of EAMs for wavelength conversion in high bit rate long-haul systems where cascading several wavelength converters is very frequent.

4

All-optical wavelength conversion

To efficiently utilize the enormous bandwidth provided by optical fibres wavelength division multiplexing has been widely used in today's optical networks. Multiple WDM channels can be operated on a single fibre simultaneously and these channels can be independently modulated and detected. In wavelength-routed networks [139], end-to-end lightpaths are set up as optical pipes between source-destination nodes and it is possible to rout data to their respective destinations based on their wavelengths. To improve the switch resolution an optical packet layer has been proposed [140], forming a packet switching wavelength-routed optical network. In these WDM networks, either wavelength switching or packet switching, wavelength conversion plays an important role.

The number of wavelengths in WDM networks determines the number of independent wavelength addresses or paths. Although this number may be large enough to fulfil the required capacity, it is often not large enough to support a large number of network nodes. The blocking probability rises when two channels at the same wavelength are to be routed at the same output. This is known as wavelength contention or wavelength continuity constraint. One method to handle such blocking is to buffer the packets waiting for the correct output wavelength to become available. If buffers are insufficient, the packet is either discarded and lost, or misrouted. Realizing the optical buffer by fibre delay-lines as proposed in [141] requires a fibre length up to 1.6 km at 2.5 Gb/s, which is of concern for reasons of complexity, stability and compactness. Another scheme using an optical loop consisting of a SOA-based Michelson interferometer can operate at 10 Gb/s [142]. However, this scheme is still quite complex as a single optical cell storage device. Alternatively, wavelength conversion can be employed to remove this blocking. If the correct output wavelength is not available, the packet may be converted to another available wavelength on the desired output fibre. It has been shown that wavelength conversion can be used to reduce the probability of blocking in both circuit-switching [143-145] and optical packet

switching networks [140,146,147]. The bit rate of a single channel in WDM networks has been increased from 2.5 to 40 Gb/s or in the future perhaps even up to 160 Gb/s by using optical time division multiplexing technology to accommodate larger network capacity. For these applications wavelength converters should have a large tuning range and be able to operate at 40 Gb/s or beyond.

Traditional wavelength converters involve optical-electrical-optical (O-E-O) conversion and are limited by the processing speed supported by electrical circuits. For future all-optical networks, optical solutions are required. All-optical wavelength conversion can be performed by using the data signal to optically modulate a continuous wave (cw) light beam at a different wavelength. As discussed in Chapter 1, all-optical wavelength conversion at speeds up to 160 Gb/s has been achieved using either the ultra-fast nonlinearities [148] of optical fibres [13] or SOA-based interferometers [24]. These schemes are, however, quite complex. Single EAM based wavelength converters [59-61,62-64,149-153] are more attractive due to its compactness as well as the simple structure.

In this chapter, the principle of EAM-based all-optical wavelength conversion is first discussed. Then we will present our experimental investigations for various system configurations, including wavelength conversion of a single channel and multiple channels at 40 Gb/s. Finally, the results will be summarised and discussed.

4.1 Principle of wavelength conversion

In the last chapter we have discussed the static characteristics of EAM-based wavelength conversion by simulating the propagation of two continuous wave optical signals working as the pump and probe. The static ER of the converted signal was also presented and the existence of an optimum device length was predicted. Now we study the dynamical performance for optical pulses; the scheme is schematically shown in Fig. 4.1. At the input of an EAM, green pulses present the control signal containing data information and the blue line is the cw probe. At the output the control signal is attenuated due to absorption and coupling loss and the data information is transferred onto the cw light as indicated by blue pulses through cross absorption modulation. Thus, when a control pulse is present it reduces the absorption of the cw signal. An optical band

pass filter is used to separate the two signals by blocking the control signal and letting the converted signal pass through.

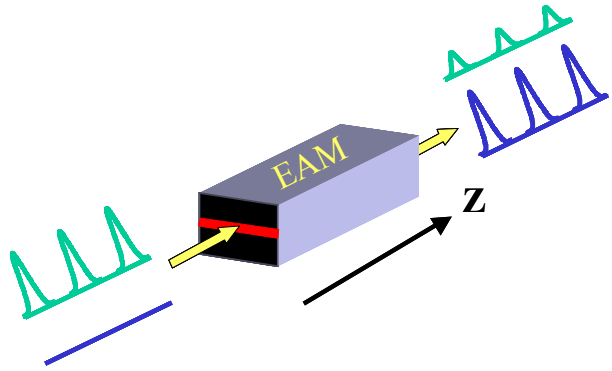

Fig. 4.1. Schematic of EAM-based wavelength conversion.

In principle, the signal evolution inside EAM can be measured by use of various EAMs of different length. This method is, however, not practical because it is very difficult to cleave very short EAMs accurately and a large number of samples are needed to get high length resolution. The study of the signal evolution inside an EAM is thus carried out theoretically using the o/o modulation model introduced in Chapter 3.

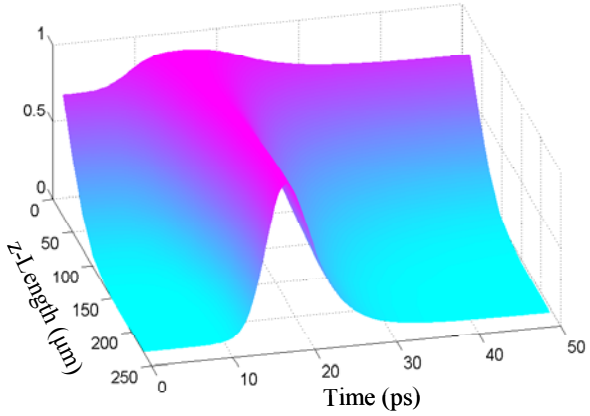

Fig. 4.2. Evolution of the converted pulse along the device.

To simulate the dynamics of cross absorption modulation, we first describe the representation of the two signals involved in this process.

The control signal is a PRBS pulse stream at 40 Gb/s. The control pulse has a full width half maximum (FWHM) of 8 ps and centre wavelength of 1540 nm, with an initial ER of 10 dB and average power 22 dBm. The cw probe has a wavelength of 1550 nm with an average power of 10 dBm. The evolution of the normalized converted pulse along the EAM is shown in Fig. 4.2 as a function of time and z-coordinate along the waveguide. The vertical axis is the optical power normalized such that the peak power of the converted pulse is fixed at unity.

As seen from Fig. 4.2, at the initial stage of propagation along the device (<50 μm), the converted pulse has quite large pulse width and poor extinction ratio, as indicated by the high pedestal and the wide pulse contour. This can be understood by recalling the carrier density dependence of absorption and recovery time discussed in the last chapter. For short device length, the attenuation is small and the control signal still has high power. Due to the finite initial ER, high average power means large pedestal power, which leads to less effective modulation of carrier density and therefore low ER of the converted pulse.

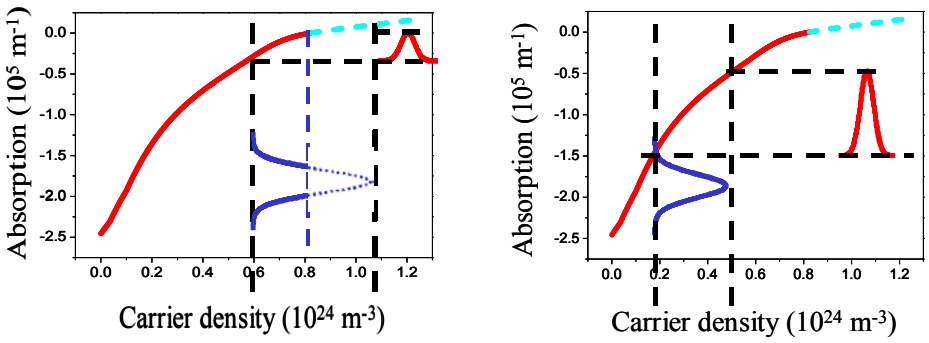

Fig. 4.3. Demonstration of modulation efficiency at (a) high and (b) low carrier density.

This effect is illustrated in Fig. 4.3 (a), where the blue and red pulses represent modulation of carrier density and absorption coefficient, respectively. Carrier density modulation, as represented by the blue pulse, is mainly due to absorption of the pump. Assuming the device is fast enough, the carrier density then follows the variation of the control signal and thus takes the shape of the pump pulse. It should be noted, however, that a carrier density larger than the transparency value (corresponding to zero absorption coefficient) is not possible for a reverse-biased EAM, since above transparency there is no absorption and the carrier density

stops increasing, as indicated by the red pulse at the top right corner of Fig. 4.3 (a). It is then clear that high pump power may actually result in less efficient carrier density modulation.

We have discussed in chapter 3 a sweep out time model to include the field-screening effect on the carrier recovery. The expression for the sweep out time is repeated as below,

$$\tau_{so}(N) = \frac{\tau_0 \tau_{tr}}{\tau_{tr}(1 - \frac{N}{N_{tr}}) + \tau_0 \frac{N}{N_{tr}}} \tag{3.5}$$

where τ denotes the sweep out time, N the carrier density, τ_0 and τ_{tr} are the sweep out time constants at low densities (8 ps) and that at transparency (25 ps) and N_{tr} is the transparency carrier density. The relation between the sweep out time and the carrier density is displayed in Fig. 4.4. It is found that the device with a high carrier density recovers slowly due to the field-screening effect and hence the converted signal acquires a broad pulse width at the early part of its propagation along the EAM.

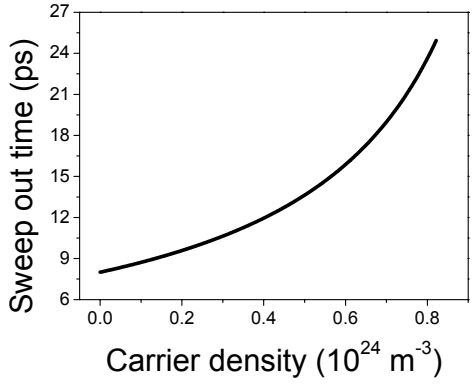

Fig. 4.4. Calculated (Eq. 3.5) sweep out time versus carrier density.

Due to propagation in the EAM, the pedestal of the converted pulse is pulled down and meanwhile the pulse is narrowed. One reason is that the control pulse looses its power and results in a small carrier density change, which increases the modulation efficiency as illustrated in Fig. 4.3 (b) and reduces the carrier recovery time. In addition, the control pulse and the

converted pulse themselves also experience non-linear absorption as discussed in chapter 3; this also contributes to the improvement of the ER and the reduction of the pulse width. The effect demonstrated in Fig. 4.3 is called bleaching effect and will be used for discussions hereafter to explain the pump power optimization.

4.2 Experimental investigations

In this section we present our experimental investigations on all-optical wavelength conversion using XAM in an EAM.

4.2.1 RZ signal at base rate of 10 Gb/s

Set-up

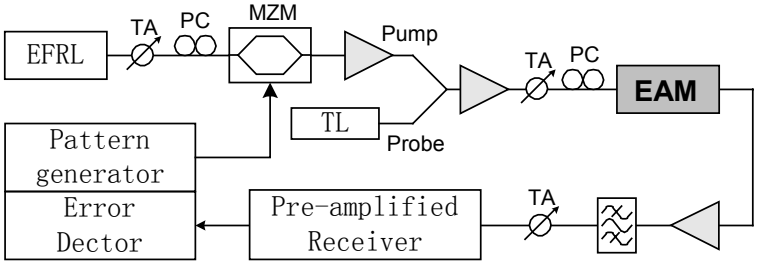

Fig. 4.5. Setup for wavelength conversion at 10 Gb/s.

The experimental set-up is shown in Fig. 4.5. A mode-locked fibre ring laser (ML-FRL), operating at 1550 nm, generates a short optical pulse train at 10 GHz with pulse width of 2.5 ps, which is then intensity modulated in a Mach-Zehnder modulator (MZM) forming the pump signal at 10 Gb/s. The bias of the MZM and the peak-to-peak amplitude of the electrical signal are around 2 V and 5V, respectively. The modulated RZ signal is amplified to an average power of 13 dBm by an optical pre-amplifier of low-noise-figure. The probe beam, generated by a tuneable laser operating at 1555 nm, is combined with the pump beam through a 3 dB coupler and then amplified by a booster amplifier to an

average power of 20 dBm. A tuneable attenuator (TA) and a polarization controller (PC) are employed to adjust the optical power as well as the polarization of the input to the EAM.

At the output of the EAM, the signal is first amplified to compensate for the power loss due to absorption and coupling, and is then launched into an optical band pass filter to block the original signal. The converted signal is afterwards injected into a pre-amplified receiver connected to the error detector for bit-error-ratio (BER) measurement.

The EAM used here has an insertion loss (fibre to fibre) of about 16 dB at 1550 nm and a static extinction ratio of 15 dB/3 V. The bias applied to the EAM was –2.5 V.

Experimental results

The measured BER curves (BER versus the optical power into the pre-amplified receiver) are shown in Fig. 4.6, where the eye diagrams of the original and the converted signal are depicted as insets. As seen from the eye diagrams, the converted signal has very clear and open eyes indicating the successful wavelength conversion.

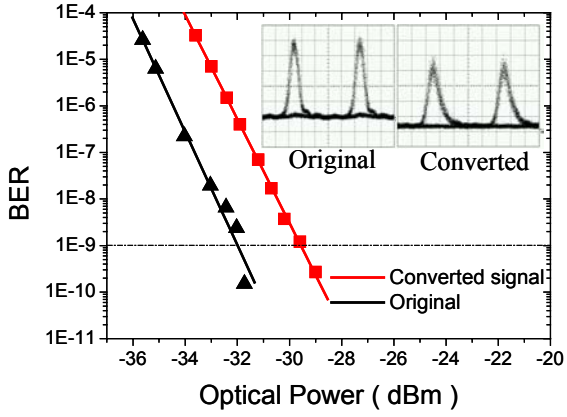

Fig. 4.6. BER of the original and the converted signal at 10 Gb/s, the insets show the respective eye diagrams.

However, the quality of the converted signal is not as good as that of the original signal. Firstly, as shown in the eye diagrams, there is a quite long tail of the converted signal that is the fingerprint of the slow

response of the EAM, implying that the carrier density in the EAM can not follow the change of pump power. The absorption of the trailing edge is thus influenced by the leading edge-generated carriers, which should have been swept out of the intrinsic region if the EAM had fast enough response speed. As a result, a reduced absorption is effective on the trailing edge leading to the tail shown in the eye diagram. This is not very harmful at 10 Gb/s, since no inter-symbol-interference (ISI) has arisen. But when the bit rate increases up to 40 Gb/s, this tail will cause significant ISI and bit errors and therefore should be avoided by increasing the EAM's o/o modulation bandwidth with careful design.

Secondly, a noisy pulse peak of the converted signal is observed. Unlike an SOA, an EAM doesn't generate ASE noise since no optical gain is involved. The noise in this case arises from all the optical amplifiers used in the set-up since any optical amplifier introduces ASE noise. For this experiment, the primary noise source is the amplifier right after the EAM because of the quite low optical power at the output of the EAM (about –18dBm). The following band pass filter can only cut off the out-of-band noise, leaving the in-band noise unchanged. Therefore, reducing the insertion loss of the EAM will be helpful to get a high signal-to-noise ratio (SNR) of the converted signal. As discussed in chapter 3 the non-linear power transfer function of an EAM can suppress low-power intensity variations; the transfer function explains the quite flat pedestal of the converted signal.

Finally, as indicated by the BER results, the converted signal leads to a receiver sensitivity of –29 dBm. Compared to the original signal (-32 dBm), a 3 dB power penalty is thus introduced by the EAM-based wavelength conversion.

4.2.2 OTDM signal at 40 Gb/s

In this subsection we present our experimental results of wavelength conversion at 40 Gb/s and investigate the influence of operative parameters, including pump light power, reverse bias of the converter and probe light wavelength on the wavelength-converted signal, including its chirp performance [151].

Set-up

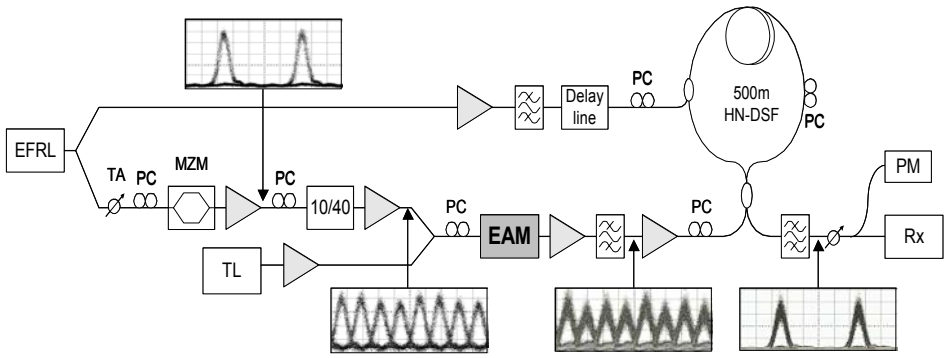

Fig. 4.7. Set-up for wavelength conversion at 40 Gb/s. EFRL: Erbium fibre ring laser, TA: Tunable attenuation, PC: Polarization control, TL: Tunable laser.

The experimental set-up is shown in Fig. 4.7. An erbium fibre ring laser (EFRL), working at 1552nm, generates short optical pulses at 10GHz which are data modulated by a MZ modulator and then optically multiplexed to 40Gb/s, to be used as the pump signal. The probe light, generated by a tunable laser (TL), is injected into the EAM together with the pump signal, and through the process of XAM the pump data signal is transferred to the probe. The converted signal is afterwards demultiplexed back to 10Gb/s by a non-linear optical loop mirror (NOLM) which consists of 500m highly non-linear dispersion-shifted fibre (HN-DSF).

In Fig. 4.8 the eye diagram of the original signal at 1552nm and that of the converted signal at 1561nm are depicted, together with the signal demultiplexed by the NOLM. In this case the receiver sensitivity for 10^{-9} BER is about –26.6dBm, which can be further improved by optimising the receiver and the NOLM.

Based on this set-up, by varying the pump power as well as the reverse bias of the EAM and the probe wavelength, a clear picture of the EAM-based wavelength conversion can be obtained.

Pump power and bias dependence

As discussed in chapter 3, the XAM occurring in an EAM can be explained by the fact that when two beams, referred to as the pump and probe beam, are launched into an EAM, the photon-generated carriers due to the absorption of the pump beam of higher power have the effects of

band-filling and screening the electric field imposed on the device, thereby lowering the probe absorption. This results in a higher output of the probe in the presence of a logic “1” in the data-encoded pump signal, thus transferring the data to the new (probe) wavelength. The performance of the wavelength conversion in an EAM is thus directly related to the power difference between the “1” and “0” levels of the pump.

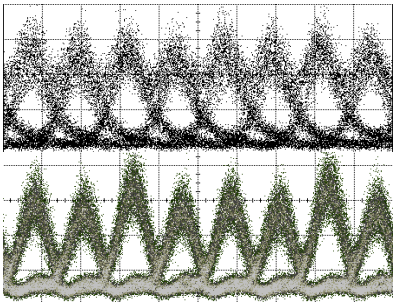

Fig. 4.8. The converted signal at 40 Gb/s with pump power levels of 16dBm (upper) and 20dBm (lower).

In Fig. 4.8 we compare two cases with pump power of 16 dBm and 20 dBm, the eye diagrams show that higher pump power leads to a better eye-opening, suggesting that the XAM process is more efficient at this pump level. The BER quoted above is obtained at 20dBm while it wasn’t possible to achieve such a low BER at a pump power level of 16dBm.

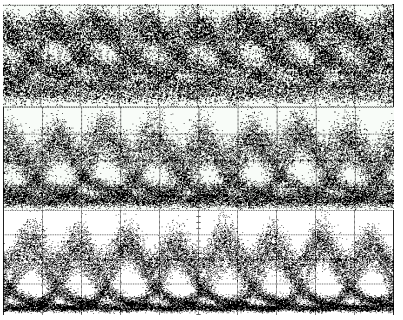

Fig. 4.9. The converted signal at 40 Gb/s for a pump power of 16 dBm with reverse bias levels of -1.5 V (upper), -2.0 V (middle) and -2.5 V (lower).

The dependence of bias voltage of the EAM is also studied at 16dBm pump light. As shown in Fig. 4.9 under fixed pump power higher reverse bias is beneficial. Lower bias thus leads to a long “tail” in the eye diagram,

which is attributed to a longer carrier recovery time under weak electric field. It should be noted that although the present results indicate higher pump power to be beneficial, one should be careful in the use of excessive pump power levels. Since the number of photon-generated carriers increases with pump power, the recovery time may be increased. This may be counterbalanced by the use of a higher reverse bias, which may, however, also increase the insertion loss of the device. Beyond this, the reliability of an EAM under such extreme conditions also needs consideration.

With reference to previous chirp measurement as discussed in Chapter 3 Section 3.5, the frequency chirp of the wavelength-converted signal also depends on the bias. As shown, higher bias leads to lower or even negative chirp α-parameter, which is desirable for long haul lightwave systems when dispersion compensation is considered.

Probe wavelength dependence

The performance at various probe wavelengths has also been investigated. Generally the original signal at 1552 nm can be converted to any wavelength ranging from 1537 nm to 1564 nm, and in all cases clear and open eyes are observed. This suggests that the EAM-based wavelength conversion has a wide wavelength tuning range.

It has been demonstrated in Chapter 3, that shorter wavelength has lower chirp α-parameter. In addition, the choice of the probe wavelength also has an impact on the conversion efficiency. With reference to [134], focusing on the band-filling effect, it is not desirable to use long wavelengths that are close to the band edge for the probe. This is because the change in absorption close to the bandgap is relatively small due to the low density of states. On the other hand, the absorption increases at shorter wavelengths, leading to a reduced optical power at the output. The tradeoff between the effective o/o modulation and the output power will be discussed in detail later in this chapter.

4.2.3 8 × 40 Gb/s OTDM wavelength conversion

Investigations on wavelength conversion have so far focused on conversion of only one wavelength. In advanced WDM networks, however, applications like network broadcasting require a multi-

wavelength optical data source where more than one converted wavelength is involved. It is therefore a relevant task to investigate the potential of a wavelength converter for multiple channel conversion.

In this subsection we present an EAM-based multiple wavelength conversion scheme where multiple WDM channels are data-encoded simultaneously by a 40 Gb/s signal through XAM in a single EAM [152]. All the wavelength-converted channels are compliant with the ITU-T proposal on the WDM wavelength grid.

Set-up

The experimental setup is shown in Fig. 4.10. The outputs of eight distributed feedback lasers (DFB-LD) with a wavelength spacing of 1.6 nm are combined in an arrayed-waveguide grating (AWG) 1. These lasers operate at the ITU-standardized wavelengths of 1549.31 nm (λ1), 1550.90 nm (λ2), 1552.52 nm (λ3), 1554.12 nm (λ4), 1555.72 nm (λ5), 1557.33 nm (λ6), 1558.96 nm (λ7) and 1560.60 nm (λ8). The combined signal of the eight channels is amplified to an average power of 15 dBm, and injected into EAM2 from the right port.

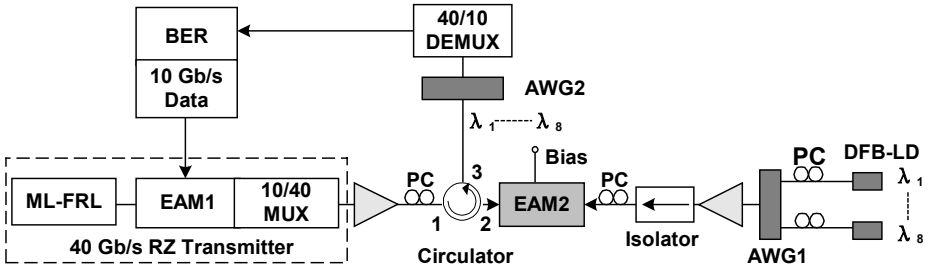

Fig. 4.10. Set-up for 8×40Gb/s OTDM wavelength conversion.

The control laser is a mode-locked fibre ring laser (ML-FRL) operating at 1545 nm, which generates 2.5 ps (FWHM) pulses with a repetition rate of 10 GHz. The control pulses are modulated in a packaged electroaborption modulator (EAM1) by a pseudorandom bit sequence (PRBS) of length 2^{15}-1 from a 10 Gb/s pattern generator, resulting in an RZ data signal at 10 Gb/s which is then optically multiplexed to 40 Gb/s by a fibre-based timing interleaver. The generated 40 Gb/s signal is amplified to an average power of 16 dBm, and injected into EAM2 from

the left port. Due to the counter-propagating configuration used for EAM2, an isolator (right side) and an optical circulator (left side) are used. The 3rd output of the circulator is connected to another commercial AWG2, which selects out each wavelength from the combined WDM signal. The converted signal at one wavelength is afterwards demultiplexed back to 10 Gb/s by a non-linear optical loop mirror (NOLM), which consists of 500 m highly non-linear dispersion-shifted fiber (HN-DSF). A pre-amplified receiver is used for BER measurement.

Experimental procedures and results

In our experiment two tapered fibers are used to couple light into and out of EAM2. Having optimized the coupling between EAM2 and the tapered fibers at 1550 nm, the fiber-to-fiber loss at zero bias is about 10 dB. The static transfer curve (transmittance as function of bias) is a quasi-linear curve up to about -2.5 V with a slope of –9 dB/V. The bias of EAM2 is set to –2 V in the experiment, yielding a potentially high saturation induced extinction ratio. The polarizations of the eight channels are optimized individually by use of eight polarization controllers (PC). The polarization of the control signal is adjusted by its own PC and remains unchanged once optimized.

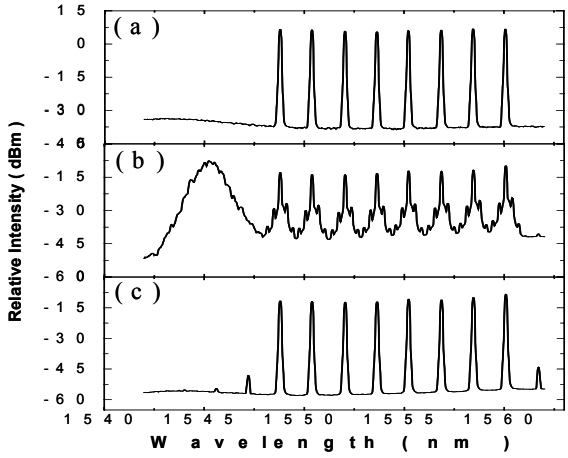

Fig. 4.11. Spectra of the WDM signals (8×40Gb/s) at (a) input of EAM2, (b) output of EAM2 with the control signal injected, (c) output of EAM2 without control signal.

Fig. 4.11 depicts the spectrum of the eight channels in three cases: (a) at the input of EAM2, (b) at the output of EAM2 with the control signal

and (c) at the output of EAM2 without the control signal. It is clearly seen that in the presence of the control signal all channels are modulated due to XAM and each acquires a broadened spectrum as shown in Fig. 4.11 (b). In case of no control signal, we find new frequency components at the output of the EAM as shown in Fig. 4.11 (c). The new components are the fingerprint of Four Wave Mixing (FWM) in the EAM; they are 30 dB weaker than the original signals, and hence their impact is negligible.

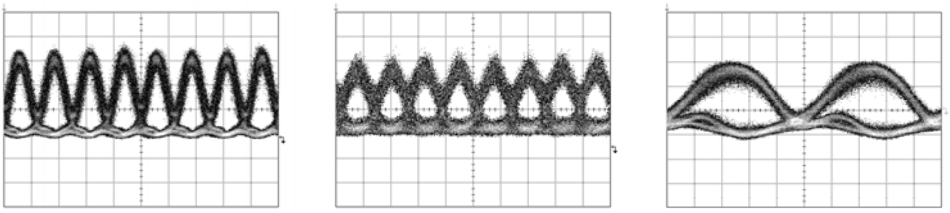

(a) (b) (c)

Fig. 4.12. The eye diagrams of (a) the original and (b) the converted signals at 40 Gb/s. (c) shows the converted signal demultiplexed down to 10 Gb/s and after a low pass filter.

As an example, we display in detail the performance of the channel at 1555.7 nm in Fig. 4.12 and 4.13. As seen from Fig. 4.12, showing the eye diagrams of the original and the converted signals, the converted signal has clear and open eyes that are comfortably error free.

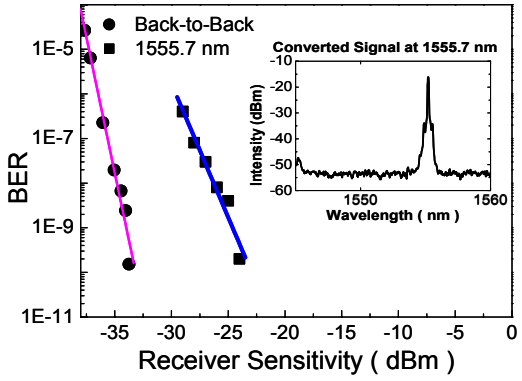

Fig. 4.13. The BERs of the control signal and the converted signal at 1555.7 nm at 40 Gb/s. The inserts show the spectrum of the converted signal.

BER curves are shown in Fig. 4.13, where the spectrum of the converted signal is also displayed for illustration. It can be seen that AWG #2 filters out one wavelength with a side mode suppression ratio larger than 30 dB. The BER measurement shows that the converted signal at 1555.7 nm has no error floor but indicates a power penalty of 8 dB compared to the control signal. This penalty is mainly due to the reduced signal-to-noise ratio (SNR) resulting from the insertion loss of the EAM, but is also due to the decreased ER stemming from the insufficient cross absorption modulation in the EAM.

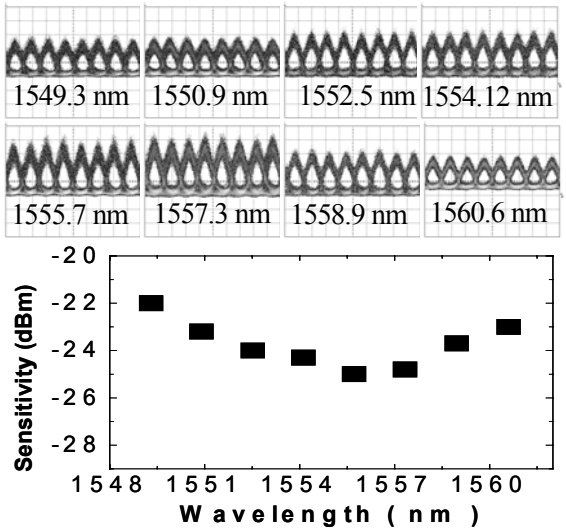

Fig. 4.14. 40 Gb/s eye diagrams and receiver sensitivities of all the converted signals.

The 40 Gb/s eye diagrams of all the eight channels are displayed in Fig. 4.14, where the receiver sensitivities at different wavelengths are depicted for an overview comparison.

It is found that all the converted channels have clear and open eyes and are error free. We also find that the wavelength near 1555 nm has the best receiver sensitivity as suggested by the local minimum seen in Fig. 4.14. This can be understood by recalling the widely used BER expression [154]:

$$BER = \frac{1}{2} erfc(\frac{Q}{\sqrt{2}}) \tag{4.1}$$

The BER is determined by a system quality parameter Q,

$$Q = \frac{I_1 - I_0}{\sigma_1 + \sigma_0} \tag{4.2}$$

where I_1 and I_0 are the photodiode currents in response to the optical mark and space signals, σ_1 and σ_0 are the standard deviations of the mark and space noise, respectively. The system quality parameter Q is then proportional to the differential photocurrent ($I_1 - I_0$) and inversely proportional to the sum of the corresponding noises ($\sigma_1 + \sigma_0$).

The photocurrent is directly proportional to the incident optical power and then,

$$I_1 = RGP_1 \tag{4.3}$$

$$I_0 = RGP_0 \tag{4.4}$$

where R is the responsivity of the photodetector, G is the gain of the pre-amplifier in the receiver, P_1 and P_0 denote the optical powers of the mark and space signals at the EAM output. The receiver noise consists of signal-ASE beat noise, ASE-ASE beat noise, short noise and thermal noise, as give by [154, 155],

$$\sigma_{s-sp} \approx 2\sqrt{R^2 G S_{sp} \Delta f}\sqrt{P} \tag{4.5}$$

$$\sigma_{sp-sp} \approx \sqrt{R^2 S_{sp}^2 \Delta f (2\Delta f_o - \Delta f)} \tag{4.6}$$

$$\sigma_{shot} \approx \sqrt{2qRG\Delta f}\sqrt{P} \tag{4.7}$$

$$\sigma_{thermal} = \sqrt{4k_B T \Delta f / R_L} \tag{4.8}$$

where S_{sp} is the spectral density of spontaneous emission induced noise, P the signal power, Δf the detector bandwidth, Δf_o the optical bandwidth,

q the electron charge, k_B the Boltzman constant, T the absolute temperature, and R_L the load resistor. For the mark signal that normally has high power, we take into account the signal-ASE beat noise and the short noise ($\sigma_1=(\sigma_{s\text{-}sp}^2+\sigma_{shot}^2)^{1/2}$), the standard variance of which is proportional to the squared root of the signal power, as given by,

$$\sigma_1 \approx \sqrt{4R^2GS_{sp}\Delta f + 2qRG\Delta f}\sqrt{P_1} \tag{4.9}$$

For the space signal we consider the ASE-ASE beat noise and the thermal noise, which are independent of the signal power, as given by,

$$\sigma_0 \approx (\sigma_{sp-sp}^2 + \sigma_{thermal}^2)^{1/2} \tag{4.10}$$

By substituting Eqs. (4.3-4.4) and (4.9-4.10) into Eq. (4.2), we obtain,

$$\frac{1}{Q} = \frac{\sqrt{4R^2GS_{sp}\Delta f + 2qRG\Delta f}\sqrt{P_1} + \sigma_0}{RG(P_1 - P_0)} \tag{4.11}$$

It is thus found that the Q parameter is characterized by P_1 and P_0. Recalling that the average power $\overline{P} = (P_1 + P_0)/2$ and the extinction ratio $ER = 10\log(P_1/P_0)$, the optical power of mark and space signals can then be expressed in terms of the average power and the extinction ratio:

$$P_1 = \frac{2\overline{P}}{1+10^{-ER/10}} \tag{4.12}$$

$$P_0 = \frac{2\overline{P}}{1+10^{ER/10}} \tag{4.13}$$

By substituting Eqs. (4.12) and (4.13) into (4.11), we obtain

$$\frac{1}{Q} = \frac{\sqrt{4R^2GS_{sp}\Delta f + 2qRG\Delta f}}{\sqrt{2\overline{P}}}\frac{1}{f_{ER}^1} + \frac{\sigma_0}{RG}\frac{1}{2\overline{P}}\frac{1}{f_{ER}^0} \tag{4.14}$$

We have here introduced two ER factors as given by,

$$f_{ER}^{1} = \frac{10^{ER/10} - 1}{\sqrt{10^{ER/10}}\sqrt{1 + 10^{ER/10}}} \tag{4.15}$$

$$f_{ER}^{0} = \frac{10^{ER/10} - 1}{10^{ER/10} + 1} \tag{4.16}$$

The Q parameter is then solely characterized by the average power and the ER factors. When the ER is very moderate the receiver noise may be dominated by the signal-noise beat noise and shot noise for both marks and spaces. Using the same approach as discussed above, we obtain,

$$\frac{1}{Q} \propto \frac{1}{\sqrt{2\overline{P}}} \frac{1}{f_{ER}} \tag{4.17}$$

We have introduced an ER factor for this case as given by,

$$f_{ER} = \frac{10^{ER/10} - 1}{(1 + \sqrt{10^{ER/10}})\sqrt{1 + 10^{ER/10}}} \tag{4.18}$$

In Fig. 4.15 the dependence of the three ER factors on the extinction ratio is shown. It is found that in all cases the ER factors increase with the extinction ratio. A general conclusion can then be drawn that to obtain a higher Q parameter, larger average power and larger extinction ratio are both preferred.

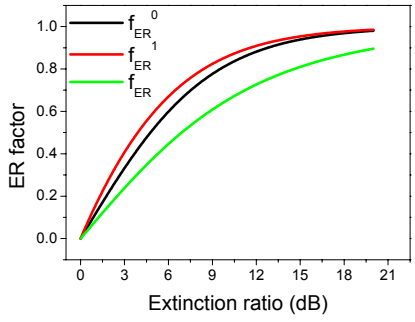

Fig. 4.15. ER factors (Eqs. (4.15), (4.16) and (4.18)) versus the extinction ratio.

As discussed previously, the wavelength-converted signal has a larger extinction ratio at shorter wavelength but also experiences larger loss, leading to a tradeoff dependent on the signal wavelength as suggested by Eqs. (4.14). This tradeoff is reflected in Fig. 4.14, where the highest receiver sensitivity obtained at 1555 nm corresponds to the optimum balance between the ER and the signal power.

4.2.4 7 × 40 Gb/s base rate wavelength conversion

The experiment we just presented is based on 10 Gb/s base rate and the 40 Gb/s signal is obtained through fibre-based interleaving. System performance evaluation, i.e. BER measurement, is performed at the base rate. It is further a challenge to work at a base rate of 40 Gb/s since the signal bandwidth is increased and so is the noise power in the receiver. Generally speaking, an extra 6 dB of signal power is required for a 40 Gb/s base rate system to match that of 10 Gb/s because of the four-fold increase of the (noise) bandwidth. In this subsection we study the case where the base rate is 40 Gb/s and repeat the same investigations as previously carried out for the OTDM 40 Gb/s signal. The results of this experiment are published in [153].

Set-up

The experimental set-up is shown in Fig. 4.16. The outputs of seven commercial distributed feedback lasers (DFB-LD) at a wavelength spacing of 1.6 nm are combined in the arrayed-waveguide grating (AWG)1. These lasers operate at ITU-standardized wavelengths of 1549.31 nm, 1550.90 nm, 1552.52 nm, 1554.12 nm, 1557.33 nm, 1558.96 nm and 1560.60 nm. The combined signal of the seven channels is amplified to an average power of 17 dBm, and injected into the EAM from the right port. The control signal is generated by a commercial RZ transmitter, which basically consists of two Mach-Zehnder modulators (MZM). The first MZM, biased at the peak transmission point and driven by a 20 GHz RF signal, modulates a CW light beam from a tuneable laser operating at 1555.8 nm and generates a 40 GHz stream of pulses with widths of ~8 ps (corresponding to 33 % of the bit-period).

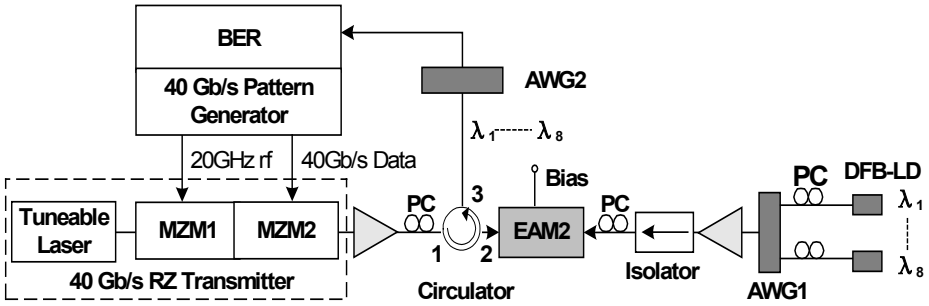

Fig. 4.16. Set-up for 7×40Gb/s base rate wavelength conversion.

The pulse stream is then launched into the second MZM and modulated by a pseudorandom bit sequence (PRBS) of length 2^{15}-1 from a 40 Gb/s pattern generator. The generated RZ signal at 40 Gb/s is amplified to an average power of 17.8 dBm, and injected into the EAM from the left port. Due to the counter-propagation scheme employed, an isolator (right side of the EAM) and an optical circulator (left side) are used. The 3rd output of the isolator is connected to another commercial AWG2, which allows selecting out each of the seven converted channels. A pre-amplified receiver is used for subsequent BER measurements.

Experimental results

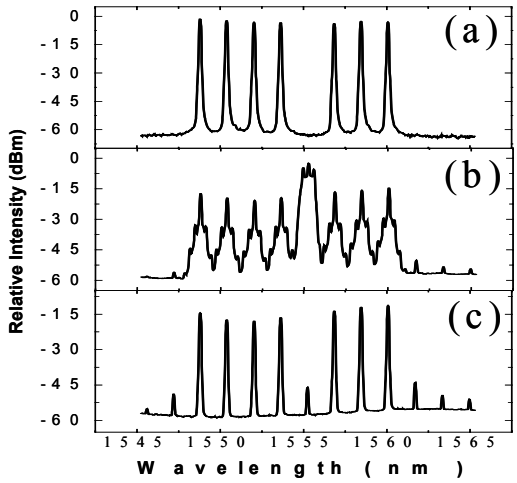

Fig. 4.17. Spectra of the WDM signals (7×40Gb/s) at (a) input of the EAM, (b) output of the EAM when a control signal is injected, (c) output of the EAM without the injection of a control signal.

Fig. 4.17 depicts the spectrum of the seven channels in three cases: (a) at the input of EAM, (b) at the output of EAM when the control signal is injected, and (c) at the output of EAM without control signal. It is clearly seen that in the presence of the control signal all channels are modulated due to XAM and each acquires a broadened spectrum as shown in Fig. 4.18 (b). In case of no control signal, we find new frequency components at the output of the EAM as shown in Fig. 4.18 (c). The new components are the fingerprint of Four Wave Mixing (FWM) in the EAM; they are 30 dB weaker than original signals, hence their impact is negligible.

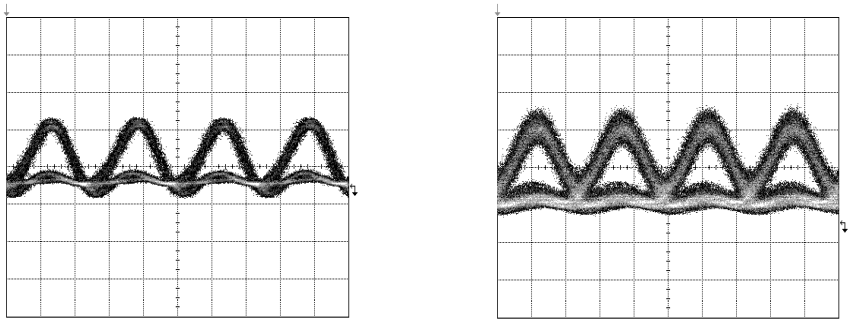

(a) (b)

Fig. 4.18. Eye diagrams of (a) the original and (b) the converted signals at 40 Gb/s base rate.

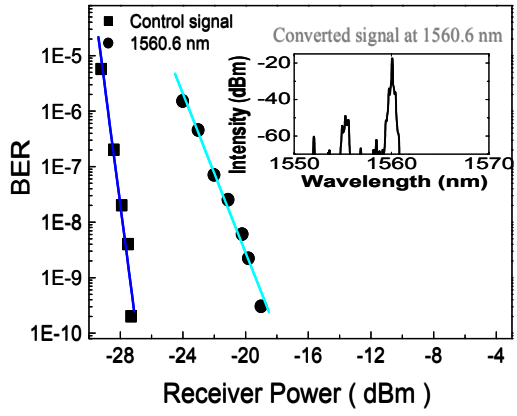

Fig. 4.19. BERs of the control signal and the converted signal at 1560.6 nm at 40 Gb/s base rate. The insert shows the spectrum of the converted signal.

As an example, we display in detail the performance of the channel at 1555.7 nm in Fig. 4.18 and 19. As seen from Fig. 4.19, showing the eye diagrams of the original and the converted signals, the converted signal has clear and open eyes that are error free. BER curves are shown in Fig. 4.20 where the inset shows the spectrum of the converted signal. It can be seen that AWG2 filters out one wavelength with a side mode suppression ratio larger than 30 dB.

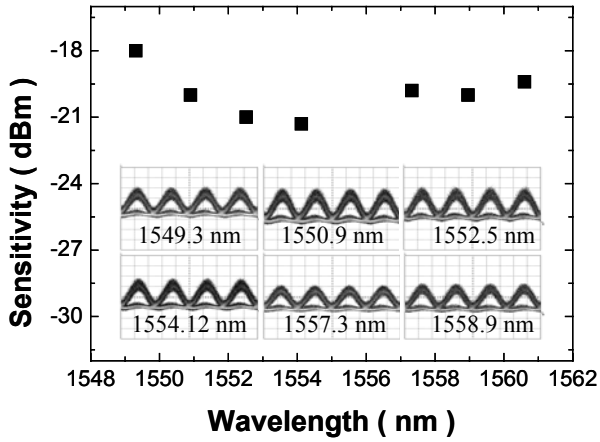

Fig. 4.20. Receiver sensitivity of all seven converted signals at 40 Gb/s base rate. The insert shows the eye diagrams of six channels with wavelength shorter than 1560 nm.

The eye diagrams of the remaining six channels are displayed in Fig. 4.20, where the receiver sensitivity of all seven channels is depicted for an overview comparison. It is found that the other six channels also have clear and open eyes and are error free. We find that the wavelength near 1555 nm has the best receiver sensitivity or lowest power penalty (6 dB) as suggested by the valley shown in Fig. 4.21. The reason has been given in previous discussions.

4.3 Discussion

4.3.1 Optimum operation

From a system point of view, an EAM-based wavelength converter can be optimized by adjusting several key parameters, such as the optical power of pump and probe and the reverse bias applied to the EAM. In section 4.2.2 experimental investigations on system optimization have been presented, accompanied with qualitative explanations. In this section we use our o/o modulation model to simulate wavelength conversion under various conditions to gain more insights. Physical explanations for the optimum pump power and device length are given by evaluation of the ER, average power and pulse width of the converted signal. The parameters used in our calculation are listed in Table 4.1 and Table 4.2.

	Pump	Probe
Wavelength (nm)	1540	1550
Bit Rate	40 Gb/s	cw
Initial ER (dB)	10	-
FWHM (ps)	8	-

Table 4.1. Major signal parameters.

Confinement factor	0.19 - 0.23
Differential gain (10^{-19} m^2)	~ 8
Saturation Power (dBm)	~ 12

Table 4.2. Major device parameters.

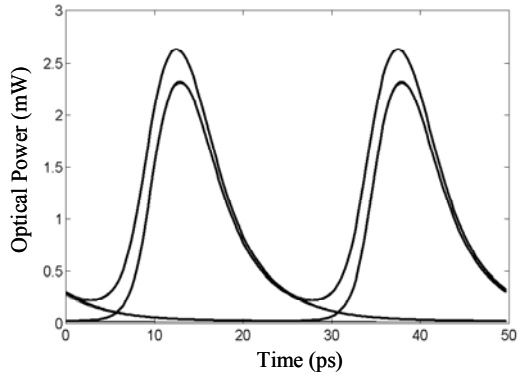

Fig. 4.21. Calculated eye diagrams of the converted signal at 40 Gb/s.

With pump power 22 dBm and probe power 10 dBm we obtain the eye diagram of the converted signal for a device length of 150 μm, as shown in Fig. 4.21.

It is clear that during propagation the converted signal develops multiple levels for logic "1" and "0". This phenomenon is known as the patterning effect since the different power levels are determined by the digital pattern carried by the probe signal. For example, the upper pulses in Fig. 4.21 correspond to at least two continuous "1s" and the lower ones represent a separate mark like the case "010". Pattern effects originate from the finite recovery time or slow response of the EAM. Considering the case of "11", the first pulse is absorbed and the carrier density is increased. When the second pulse arrives, the generated carriers by the first pulse have not yet been swept out and hence the second pulse experiences less absorption, leading to larger output power. In case of "010", the carriers generated by the pulse have more time to recover before the next pulse arrives. However, a long trailing tail is left, which extends into the following bit(s) and causes intra-channel interference. It is therefore obvious that the fast response of an EAM or the short recovery time is of extreme importance. In the following discussions the extinction ratio of the converted signal is defined as the ratio of the lowest peak power to the highest pedestal.

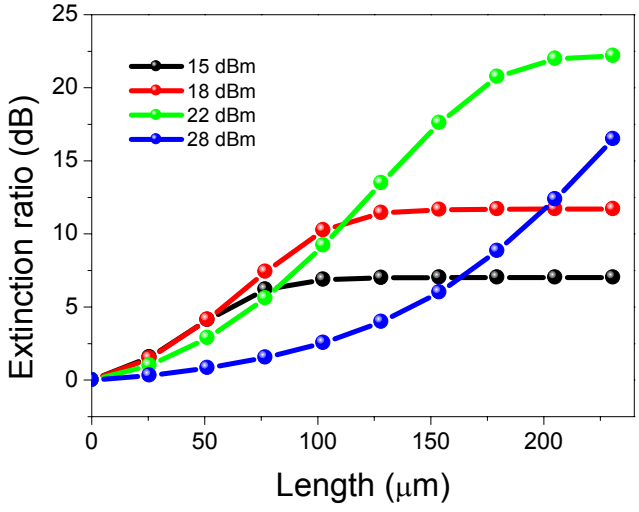

Fig. 4.22. Calculated ER versus device lengths for various pump power levels.

The role of the pump power is investigated by varying the average pump power with all other parameter fixed in our calculation. The extinction ratio of the converted signal versus device length is shown in Fig. 4.22, where four pump power levels are employed.

Generally, for all pump levels, the ER of the converted signal initially increases with propagation length and reaches maximum at a later stage, in agreement with discussions for static characteristics in chapter 3.

For a device as long as 225 μm, a moderately higher pump power generates larger ER, as indicated by the black and red lines representing a power increase from 15 dBm to 18 dBm. This is simply because the increased pump power causes larger carrier density modulation.

However, when we increase the pump power further, e.g., from 18 dBm (red) to 22 dBm (green), for short device length (<100 μm) the ER of the converted signal becomes worse. If we increase the pump power to 28 dBm (blue), it is found that the ER is even lower than that of 15 dBm for device lengths up to 150 μm, and worse than that seen for a pump power of 22 dBm for any device length.

It is hence clear that an optimum pump power exists for a certain device length [134], as clearly illustrated in Fig. 4.23, where the ER of the converted signal at 150 μm for various pump power levels is displayed. The highest ER is in this case obtained at a pump average power of 22 dBm.

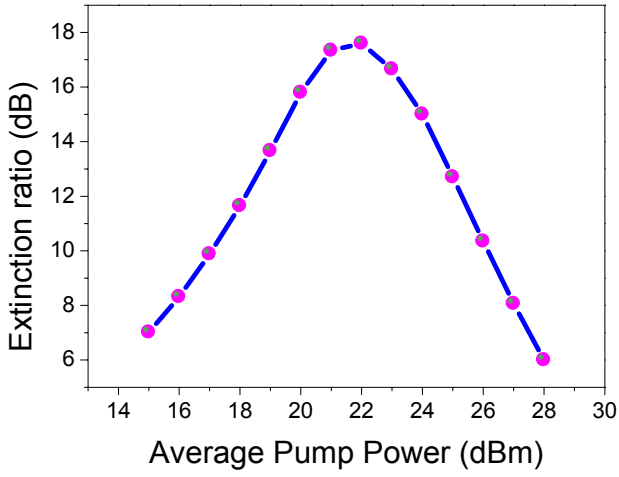

Fig. 4.23. Calculated ER of the converted signal for a device length of 150 μm.

The phenomenon that very high pump power (above the optimum value) leads to low ER can be explained by the absorption bleaching effect, which was discussed in the first section. With finite initial ER, large average power means high pedestal and therefore low modulation efficiency for the carrier density, as previously illustrated in Fig. 4.3, especially for the early stage of propagation where the pump signal still has considerable power. When the input power of the pump is very high, then although the signal looses some power during propagation, the pedestal of the pump still has relatively high power level during propagation through the device. Due to the saturation of absorption, marks and spaces of the pump will experience almost same absorption, leading to poor carrier density modulation and hence low ER for the wavelength-converted signal. The higher the input power of the pump is, the lower the ER of the probe becomes.

It is also found from Fig. 4.22 that propagation at the later stage inside the device has a small contribution to the ER of the probe. For example, there is no significant ER improvement after 125 μm for an initial pump power of 15 or 18 dBm. This observation suggests an optimum device length for certain initial pump power. Another consideration is the power loss due to transmission in a long device. Fig. 4.24 shows how the average power of the probe evolves along the device for various initial pump power levels.

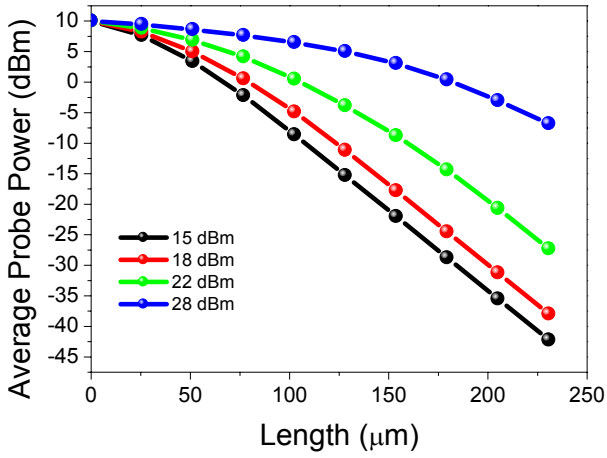

Fig. 4.24. Average power versus device length.

Basically the average power of the probe decreases along the device for all pump power levels. Higher pump power leads to higher probe power due to the larger carrier density and the small absorption coefficient experienced by both. It is therefore tempting to conclude that larger pump power is desirable to get large OSNR at the output of the device. However, as discussed before, the bleaching effect counteracts this by reducing the ER.

This consideration is further elucidated in Fig. 4.25, where the average power and ER of the probe versus device length is depicted for a pump power of 22 dBm. It is clear that the longer the device is, the higher ER and the lower average power the probe has. For example, increasing the device length from 150 μm to 200 μm results in an ER improvement of about 5 dB and a power loss of more than 10 dB. Lower output average power leads to low OSNR and poor receiver sensitivity. The optimum device length is therefore determined by taking into account the trade-off between the ER and the power level of the converted signal.

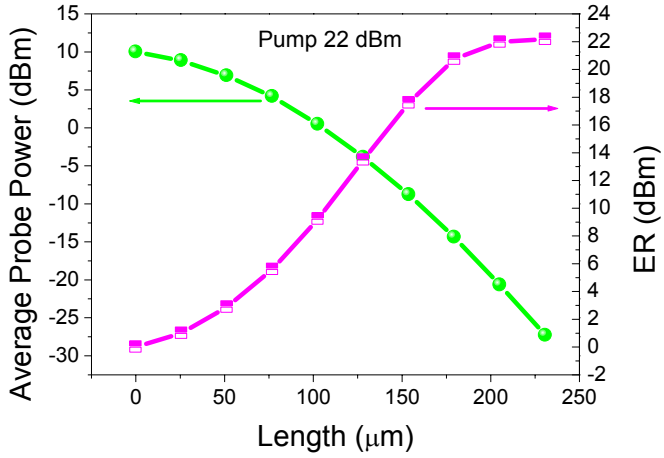

Fig. 4.25. Average power and ER of the probe vs. device length at pump power of 22 dBm.

Finally, we make some comments on the pulse width of the wavelength-converted signal. In the first section of this chapter Fig. 4.2 we have demonstrated how the pulse narrows along the device and a qualitative explanation was given. Here we consider in more detail how the pump power and device length influence the pulse width. Fig. 4.26

shows the pulse width versus device length at three different pump power levels and an initial pump pulse width of 8 ps FWHM.

At low pump power (15 dBm, black) the converted pulses obtains the minimum width of 9.5 ps at about 100 μm and maintain this value under further propagation. Increasing the pump power from 15 dBm to 22 dBm, we find that the pulse width continues to decrease during propagation and reaches its minimum of about 6 ps at the output. A further increase of pump power, e.g., from 22 dBm to 28 dBm, is found to result in wider pulses compared to the two former cases. Since the pulse width is mainly determined by the carrier density modulation arising from the absorption of the pump signal, the arguments and explanations given above can also be applied here. The results, shown in Fig. 4.26, suggest the optimum pump power to get the narrowest converted pulse to be, for the specific device parameters chosen, 22 dBm at a device length of 150 μm.

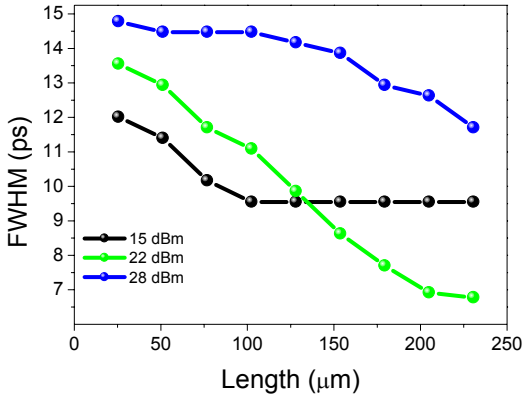

Fig. 4.26. Calculated pulse width versus device length.

4.3.2 Other wavelength conversion schemes

At the beginning of this chapter we reviewed different techniques of all-optical wavelength conversion. Here, for comparison purpose, we extend this topic by briefly demonstrating our experimental results on fibre- and SOA-based wavelength conversion at 40 Gb/s. It should be noted that in this section we do not present the experimental details, instead, we only discuss the principle and present major results. Set-ups given here are all simplified.

XPM and optical filtering

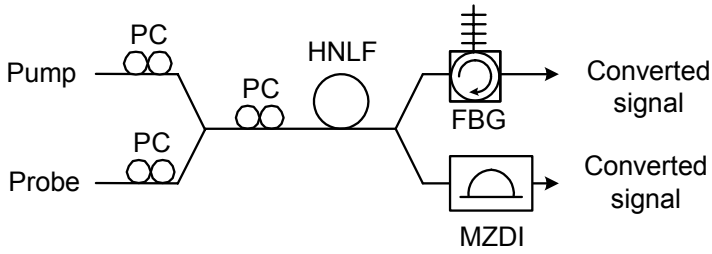

Fig. 4.27. Wavelength conversion at 40 Gb/s using XPM and optical filter.

The first scheme is schematically shown in Fig. 4.27, where PC stands for polarization controller, HNLF highly non-linear fibre, FBG fibre Bragg grating, MZDI Mach-Zehnder delay interferometer. This fibre-based scheme uses cross phase modulation that occurs when the original data signal (used for pump, Fig. 4.28 (a)) and a cw lightwave at a different wavelength (probe) are travelling together in a non-linear fibre [156-158]. As a result of XPM, data information of the pump in the form of intensity variation modulates the phase of probe and the spectrum of the probe becomes broadened as shown in Fig. 4.28 (c).

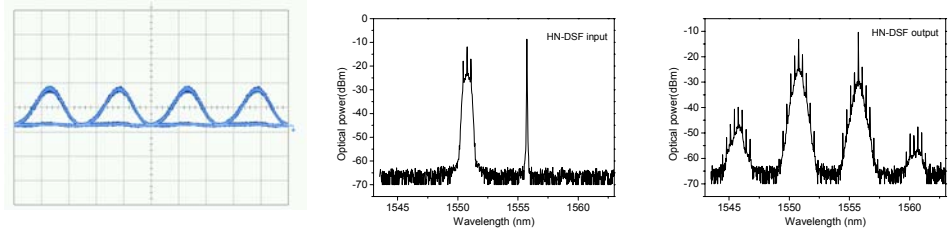

(a) (b) (c)

Fig. 4.28. (a) Eye diagram of original signal at 40 Gb/s, spectrum at HNLF (b) input and (c) output.

By passing the phase-modulated probe signal through an optical filter where the carrier is suppressed, the phase modulation is demodulated and transferred back to intensity variation. We investigated two different optical filters for phase demodulation, i.e., an FBG and an MZDI. The waveform and spectrum of the converted signal generated by the FBG and the MZDI are shown in Fig. 4.29 and 30, respectively. In both cases the converted signal has clearly open eyes with ER larger than 11 dB.

Compared to the back-to-back case, the receiver power penalties due to wavelength conversion using FBG and MZDI are found to be 0.2 and 0.8 dB, respectively.

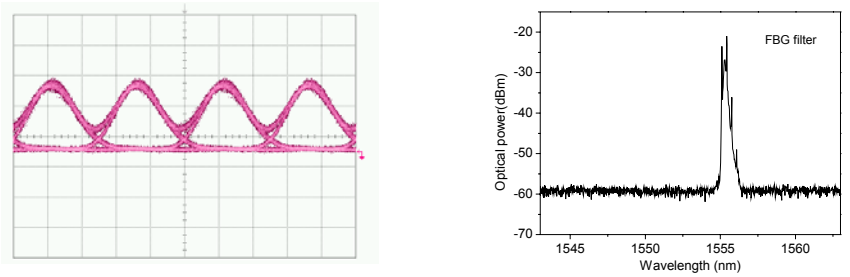

Fig. 4.29. (a) Eye diagram at 40 Gb/s and (b) spectrum at output of FBG.

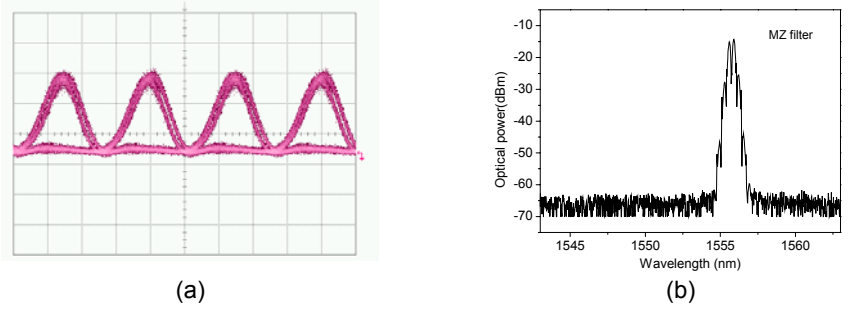

Fig. 4.30. (a) Eye diagram at 40 Gb/s and (b) spectrum at output of MZDI.

Kerr switch

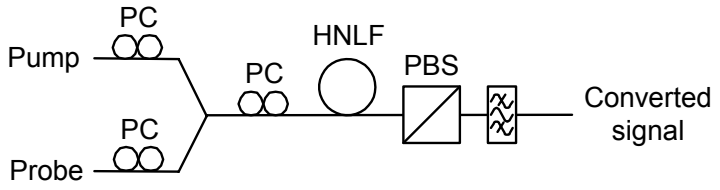

Fig. 4.31. Wavelength conversion at 40 Gb/s using a Kerr switch.

Fig. 4.31 shows the set-up for wavelength conversion using a Kerr switch, where PBS stands for polarization beam splitter. In the absence of the pump, there is no output at the cw probe wavelength because the polarization of the probe after transmission along the HNLF is adjusted to

be vertical to the port of the PBS used. In the presence of the pump XPM-induced polarization rotation allows part of the probe to pass through the PBS and data information on the pump is therefore copied onto the probe. The waveform and spectrum of the converted signal are shown in Fig. 4.32. Compared to the back-to-back case, the receiver power penalty due to wavelength conversion using the Kerr switch is about 2.1 dB.

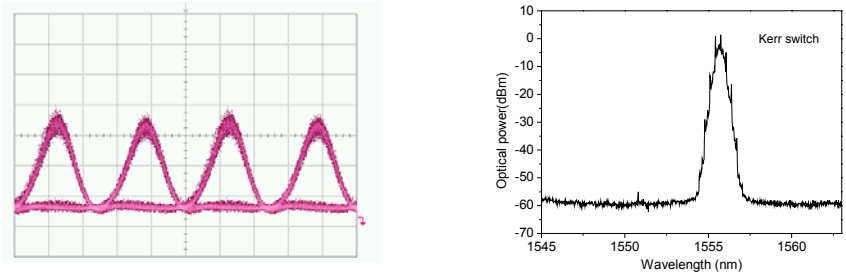

Fig. 4.32. (a) Eye diagram at 40 Gb/s and (b) spectrum of the converted signal by a Kerr switch.

Four wave mixing

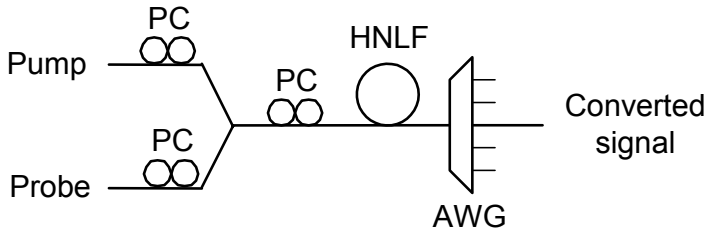

Fig. 4.33. Wavelength conversion at 40 Gb/s using FWM.

The set-up of FWM-based wavelength conversion is depicted in Fig. 4.33, where AWG strands for arrayed waveguide grating. As shown in Fig. 4.28 (c), new frequency components are generated through FWM at both sides of the pump-probe pair. By filtering out one of the FWM components, wavelength conversion is realized. The eye diagram of the converted signal is shown in Fig. 4.34. Compared to the back-to-back case the receiver power penalty due to wavelength conversion using FWM is about 1.6 dB.

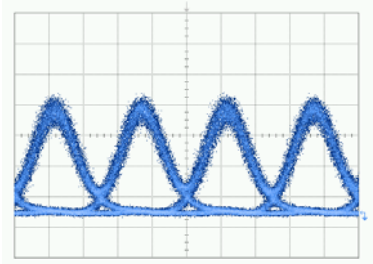

Fig. 4.34. Eye diagram of the converted signal at 40 Gb/s using FWM.

SOA-XGM

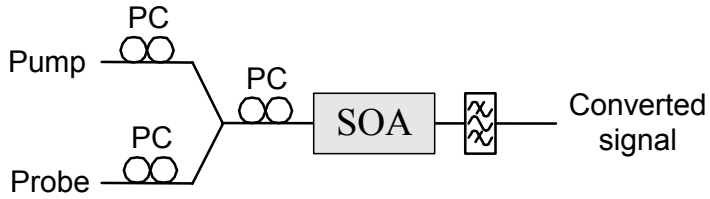

Fig. 4.35. Wavelength conversion at 40 Gb/s based on SOA-XGM.

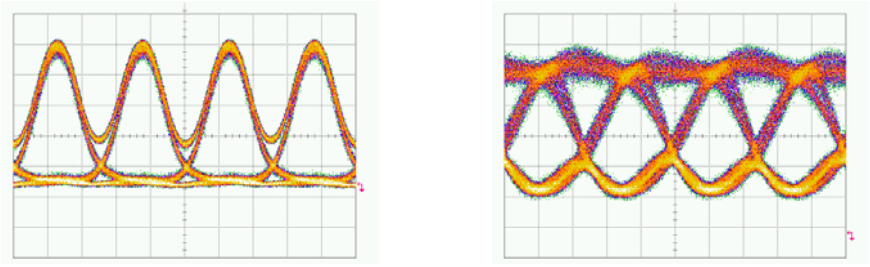

Fig. 4.36. Eye diagrams at 40 Gb/s of (a) the original and (b) converted signals.

Fig. 4.35 shows the set-up for SOA-XGM based wavelength conversion. The principle of this scheme is much like that of EAM. The pump signal modulates the gain of the SOA by depleting carriers and the inverted data information is duplicated onto the probe mediated by gain variation. The SOA used, developed under the SCOOP program, is 1400 μm long and is driven by a current of 750 mA.

The eye diagrams of the original and the converted signals are shown in Fig. 4.36. Compared to the back-to-back case, the receiver power penalty due to wavelength conversion using XAM is about 5 dB.

Comparison

As discussed above fibre-based schemes have in general less power penalty than semiconductor solutions. However, since the non-linear medium used here is the HNLF, the system is very sensitive to environmental disturbances, such as temperature and vibration. Due to the walk-off between pump and probe stemming from fibre chromatic dispersion, the wavelength tuning range is quite limited in order to match the group velocities of the two wavelengths involved. On the other hand, walk-off can be reduced by use of short HNLF, which unfortunately also reduces the interaction length and thus degrades the conversion efficiency.

SOA and EAM based solutions have comparable power penalty and both have advantages like environmental stability and compactness. Large insertion loss and high power requirement are issues to be addressed for the SOA and EAM.

One striking advantage of the EAM is the small wavelength conversion chirp as discussed in chapter 3 where the measured chirp α-parameters are from 0.2 to –0.6 depending on the operating bias and the probe wavelength.

The SOA-XGM scheme displays larger chirp compared to the EAM scheme mainly due to the larger carrier density modulation resulting from the high pump power and the large current injection, which are necessary to obtain the high extinction ratio and the high-speed operation. For instance, it was reported that the spectrum of the converted signal using SOA-XGM at 10 Gb/s was broadened to 13 GHz [159]. The broadened spectrum is related to the chirp α-parameter by [118],

$$\Delta\omega = \frac{(1+\alpha^2)^{1/2}}{T_0} \tag{4.19}$$

where $\Delta\omega$ is the spectrum width and in this case $\Delta\omega = 2\pi \times 13GHz$ and $T_0 = 100ps/1.665$ if the pulse width is assumed to be Gaussian, then the chirp α-parameter is about 4.8.

Fibre-based schemes rely on the XPM effect in the non-linear fibre as well as the conversion from the phase modulation to the intensity modulation, which leaves some residual phase information on the converted signal. Analytical results can be obtained by studying the non-linear phase due to XPM and the subsequent conversion.

As an example we investigate the residual phase modulation for the scheme based on XPM and optical filtering. For simplicity we consider a lossless and non-dispersive non-linear fibre and assume the original data signal and the cw light are both linearly polarized and collinear. In this case the non-linear propagation equations of the two fields involved are given as,

$$\frac{\partial A_1(z,t)}{\partial z} = i\gamma_1\left(\left|A_1(z,t)\right|^2 + 2\left|A_2(z,t)\right|^2\right)A_1(z,t) \tag{4.20}$$

$$\frac{\partial A_2(z,t)}{\partial z} = i\gamma_2\left(\left|A_2(z,t)\right|^2 + 2\left|A_1(z,t)\right|^2\right)A_2(z,t) \tag{4.21}$$

where A denotes the slowly varying envelope and γ the non-linear parameter [118], the suffixes 1 and 2 represent the cw light and the data signal, respectively.

Analytical solutions are easily obtained, i.e.,

$$A_1(L,t) = A_1(0,t)\exp(i\phi_1(t)) \tag{4.22}$$

$$\phi_1(t) = \gamma_1 L(P_1 + 2P_2(t)) \tag{4.23}$$

where $\phi_1(t)$ denotes the non-linear phase acquired by the cw light, L the fibre length, and P_1 and $P_2(t)$ the optical powers of the two signals considered.

The XPM modulated signal is then used as the input for the subsequent filters and is expressed as,

$$E_{in}(t) = A_1\exp(-i\omega_0 t)\exp(i\phi_1(t)) \tag{4.24}$$

where ω_0 is the carrier wavelength and A_1 the time invariant amplitude.

For the FBG filter it is more convenient to work in the frequency domain. The most useful part of the transfer function of this filter is the edge used for phase-amplitude conversion, which is known as slope detection [138] in the context of analogue FM system. We therefore only focus on the edge of the transfer function of the FBG as shown in Eq. (4.25), where k denotes the slope.

$$H(\omega) = 1 + k(\omega - \omega_0) \tag{4.25}$$

The output of the FBG is then $E_{out}(\omega) = E_{in}(\omega)H(\omega)$, which is transferred back to time domain and the final result is obtained with some manipulations,

$$E_{out}(t) = A_1 \exp(-i\omega_0 t)\exp(i\phi_1(t)) \cdot [1 - 2k\gamma_1 L \frac{dP_2(t)}{dt}] \tag{4.26}$$

The term in the square bracket of Eq. (4.26) is the resultant amplitude modulation. However, it is clearly that the signal after filtering retains a term of the time-varying phase ($\exp(i\phi_1(t))$), which is source of the frequency chirp for this wavelength conversion scheme.

In case of the MZI filter, we choose to work in the time domain and then the output signal is readily found, i.e.,

$$E_{out}(t) = E_{in}(t) + E_{in}(t+T) \tag{4.27}$$

where T is the extra time delay of one arm compared to the other of the MZI. By substituting Eq. (4.24) into Eq. (4.27), we obtain,

$$\begin{aligned} E_{out}(t) = {} & 2A_1 \exp(-i\omega_0 t)\exp(i\varphi_1(t))\exp(i\varphi_2(t)) \\ & \cos\{\frac{\omega_0 T}{2} + \gamma_1 L[P_2(t) - P_2(t+T)]\} \end{aligned} \tag{4.28}$$

where

$$\varphi_1(t) = \frac{2\gamma_1 L P_1 - \omega_0 T}{2} \tag{4.29}$$

and

$$\varphi_2(t) = \gamma_1 L[P_2(t) - P_2(t+T)] \tag{4.30}$$

The cosine term in Eq. (4.28) reflects the amplitude modulation and the residual phase information is shown in Eq. (4.30). The values of the chirp α-parameter in the two cases discussed above depend on

experimental details and careful investigations are required for chirp measurements. However, considering the fact that the intensity variation of the converted signal originates from the phase modulation, the large frequency chirp of the converted signal is expected.

4.4 Summary

In this chapter we first discussed the principle of EAM-XAM based wavelength conversion and studied the evolution of the converted signal in an EAM. A wavelength conversion experiment at 10 Gb/s was presented where the power penalty due to conversion was about 3 dB.

Next we demonstrated wavelength conversion at 40 Gb/s. The influence of some operation parameters, including pump light power, reverse bias of the converter and probe light wavelength, is experimentally investigated for the wavelength-converted light, including its chirp performance. As a result of this investigation, a higher pump power (up to 20 dBm) and a relatively larger reverse bias (-2.5 V) are preferred for obtaining both larger extinction ratio and lower chirp of the converted signal. As to the probe wavelength, which is so far optional within the whole C-band, conversion to shorter wavelength relative to the pump shows lower frequency chirp.

We have also demonstrated an EAM-based multiple wavelength conversion scheme where eight WDM channels are data-encoded simultaneously by an OTDM RZ signal (1545 nm) at 40 Gb/s through XAM. The receiver sensitivity for the back-to-back case is –33 dBm and the average power penalty for the eight converted channels is 9.2 dB. The best channel at 1555.7 nm has a power penalty of 8 dB. We explained the wavelength dependence of the power penalty by studying the impact of the extinction ratio and the average power of the converted signal on the Q parameter.

In another similar system configuration, where the original data signal is a 40 Gb/s base rate signal at 1555 nm, simultaneous 7 × 40 Gb/s wavelength conversion in RZ format is realized. The receiver sensitivity for the back-to-back case is –27.3 dBm and the average receiver power penalty for the eight converted channels is 7.4 dB. The best channel at 1554.12 nm has a power penalty of 6 dB. These experimental results

suggest that an EAM can be used for broadcasting in future WDM networks.

Finally, through numerical simulation, we gave physical explanations for the optimum pump power and device length, considering impacts on the extinction ratio, average power and pulse width of the wavelength-converted signal. We also briefly discussed some other wavelength conversion schemes such as fibre-based XPM and optical filtering, fibre-based Kerr switch, fibre-based FWM and SOA-based XGM. As a result of the comparison, it is suggested that fibre-based solutions have relatively lower power penalties and have great potential for ultra-high speed operation while single semiconductor devices can so far operate at 40 Gb/s and are more attractive in terms of compactness, stability and integration. An important advantage of the EAM-based wavelength conversion scheme is that the frequency chirp of the converted signal is very small, which is desirable for long distance transmission and optical labelling systems, as will be discussed in chapter 6.

5

All-optical demultiplexing

The channel rates in wavelength division multiplexing (WDM) transmission systems are steadily increased in order to cope with the expected increasing need for capacity in telecommunication systems. Channel rates of more than 40 Gb/s require optical time division multiplexing (OTDM) techniques, because 40 Gb/s is the highest bit rate for electrical signal processing, at present. OTDM uses bit-interleaving of signals at a base rate (e.g. 10 Gb/s) to form a higher bit rate data stream (e.g. 160 Gb/s) at a single wavelength. Fast optical switches are one of the key components in such OTDM systems. They are needed as demultiplexers to select one tributary channel (signal at the base rate) out of the bit-interleaved data stream for the optoelectronic receiver.

As discussed in Chapter 1, fibre-based demultiplexers, either configured as a nonlinear optical loop mirror (NOLM) [2,26,27] or using cross phase modulation (XPM) and optical filtering [28,29], have shown ultra-high speed operation up to 1.28 Tb/s [2], but have disadvantages with respect to compactness, environmental stability and integration. For these reasons, semiconductor devices may be preferred and thus have attracted intense attention. A number of SOA-based solutions have been demonstrated, which either rely on four-wave-mixing [30,31] or use various interferometers such as the symmetric Mach-Zehnder interferometer [32-34] or the gain transparent ultrafast nonlinear interferometer [35]. The EAM has also been extensively studied for high-speed demultiplexing and indeed several impressive high-speed demonstrations have been published, such as a photodiode integrated with an electroabsorption modulator (PD-EAM) at 320 Gb/s [73], and a travelling-wave EAM at 160 Gb/s [71]. However, [71,73] both require complex electronics like the travelling waveguide and [73] also requires advanced integration of PD with EAM. Using only one EAM waveguide, demultiplexing of 160 Gb/s to 40 Gb/s has been demonstrated through e/o modulation [67,68] or o/o modulation in self-cascading configuration [76].

In this chapter, we will discuss all-optical demultiplexing of an OTDM data signal from bit rates of up to 160 Gb/s to 10 Gb/s using cross absorption modulation (XAM) in a single EAM with a very simple waveguide structure [160]. In the first section we will introduce the fundamental principle of EAM-based all-optical demultiplexing using the o/o modulation model discussed previously, followed by experimental investigations at 80 and 160 Gb/s presented in section 2. Finally, the results will be summarised and discussed.

5.1 Principle of demultiplexing

The principle of EAM-based demultiplexing using XAM is schematically shown in Fig. 5.1.

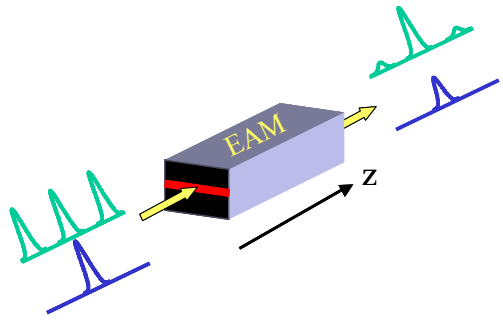

Fig. 5.1. Schematic of EAM-based all-optical demultiplexing.

At the input of the EAM, the green pulses represent the OTDM data signal while the blue pulse represents an optical clock signal with a repetition rate given by the OTDM base rate. The channel of the OTDM data stream that overlaps in time with the clock pulse is to be demultiplexed. During propagation in the EAM, the clock pulses saturate the absorption of the EAM and open a transmission window for the target OTDM channel through XAM, letting the target channel pass through with all other channels being suppressed. As shown in Fig. 5.1, at the output of the EAM the control signal is attenuated due to absorption and coupling loss. The target channel has a much higher power level than other channels and is thus demultiplexed. An optical band pass filter can

be used to separate the two signals by blocking the control signal and letting the demultiplexed signal pass through.

Using the o/o modulation model introduced in Chapter 3, we can study the signal evolution inside an EAM. The control pulse (1540 nm) has a full width half maximum (FWHM) of 1.5 ps and a repetition rate of 10 GHz, with an initial ER of 15 dB and an average power of 18 dBm. The 160 Gb/s OTDM data signal has a central wavelength of 1550 nm and an average power of 10 dBm. The evolution of the normalized demultiplexed signal along the EAM is shown in Fig. 5.2 as a function of time and z-coordinate along the waveguide. The vertical axis is the optical power normalized such that the peak power of the demultiplexed pulse is fixed at unity.

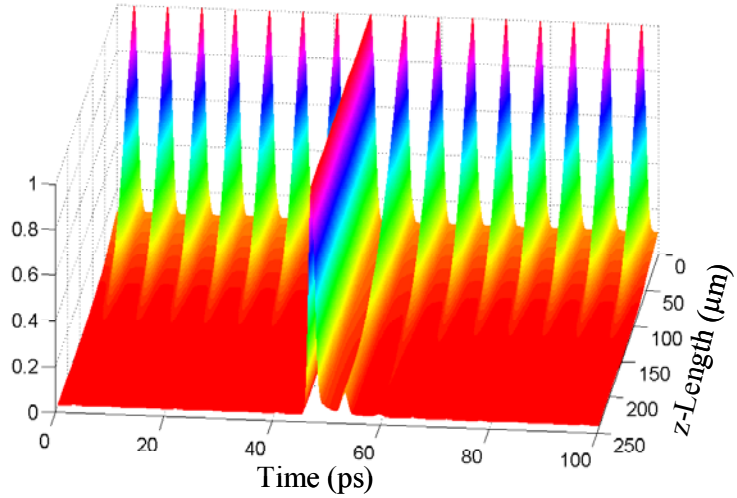

Fig. 5.2. Evolution of the demultiplexed signal along the device. The peak power of the demultiplexed signal is normalised to one.

As seen from Fig. 5.2, demultiplexing of the target channel is achieved gradually during propagation. At the input of the EAM, all the 16 channels have the same amplitude. During propagation, the target channel that is synchronised to the control clock signal experiences less absorption than others and thus has a relatively higher power level. At a device length long enough, e.g., longer than 150 μm, all the channels, except the one immediately following the target channel, are sufficiently suppressed. The reason that we see a small "pursuing neighbour" is due to the slow recovery time (~ps in the present example) of the photon-

generated carriers, which leaves the switching window slightly open for the subsequent pulse.

5.2 Experimental investigation

In this section we present our experimental investigations of all-optical demultiplexing using XAM in a single EAM with a simple waveguide structure.

5.2.1 Demultiplexing from 80 to 10 Gb/s

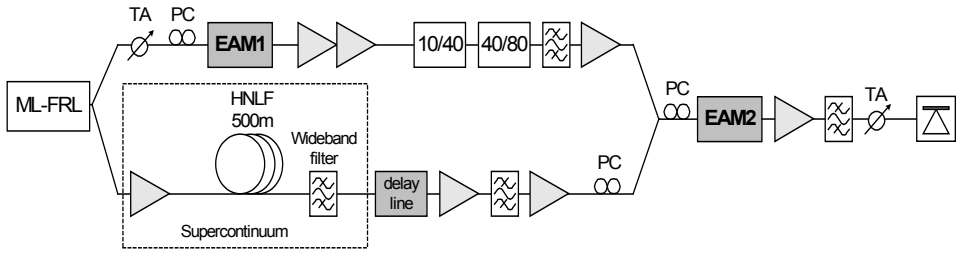

Fig. 5.3. Set-up for demultiplexing at 80 Gb/s. ML-FRL: Mode-locked fibre ring laser, TA: Tunable attenuation, PC: Polarization control, HNLF: Highly nonlinear fibre.

80 Gb/s signal generation

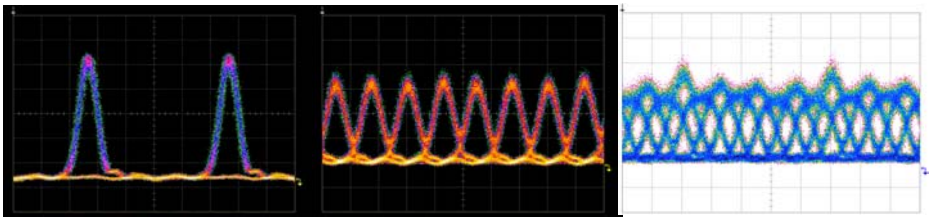

(a) (b) (c)

Fig. 5.4. Original eye diagrams at (a) 10 Gb/s, (b) 40 Gb/s and (c) 80 Gb/s.

The schematic set-up is shown in Fig. 5.3. A mode-locked fibre ring laser (ML-FRL), operating at 1548 nm, generates a short optical pulse

train at 10 GHz with a pulse width of ~ 3.59 ps, which is divided into two channels. The upper channel is intensity modulated by EAM1 and then optically multiplexed to 80 Gb/s by fibre-based interleaving. The eye diagrams at 10, 40 and 80 Gb/s are shown in Fig. 5.4.

Optical clock generation by super-continuum

Fibre-based super-continuum is used to shift the optical clock signal to a different wavelength. As seen in Fig. 5.3, the original clock signal at 1548 nm is amplified and launched into a 500 m highly nonlinear fibre (HNLF). At the output of the HNLF, the spectrum of the clock signal considerably broadens due to nonlinear effects in the fibre such as SPM and FWM. A new clock signal at a different wavelength is then obtained by using an optical band pass filter to chop the broadened spectrum.

This mechanism is shown in Fig. 5.5, where the broadened spectrum resulting from the super-continuum and the transmission window of the optical band pass filter (bandwidth 1.6 nm) are shown. The wavelength converted clock signal has a pulse width of 4 ps, a sample of which is shown as an inset in Fig. 5.5.

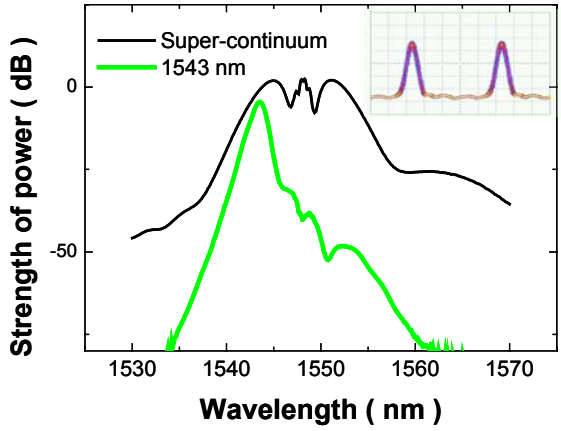

Fig. 5.5. Spectra of the output of the HNLF (black) and the generated clock signal (green), the inset shows the oscilloscope trances of the new optical clock.

In order to optimise the wavelength-converted clock signal, two optical band pass filters of different bandwidths are investigated. The pulse width of the converted signal is measured by an auto-correlator as

shown in Fig. 5.6, where the auto-correlation trace of the original pulse is depicted for reference. The original pulse has a pulse width of 3.59 ps, which is narrow enough to generate an 80 Gb/s signal (one bit time is 12.5 ps) by optical multiplexing. A 40 GHz Fabry-Pérot (FP) filter (~ 0.3 nm) is first tested and the resulting pulse width is about 6 ps. Based on the consideration that the pulse width is inversely proportional to the spectrum width, a filter with a wider bandwidth (1.6 nm) is tested in order to obtain a narrower pulse. As a result a pulse width of 4 ps is obtained. The waveform of the optical clock generated by the 1.6 nm filter is shown in the inset of Fig. 5.5.

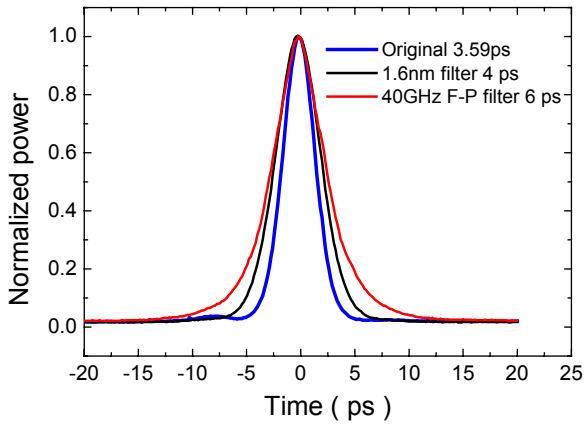

Fig. 5.6. Auto-correlation traces of the original pulse (blue) and the super-continuum wavelength-converted pulses obtained using two different filters (black and red).

Demultiplexing results

The data signal at 80 Gb/s and the control clock signal at 10 GHz are inserted into EAM2 through a 3 dB coupler. At the output of EAM2 the clock signal is suppressed by an optical band pass filter.

One example of the demultiplexed signal is shown in Fig. 5.7 (a). Error free operation is obtained at –21.7 dBm with EAM2 biased at –1.4 V. All the channels are found to be error free with an average receiver sensitivity of –21.5 dBm, as shown in Fig. 5.7 (b).

As seen from Fig. 5.7 (a), the zero level is quite “broad”, leading to a moderate extinction ratio. To further improve the receiver sensitivity, a

dispersion imbalanced loop mirror (DILM) is utilised to suppress variations of the zero level of the demultiplexed signal.

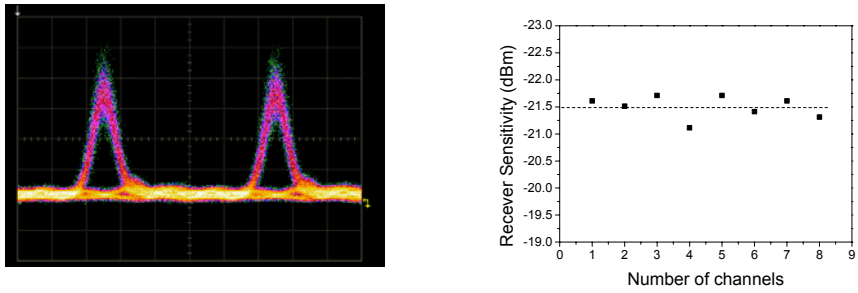

(a) (b)

Fig. 5.7. (a) An example of the eye diagrams at 10 Gb/s of the signal demultiplexed from an 80 Gb/s data stream, and (b) the receiver sensitivities for all channels.

Regeneration by a DILM

The DILM is basically an asymmetric nonlinear optical loop mirror (NOLM) that acts similarly to a saturable absorber in the sense that it can be used to suppress the ASE noise and pulse-to-pulse interactions. The working principle, though, relies on interference and not absorption, as will be discussed below. A number of applications using DILMs have been demonstrated such as pulse compression [161,162], cross talk suppression in an OTDM system [163], in-band ASE noise suppression [164], self-switching [165] and pedestal suppression in XGM wavelength converters [166].

A DILM consists of a 50/50 coupler and a fibre loop made of one segment of high anomalous dispersion single mode fibre (SMF), and another segment of dispersion-shifted fibre (DSF) or highly nonlinear DSF (HNLF) with a much lower dispersion. The unique switching property of the DILM is that only pulses are switched out, whereas a cw signal of arbitrary intensity is totally reflected because dispersion only affects pulses [167,168]. When the data signals enter the DILM, only the mark bits have sufficient power to open the switching window whereas the space bits do not, so the data signals are re-shaped by the DILM. As shown in Fig. 5.8, when the signal light enters the DILM through one port of the 50/50 coupler, the incident light is split into two parts before it

propagates in the fibre loop in two different directions. The clockwise-propagating pulse enters the SMF first and disperses quickly and its peak power decreases as the pulse width broadens. As a result, in the second fibre segment, the clockwise-propagating pulse gets less nonlinear phase shift than the counter-propagating beam. When the phase shift difference between these two beams equals π, the maximum transmission of the DILM occurs.

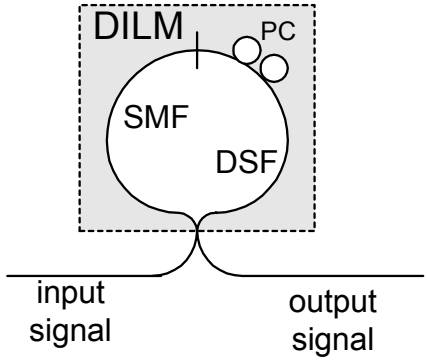

Fig. 5.8. Schematic of the DILM.

A Mach-Zehnder interferometer model has been proposed as an equivalent to the Sagnac loop mirror of the DILM [167]. By assuming that the states of polarization of the two beams are parallel and the phase shift difference between the two beams is $\Delta\phi(t)$, the transmission output of the DILM can be obtained,

$$\begin{aligned} P_{out}(t) &= \left|A_1(t)\exp(i\phi_1(t)) - A_2(t)\exp(i\phi_2(t))\right|^2 \\ &= A_1^2(t) + A_2^2(t) - 2A_1(t)A_2(t)\cos[\Delta\phi(t)] \end{aligned} \tag{5.1}$$

where $A_{1/2}$ and $\phi_{1/2}$ are the slowly varying envelopes and the instantaneous phases of the electric fields propagating in the two fibre arms; the subscript *"1"* relates to propagation in first the SMF and then the HNLF, and subscript *"2"* vice versa. The propagation of the fields in the fibre is governed by the coupled nonlinear Schrödinger equations [118],

$$\frac{\partial A_i}{\partial z} + \frac{1}{V_{g,s}}\frac{\partial A_i}{\partial t} + i\frac{\beta_{2,s}}{2}\frac{\partial^2 A_i}{\partial t^2} + \frac{\beta_{3,s}}{6}\frac{\partial^3 A_i}{\partial t^3} = i\gamma_s\left|A_i\right|^2 A_i \tag{5.2}$$

$$\frac{\partial A_i}{\partial z}+\frac{1}{V_{g,h}}\frac{\partial A_i}{\partial t}+i\frac{\beta_{2,h}}{2}\frac{\partial^2 A_i}{\partial t^2}+\frac{\beta_{3,h}}{6}\frac{\partial^3 A_i}{\partial t^3}=i\gamma_h\left|A_i\right|^2 A_i \tag{5.3}$$

where β_2 is the dispersion parameter, β_3 is the 3rd-order dispersion, A_i (i=1,2) denote amplitudes of the electric fields in the two arms, the index s stands for SMF and h for HNLF, γ is the nonlinear coefficient defined as $2\pi n_2/\lambda A_{\text{eff}}$, n_2 is the nonlinear refractive index of the fibre, and A_{eff} is the effective core area, and finally V_{g} is the group velocity. By solving Eqs. (5.1)-(5.3) the intensity transfer function of the DILM can be obtained as shown in Fig. 5.9 [167], which shows a strong nonlinearity that is desirable for 2R regeneration. It is also noted that above an optimum power level, corresponding to maximum transmission, the output shows an oscillating structure as suggested by Eq. (5.1), meaning that a careful control of the signal power is required to avoid the pulse splitting that may result from the oscillations.

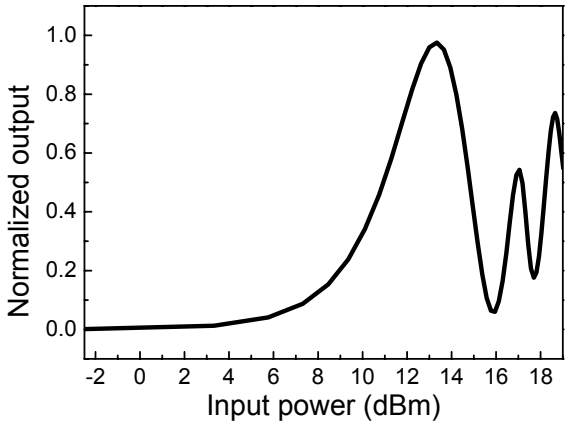

Fig. 5.9. Intensity transfer function of the DILM [167].

The DILM used in our experiment consists of a 3 dB coupler, a 1030 m long SMF and a 1 km long DSF. Fig. 5.10 (a) shows the eye diagram of the signal regenerated by the DILM and (b) shows the measured BER curves without (black) and with (red) 2R regeneration. It is clearly seen that the zero level is suppressed compared to the case without the DILM.

This signal regeneration leads to an improvement of the average receiver sensitivity of 3 dB (from –21.5 dBm to –24.5 dBm).

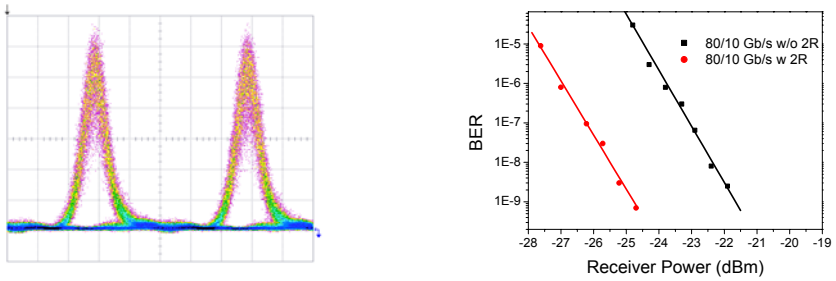

(a) (b)

Fig. 5.10. (a) Eye diagrams at 10 Gb/s of the demultiplexed signal from an 80 Gb/s data stream after the DILM and (b) the measured BER curves.

This experiment confirms that EAMs of a simple waveguide structure can be used for high speed demultiplexing up to 80 Gb/s. In addition, the quite low bias (-1.4 V) in our experiment suggests that there is room to narrow the switching window by increasing the bias without introducing too much power penalty, therefore demultiplexing at even higher bit rate is possible.

5.2.2 Demultiplexing from 160 to 10 Gb/s

Experimental procedures

The experimental set-up is shown in Fig. 5.11 [160]. A pulse-generating laser (ERGO PGL - a passively mode-locked laser using an Erbium doped glass as the gain medium and a fast semiconductor saturable absorber mirror to obtain pulsed operation at 10 GHz) operates at 1545 nm, and provides pulses with a pulse width of 1.4 ps. These are intensity modulated by a Mach-Zehnder modulator forming a data signal at 10 Gb/s. The data signal is amplified to a power level of 4.5 dBm and passed through a 3 nm optical band pass filter before being optically multiplexed to 160 Gb/s. The output of the multiplexer is amplified to a power level of 16 dBm by an in-line amplifier followed by a 3.5 nm optical band pass filter.

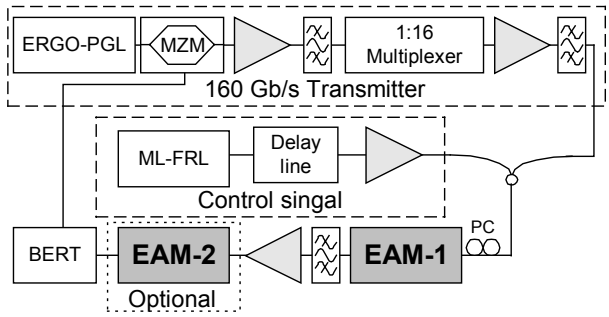

Fig. 5.11. Set-up for demultiplexing from 160 to 10 Gb/s. ERGO-PGL: Erbium Glass Oscillator Pulse Generating Laser, MZM: Mach-Zehnder Modulator, ML-FRL: Mode-Locked Fibre Ring Laser, BERT: BER testset.

A mode-locked fibre ring laser (ML-FRL) operating at 1558 nm, generates optical pulses at a repetition rate of 10 GHz with a pulse width of 2.4 ps, which are used as control pulses to obtain switching through XAM in EAM-1. Following an optical delay line used for channel selection, an optical amplifier boosts the control signal to an average power level of 19.7 dBm. The data and control signals are then combined by a 3 dB coupler and launched into EAM-1 biased at –2.8 V. The average power levels of the data and control signals at the input of EAM-1 are 9.3 dBm and 16.3 dBm, respectively. Since EAM-1 is polarisation dependent, a polarisation controller is employed for polarisation optimisation. At the output of EAM-1, a 1.5 nm optical band pass filter is utilised to suppress the control signal. The demultiplexed signal is then detected and the BER is measured.

Experimental results

The optical switching characteristics of EAM-1 are first measured using the control signal as pump and cw light at 1545 nm as probe. The autocorrelation trace of the modulated probe signal is shown in Fig. 5.12. The trace of the switching window (S.W.) yields an auto-correlated width of about 12 ps. The de-correlated real switching window is usually an asymmetric function with a steep rise and an exponentially decaying tail [74]. Fitting such a function to the measured data reveals a real switching window with a FWHM of about 7 ps, as shown in Fig 5.12. The steep rising edge of the fitted S.W. reflects the fast carrier density increase resulting from the absorption of the leading edge of the control pulse,

while the falling tail represents the relatively slow carrier recovery. Considering the tail one gets an effectively slightly wider window than the 160 Gb/s time slot. Trailing pulses will thus be switched through to some extent, but as will be shown, error-free demultiplexing can still be obtained.

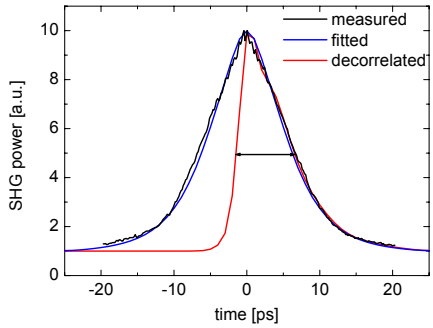

Fig. 5.12. Measured autocorrelation trace of the switching window (black) and the fitted (blue) and decorrelated (red) swithing windows.

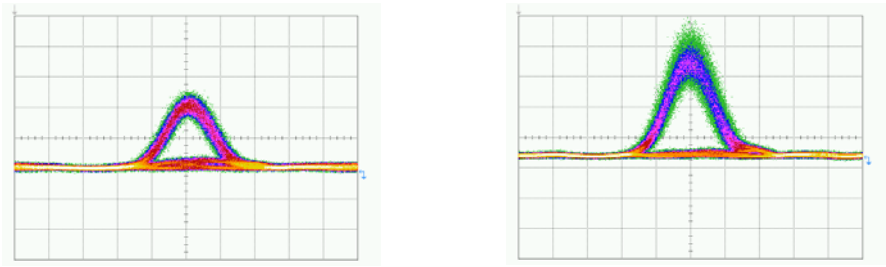

(a) (b)

Fig. 5.13. Eye diagrams at 10 Gb/s of the demultiplexed signal from an 160 Gb/s data stream (a) without and (b) with regeneration.

An example of the demultiplexed signal is shown in Fig. 5.13 (a). The eye is clear and open, and it is found that the signal is error free; the measured receiver sensitivity for this channel is –25.5 dBm. It may also be noted, however, that the extinction ratio is quite modest as indicated by the broad pedestal. This is due to the insufficient suppression of neighbouring OTDM channels stemming from the non-optimum switching window.

In order to improve the receiver sensitivity, EAM-2 is used to regenerate the demultiplexed signal through nonlinear absorption. As

discussed in chapter 3, high-intensity signals experience less absorption than low-intensity signals due to the absorption saturation effect in an EAM. This results in a nonlinear intensity transfer function, which can be used for pulse reshaping by increasing the extinction ratio and suppressing the space noise. The eye diagram of the regenerated signal is shown in Fig. 5.13 (b). It is evident that the noise on the zero bits is greatly suppressed, leading to an improved extinction ratio. It is also found, however, that the noise on the mark is enhanced. This is explained by the fact that the mark level probes a steeper slope of the intensity transfer function of the absorber, which actually may correspond to an enhancement of the intensity fluctuations of the input signal. Although the added noise on the mark slightly counteracts the benefit from zero level suppression, the receiver sensitivity improvement is still considerable as illustrated in Fig. 5.14, where the measured BER curves of the demultiplexed signal with and without regeneration are shown together with the performance of the original 10 Gb/s signal.

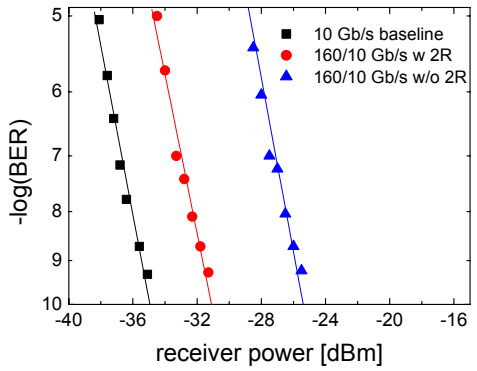

Fig. 5.14. Measured BER curves of the original 10 Gb/s signal (black) and the demultiplexed signal with (red) and without (blue) regeneration.

The receiver sensitivities of all channels without (solid circles) and with (solid squares) regeneration are shown in Fig. 5.15. Without regeneration the average sensitivity of the 16 channels is –25.3 dBm with a variation range of 0.7 dB. After regeneration by EAM-2 the average sensitivity is improved to –31.6 dBm with a variation range of 1 dB, i.e., more than 6 dB improvement. Compared to the back-to-back case (-35.4 dBm) the power penalty due to multiplexing and demultiplexing is 3.8 dB if regeneration is adopted.

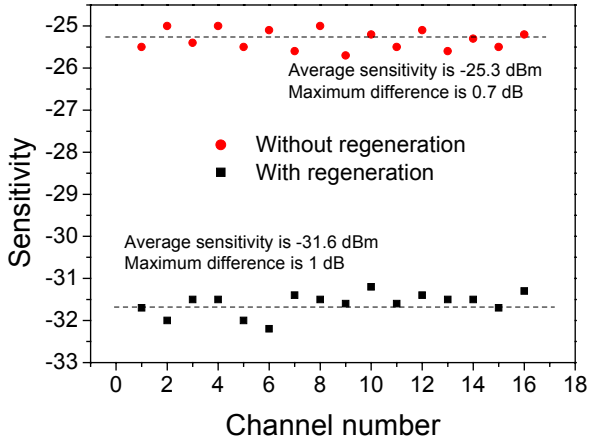

Fig. 5.15. Measured performance of all channels.

Compared to the previous case at 80 Gb/s, this demultiplexing subsystem is improved in several ways, which makes demultiplexing at 160 Gb/s possible. The EAM used here has a large static ER (28 dB/3V, previously 18 dB/3V), which results in an improvement of the ER of the switching window and thus a better suppression of the neighbouring channels. The insertion loss is reduced by about 8 dB through the use of a new type of tapered fibres, which reduces the stray light and leads to a higher power efficiency since more power of the control signal is launched into the EAM for absorption saturation. The quality of the control pulse and the system stability are improved by use of a separate short pulse source, while previously a fibre-based super-continuum wavelength conversion scheme was employed to generate the control pulse.

5.3 Discussion

5.3.1 Optimum operation

We have discussed our experimental results of all-optical demultiplexing using a single EAM. Now we use the o/o modulation

model to study the optimum operation for an EAM-XAM based demultiplexer. The major signal parameters used in our calculation are listed in Table 5.1. The primary device parameters have been given in Table 4.2.

	Control signal (Pump)	Data signal (Probe)
Wavelength (nm)	1540	1550
Repetition Rate	10 GHz	80 Gb/s
Initial ER (dB)	15	10
Pattern	Pulse train	PRBS
Pulse width (ps)	3	3

Table 5.1 Major parameters characterizing the input signals; data and control.

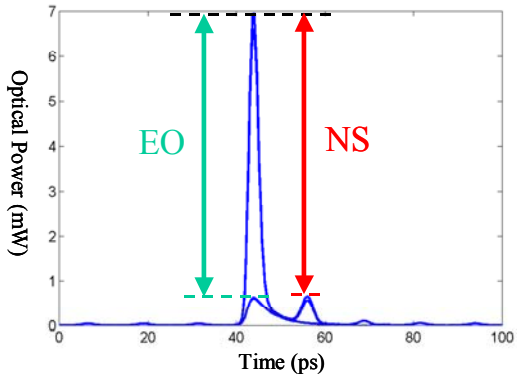

Fig. 5.16. Calculated eye diagram for the 10 Gb/s demultiplexed signal from an 80 Gb/s OTDM data stream.

The evaluation of the signal quality will mainly focus on two parameters, i.e., the eye opening of the selected channel (hereafter referred to as EO) and the suppression of neighbouring channels (hereafter referred to as NS). The definitions of these two parameters are illustrated in Fig. 5.16, where an example of the demultiplexed signal from an 80 Gb/s OTDM data stream is shown. As seen in Fig. 5.16, the EO is defined as the ratio of the minimum peak power of the marks to the maximum peak power of the spaces ($EO=10Log(Peak_{mark,min}/Peak_{space,max})$) and the NS is defined as the ratio of the minimum peak power of the marks to the maximum peak power of the neighbour channels ($NS=10log(Peak_{mark,min}/Peak_{neighour,max})$). The

extinction ratio of the demultiplexed signal is determined by the EO and the NS and therefore they should be optimized simultaneously.

The pump power dependence of the eye opening and the neighbour channel suppression is shown in Fig. 5.17. It is found that the EO of the demultiplexed signal generally increases with device length as a result of the nonlinear absorption experienced by the selected channel, meaning that the marks are less absorbed than the spaces. The improvement of the EO is less pronounced for higher pump powers, which can be understood by considering the bleaching effect discussed in Chapter 4. However, as seen from Fig. 5.17 (a), the variation of the EO is very small (less than 1 dB) and hence the pump power dependence of the EO can be neglected. In contrast, the NS shows a quite large dependence on the pump power as illustrated in Fig. 5.17 (b), where a picture similar to that of wavelength conversion is observed. An optimum pump power (18 dBm) for a device length of 150 μm is found, which generates a NS 4 dB larger than the values obtained for lower (15 dBm) or higher (22 dBm) pump power levels. The less efficient carrier density modulation under very high pump power is the cause for this dependence.

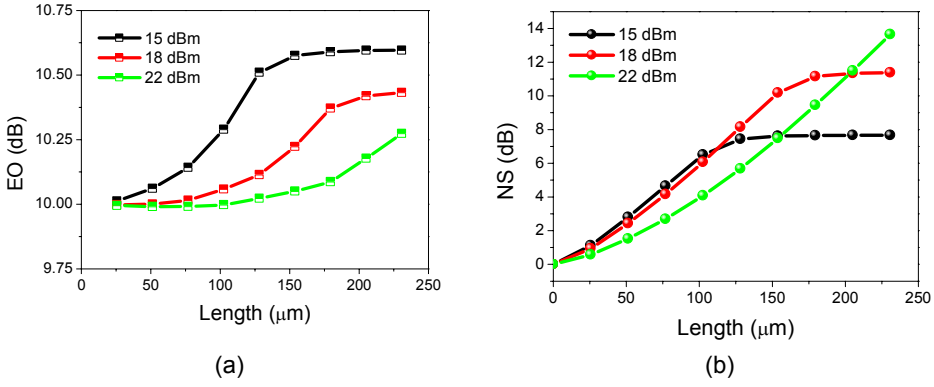

Fig. 5.17. Calculated (a) EO and (b) NS of the demultiplexed signal from an 80 Gb/s OTDM data stream versus device length for various pump powers.

Regarding the wavelength dependence of the efficiency of XAM based demultiplexing, the arguments for wavelength conversion also apply for demultiplexing since the transmission window opened by the absorption of the pump signal is the common mechanism used. In short, a pump signal at shorter wavelength is preferred because it has a larger absorption coefficient and can effectively modulate the carrier density.

However, a pump signal of longer wavelengths can achieve the same level of carrier density modulation if enough power is given and the ER is considerably high. The choice of the probe wavelength, the data signal in case of demultiplexing, depends on the trade-off between the extinction ratio and the output power, as discussed in chapter 4.

5.3.2 Regeneration using an EAM or a DILM

In the experiments discussed previously we have demonstrated the receiver sensitivity improvement of the demultiplexed signal by 2R regeneration using an EAM or a DILM. Here we qualitatively discuss the systematic indication of regeneration of this kind and compare these two schemes.

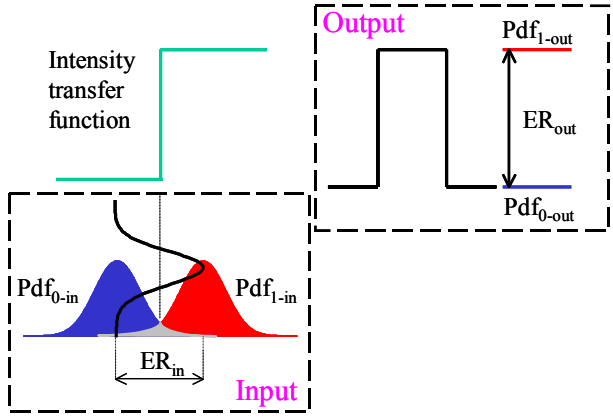

Fig. 5.18. Schematic of an ideal 2R regenerator.

For both schemes the mechanism used is the nonlinear intensity transfer function of the regenerator. To explain how regeneration works we draw upon an ideal 2R regenerator for NRZ signals, the instantaneous intensity transfer function of which is a stepwise function as shown in Fig. 5.18. The improvements of the signal are twofold. Firstly, the variance of the intensity fluctuations is decreased by the flat slopes at high and low intensities leading to narrow probability density functions (PDF). Secondly, the steep middle part may increase the extinction ratio depending on the height. Although the intensity transfer function of the EAM or NOLM based regenerator is far from being stepwise, these two

schemes can still realize regeneration function to a certain extent, as we have experimentally demonstrated.

However, one should note that the increase in the extinction ratio and the suppression of the noise do not imply an improved bit error ratio after the generator. As shown in Fig. 5.18, the regenerator imposes a threshold on the input signal and makes "decisions" based on this threshold. In other words, the regenerator works as an electrical error detector, however, in the optical domain. The overlapping area of the pdfs that corresponds to bit errors, as shown in Fig. 5.18, is thus implicitly transferred into the regenerated signal. To elucidate this, the BER of the input signal is expressed as

$$BER_{in} = E(\sigma_{in}) \tag{5.4}$$

where σ_{in} denotes the standard deviation of the noise and $E()$ the error integral. In arriving (5.4), we have assumed that marks and spaces have the same noise characteristics.

Assuming that the noise has Gaussian characteristics and based on a step-wise linear transfer function that has the same slope around mark and space levels and a discontinuity at the threshold [169], the BER of the regenerated signal is

$$BER_{out} = BER_{2R} + E(\sigma_{out}) \tag{5.5}$$

where BER_{2R} denotes the bit errors generated by the pulse reshaping and the second term accounts for the bit errors due to the redistributed noise.

For an ideal regenerator as shown in Fig. 5.18, BER_{2R} equals to BER_{in} because all the bit errors are transferred into the regenerated signal; σ_{out} is zero due to the zero pdfs after regeneration, then we obtain $BER_{out} = BER_{in}$. For a linear device which has a linear transfer function with an unity slope, BER_{2R} is zero since no reshaping is performed; σ_{out} equals σ_{in} because the output pdfs are the same as the input, then we also obtain $BER_{out} = BER_{in}$. Devices with a transfer function of an arbitrary nonlinearity fall in between the two cases considered above and the BER remains unchanged after a single regenerator [169].

Although the BER is not improved by use of a regenerator the signal is still conditioned in a way that decreases the rate of error accumulation in the rest part of the transmission. By approximating the nonlinear

intensity transfer function by a stepwise linear function and omitting the timing jitter, a simple expression for the BER after N regenerators can be derived [169],

$$BER_N \cong \frac{1}{\sqrt{2\pi Q_0^2 / F_N}} N \sqrt{\frac{1-\gamma^2}{1-\gamma^{2N}}} \exp(-\frac{1}{2}\frac{Q_0^2}{F_N}\frac{1-\gamma^2}{1-\gamma^{2N}}) \tag{5.6}$$

where γ is the nonlinearity parameter as introduced in [170] and F_N the noise figure of the linear amplifier forming part of regenerator and Q_0 is the input signal Q-value. Using Eq. (5.6), one finds that compared to linear devices, nonlinear devices have lower BERs for any value of N except for $N=1$ and the larger the nonlinearity is, the lower the BER becomes. When the regenerated signal is directly detected in a pre-amplified receiver it will be contaminated by various receiver noises, much the same way a signal is degraded along transmission. In this regard, a single regenerator can still improve the system performance as manifested by an enhancement of the receiver sensitivity as we have shown before.

The second point of the intensity transfer function is the frequency dependence. In the case of a DILM, the nonlinearity stems from the SPM effect in the fibre, which has a relaxation timescale of femtoseconds and therefore can be treated as an instantaneous process for most of applications of today. For an EAM, the nonlinear absorption results from absorption saturation and the response speed depends on the carrier recovery time. If the carrier density can not follow the change of the signal power, the EAM behaves like a linear component. The frequency dependence of the noise redistribution of NRZ signals by an EAM has been studied in [171], where it is found that the noise reshaping is more pronounced at low frequencies under small signal modulation.

Finally, the redistribution of the mark noise is different from that of the space noise when an EAM is used for regeneration. In [171], simulation results show that an EAM can actually enhance the mark noise at low frequencies due to the nonlinear intensity transfer function. This means that most of the improvement results from an increase in the extinction ratio and the variation suppression at the zero level, which is in agreement with our experimental results (see Fig. 5.13 and 5.14). In the case of the DILM, the intensity transfer function has a quite flat slope at low intensities and an oscillation structure at high intensities, as

previously shown in Fig. 5.9. The distribution thus faces the same problem as the EAM with respect to mark noise, if the input signal power is below the optimum value.

5.4 Summary

In this chapter we first discussed the principle of EAM-XAM based all optical demultiplexing and then presented our experiments of all-optical demultiplexing from an 80 Gb/s OTDM data stream to 10 Gb/s using a single EAM. All channels are found to be error free (BER < 10^{-9}) and an average receiver sensitivity of –21.5 dBm was obtained. By use of a DILM to regenerate the demultiplexed signal, the average receiver sensitivity is improved by 3 dB.

Next we experimentally demonstrated all-optical demultiplexing from a 160 Gb/s OTDM aggregated data signal to 10 Gb/s using a single EAM with a simple waveguide structure. All 16 demultiplexed OTDM tributary channels were error free with an average receiver sensitivity of –25.3 dBm. We furthermore demonstrated an improvement of up to 6 dB in the receiver sensitivity by regeneration of the demultiplexed channel by an additional EAM acting as a saturable absorber. This scheme is very promising due to the possibility of simple monolithic integration of two cascaded EAMs with a booster SOA in between.

We also discussed, from a system point of view, the main factors affecting the quality of the demultiplexing sub-system such as the choice of wavelength and the dependence on the pump power. An optimum pump power is found by evaluating the eye opening and the suppression of the neighbouring channels. Shorter wavelength for the control signal is generally preferred and the choice of the data signal wavelength depends on the trade-off between ER and insertion loss. A discussion about 2R regeneration based on a nonlinear intensity transfer function is given. It is reiterated that a 2R regenerator can not reduce the BER but can inhibit its accumulation. The nonlinear transfer function of an EAM is frequency dependent and the main improvement from an EAM-based regenerator is the enhancement of the ER and the suppression of the noise of spaces.

6

Optical labelling using EAMs

In previous chapters we have theoretically and experimentally studied several all-optical functionalities using cross absorption modulation and absorption saturation in an EAM, including wavelength conversion, demultiplexing and 2R regeneration. It has been shown that an EAM is able to serve as a versatile and key component for future all-optical networks. Now we want to discuss the applications of EAMs in optical label processing. As discussed before an EAM operating as a wavelength converter only responds to the intensity variation of the control signal disregarding any modulation/information on the phase. Furthermore, our e/o and o/o chirp measurements, presented in chapter 2 and 3 respectively, indicate that the e/o modulated or the wavelength converted signal by an EAM has very low chirp, meaning that the phase information of a cw light in either case may be preserved after being e/o or o/o modulated. This feature enables optical label encoding, erasure and swapping provided that the payload and the label are modulated on intensity and phase/frequency of an optical carrier respectively.

In the first two sections of this Chapter, an introduction to optical label swapping and orthogonal modulation is given. The following four sections are dedicated to our experimental investigations using EAMs for optical label processing based on various orthogonal modulation formats, including amplitude shift keying /differential phase shift keying (ASK/DPSK), amplitude shift keying /frequency shift keying (ASK/FSK), (NRZ/RZ)DPSK/ASK and base-band-coded-RZASK/DPSK. A summary is given in the last section.

It should be noted that some of the experiments described in this chapter were carried out in association with the EU IST project STOLAS .

6.1 Optical-label-switched network

The exponential growth of the broadband Internet traffic is pushing for larger and larger bandwidth. The measure that has been taken to overcome the ever-increasing bandwidth demand is a massive deployment of optical WDM systems. A recent report of a WDM transmission system with 273 channels operating at 40 Gb/s base rate has shown a system capacity of more than 10.9 Tb/s [1]. However, due to the bottleneck caused by optoelectronic conversion and processing at intermediate nodes, the throughput of the real networks is not as expected. Hence, all-optical networking is envisaged that is based on end-to-end lightpaths, enabled by optical cross-connects, switches and routers. For instance, an optical packet layer was proposed [140] to facilitate optical networking, which is a logical function layer between the electrical switched layer, such as synchronous digital hierarchy (SDH) or asynchronous transfer mode (ATM), and the optical transport layer. The introduction of a bit rate and transfer mode transparent optical packet switched layer can bridge the granularity gap between the high speed wavelength channels in the optical WDM transport network and the electrically switched network partitions. This improves the bandwidth utilization and the flexibility of the network by allowing switching of frequently changing high bit rate connections with diverse traffic characteristics without affecting the backbone cross-connects. Moreover, this optical packet switched layer can support and transport any data format without prior addition of framing and control bits, thereby offering a potential cost competitive solution.

Another simplified optical packet switching architecture as proposed in [172] is based on IP-over-WDM, which carries IP packets directly over WDM channels avoiding SDH or ATM as the intermediate layers, and thus leads to more efficient data transport networks. Direct IP-over-WDM transport is supported by the MPλS protocol [173], in which wavelength-switched channels are provisioned similar to MPLS label-switched paths. Fine switch granularity can be achieved by introducing a second-level optical label next to labelling with wavelengths, thus forming a two-level optical labelling network [42].

A two-level optical-label-switched network is schematically illustrated in Fig. 6.1 (taken from [42] with minor changes). Coming from the access or metro network, IP packets enter the core network at an ingress router and travel multiple hops through the core, exiting at an egress router. At an ingress router, IP packets are encapsulated with an optical label without modifying the original packet structure. A new wavelength is

assigned to the payload and label by wavelength conversion by looking up local routing tables. The new wavelength may be different from the original one and serves as a first-level label. The two-level-labelled packet is then ready to be forwarded to the next node.

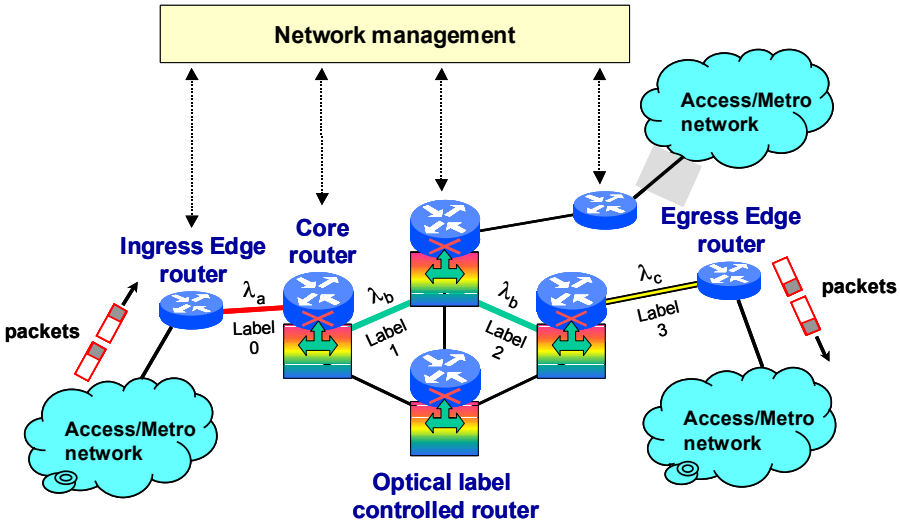

Fig. 6.1. Schematic of optical-label-switched network.

Once inside the core network, core routers perform routing and forwarding functions. The routing function computes a new label and wavelength from an internal routing table given the current label, current wavelength and fibre port. The routing tables are generated by converting IP addresses into smaller pairs of labels and wavelengths and distributing them across the network much in the same way that multi-protocol label switching is used in today's IP networks [174]. The forwarding function involves swapping the original label with the new label and physically converting the labelled packet to the new wavelength. Other switching or buffering mechanisms (space, time, etc.) are also configured in the forwarding process. When reaching an egress router the IP packet is deprived of the optical label and forwarded to its destination.

This two-level labelling scheme has various advantages. Reduction of SDH or ATM can significantly reduce system costs and simplify network managements. The second-level label ensures fine switch granularity. Due to the relatively low bit rate and compatibility with current electronic circuits low costs of provisioning the optical label are expected. The

second-level label can also be designed to be independent of the IP payload, thus ensuring transparency to payload bit rate as well as the seamless upgrading.

6.2 Orthogonal Modulation

The method of coding the label onto a packet impacts the channel bandwidth efficiency, the transmission quality of the packet and label, and the best method to wavelength convert the packet and optically swap the label. Two approaches that have been extensively studied are the serial label [36,37] and the optical sub-carrier multiplexed label [38-41]. With serial coding a fixed bit rate label is multiplexed at the head of the IP packet with the two separated by an optical guard-band (OGB). The OGB is used to facilitate label removal and reinsertion without static packet buffering and to accommodate finite switching times of optical switching and wavelength conversion. The bit-serial label is encoded on the same wavelength as the IP packet and is encoded as a base band signal. For optical sub-carrier multiplexed labels a base band signal is modulated onto an RF sub-carrier and then multiplexed with the IP packet on the same wavelength. An OGB is not necessary in the sub-carrier case since the label is transmitted in parallel with the packet [172].

Packet transparency is realized by setting a fixed label bit rate and modulation format independent of the packet bit rate. The choice of label bit rate is driven by a combination of factors including the speed of the burst-mode label recovery electronics and the duration of the label relative to the shortest packet at the fastest packet bit rates. Additionally, running the label at a lower bit rate allows the use of lower cost electronics to process the label. The label and packet can be encoded using different data formats to facilitate data and clock recovery [172].

Encapsulation of IP packets using optical labels has advantages in that the contents of the original IP packets are not modified and the label is coded at the same wavelength as the IP packet. In the serial case, erasure and rewriting of the label may be performed independently of the IP packet bit rate, however, timing of the label replacement and possibly erasure process is somewhat time critical. The sub-carrier labels have the advantage that they can be removed and replaced more asynchronously

with respect to the packet but potentially suffer from dispersion induced fading [172].

Within the framework of the EU IST project Stolas a new optical label coding method is proposed, i.e., Orthogonal Modulation [42,43]. In contrast to the two techniques discussed above orthogonal modulation generates an optically labelled signal by putting the label information on the optical carrier wave in a modulation format that is orthogonal to that of the payload. The concept of orthogonal modulation is schematically shown in Fig. 6.2. For instance, the label information is either DPSK modulated on the phase or FSK modulated on the frequency of the optical carrier while the payload is ASK modulated on the amplitude. Here "orthogonal" means that the demodulation of the payload and label can be achieved independently of each other.

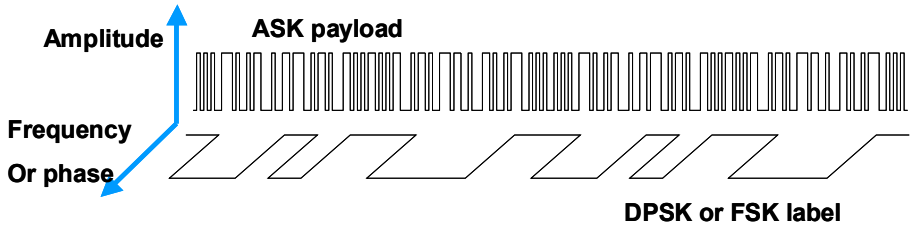

Fig. 6.2. Orthogonal modulation.

Orthogonal ASK/DPSK [175-179] and ASK/FSK [180-185] optical labelling schemes have been proposed as a competitor to the sub-carrier multiplexed optical labelling due to compact spectrum, simple label swapping and remarkable scalability to high bit rates. These two labelling techniques have better spectral efficiency compared to the sub-carrier multiplexing methods, leading to good resilience to fibre chromatic dispersion. Additionally, the labelling processing can be kept intact when upgrading the payload speed in contrast to the traditional sub-carrier multiplexing method where it is necessary to change the RF frequency if the payload bit rate is increased. Compared to the ASK/FSK scheme ASK/DPSK has more compact spectrum, however, the detection of low bit rate DPSK labels imposes very stringent requirement on the line-width of lasers and the stability of fibre-based demodulators.

Alternatively, the DPSK/ASK [186,187] optical labelling can be achieved with a combination of a DPSK modulated payload and an ASK modulated label. Due to the fact that the relatively lower bit rate label

(typically up to a few Gbit/s for compatibility with electronic label processing) is renewed at each node, the modulation depth only needs to be large enough to ensure the label transmission for just one hop. This small modulation depth can further extend the multi-hop transmission of the DPSK payload, which leads to DPSK/ASK labelling having a larger tolerance to the modulation depth than ASK/DPSK labelling.

In the following sections we will present our experimental investigations on various orthogonal labelling schemes using EAMs for label processing. In case of ASK/DPSK and ASK/FSK labelling systems label erasure and reinsertion can be achieved through EAM-based wavelength conversion. For DPSK/ASK labelling systems two EAMs are used for label encoding and erasure, with one modulated by the electrical label signal in the normal way and the other one inversely.

6.3 Label encoding based on ASK/DPSK format

In this section we present our experimental investigations on EAM-based optical label encoding based on a 10 Gb/s ASK payload and a 2.5 Gb/s DPSK label, in connection with which the chirp property of the wavelength converted signal is discussed.

The experiments were carried out together with my colleagues N. Chi, J. Zhang, P. V. Holm-Nielsen, B. Carlsson, C. Peucheret, P. Jeppesen (Stolas members at Research Center COM, DTU) and the results are published in [175-179].

6.3.1 Experimental set-up and results

Set-up

The experimental set-up is shown in Fig. 6.3 [175]. A CW light beam generated by tuneable laser #1 (TL1) working at 1550 nm is intensity-modulated by a MZI modulator with a PRBS pattern length of 2^9-1 forming a Non-Return-to-Zero (NRZ) signal at 10 Gb/s that serves as the pump, hereafter referred to as an ASK signal. Wavelength conversion is performed through cross absorption modulation induced by the pump beam on a probe signal. The probe beam is generated by tuneable laser #2

(TL2) working at 1555 nm and is phase-modulated at 2.5 Gb/s with a PRBS pattern length of 2^7-1, hereafter referred to as a DPSK signal. Parasitic phase modulation in the EAM, due to refractive index changes induced by the ASK-pump signal, will thus affect the quality of the DPSK signal. The optical power of the pump and probe beams are 20 dBm and 10 dBm, respectively. The reverse bias of the EAM is -2.4 V.

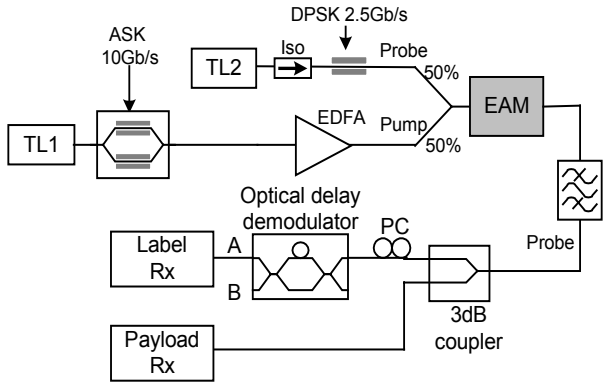

Fig. 6.3. Experimental set-up for label encoding using an EAM for a 10 Gb/s ASK payload and a 2.5 Gb/s DPSK label.

After wavelength conversion the probe beam is filtered out through an optical band pass filter with a bandwidth of 1.6 nm. In the case of conversion to the same wavelength, counter-propagation of the pump and probe can be used to separate the original and the converted signals. Using a 3 dB coupler, the converted signal is divided into two arms, one for intensity detection and the other for phase detection. The phase detector is a fibre-based delay interferometer (DI), which converts the DPSK modulation as well as the frequency chirp into intensity variation. One arm of the interferometer is 8 cm longer than the other, corresponding to an extra time delay of 400 ps. The transmission loss difference between the two arms is very small (~ 0.17 dB), therefore no loss imbalance effect is observed on the DPSK detection.

Experimental results

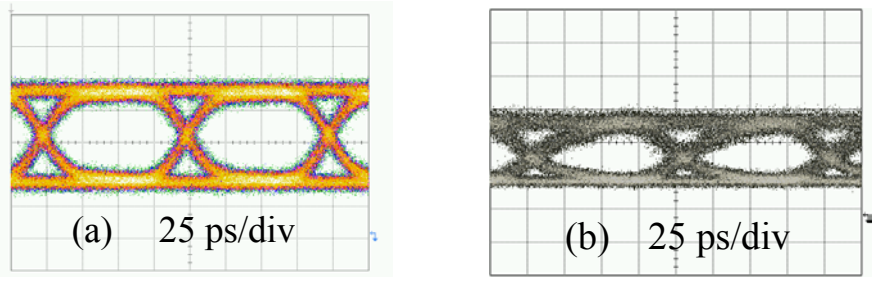

Fig. 6.4. Eye diagrams of the ASK payload at 10Gbit/s of (a) the original signal and (b) the converted signal.

Fig. 6.4 depicts the ASK eye diagrams of the original signal and the converted signal, clearly showing that the ASK information is successfully duplicated onto the probe beam. Since both mark bits and space bits of the wavelength converted signal carry phase information, the power level of space bits shouldn't be too low to facilitate detection of the phase variation. Therefore a relatively low extinction ratio (ER) of the converted signal is required. Theoretically, an ER up to 9.5 dB is allowed for DPSK detection. In our experiment, however, we adjust the ER to be about 3.5 dB because the fibre-based DI is temperature and polarization sensitive and therefore difficult to optimise. Compared to a normal ASK signal with an ER of 10 dB, the power penalty due to low ER is measured to be ~6 dB. The ER of the ASK signal can be improved by using a high-stability DPSK detector and/or a balanced receiver.

The DPSK eye diagrams before and after wavelength conversion are shown in Fig. 6.5; open eyes of the converted signal are observed. As expected, however, the upper eyelids are broadened considerably while the lower eyelids get only slightly thicker. This can be attributed to the 256 different combinations of ASK bits in one DPSK bit-time of the two arms of the DI, as will be discussed in the following subsection.

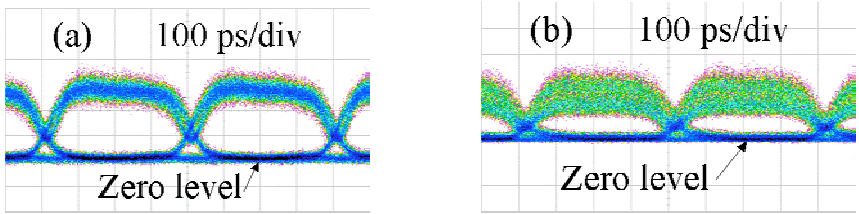

Fig. 6.5. Eye diagrams of the DPSK label at 2.5 Gb/s of (a) the original signal and (b) the converted signal.

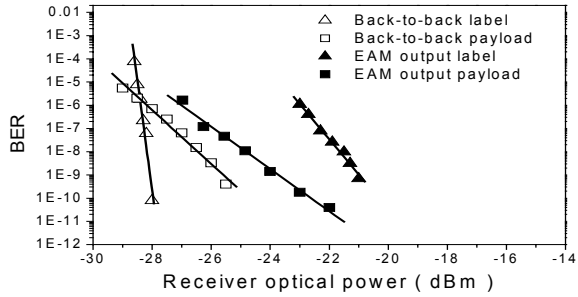

Fig. 6.6. BER of the payload at 10 Gb/s and the label at 2.5 Gb/s before and after wavelength conversion.

The measured BER curves are shown in Fig. 6.6. The receiver sensitivities for the payload/label in back-to-back case and after label encoding are –25.6/-28.1 dBm and –23.7/-21 dBm, respectively. The results confirm that the ASK and DPSK components of the converted signal can both have BERs as low as 10^{-9}, and optical label encoding/recognition is thus successfully realized.

6.3.2 Pulse chirp analysis

In the delay interferometer one arm provides an extra delay of 400 ps to the signal, i.e. one bit-time of the DPSK signal, before it is combined with the other arm at the output. The interference between the two arms is generally governed by equations (1)-(2), where E denotes the output electric field, P the compound optical power and ω the optical angular frequency. P_A and φ_1 are the optical power and the phase of one arm, P_B and φ_2 of the other arm. $\Delta\varphi_{dpsk}$ is the phase difference between the two arms induced by the original DPSK modulation and $\Delta\varphi_{chirp}$ is the phase difference caused by chirp originating from wavelength conversion (i.e. XAM in the EAM) [175].

$$E = P_A^{1/2} e^{j(\omega t+\varphi_1)} + P_B^{1/2} e^{j(\omega t+\varphi_2)} \tag{6.1}$$

$$P = |E|^2 = P_A + P_B + 2\sqrt{P_A P_B}\cos(\varphi_1 - \varphi_2) = P_A + P_B + 2\sqrt{P_A P_B}\cos(\Delta\varphi_{dpsk} + \Delta\varphi_{chirp}) \tag{6.2}$$

In one DPSK bit-time four ASK bits of one arm overlap with their counterpart in the other arm, resulting in a total of 256 combinations. This is understandable because each arm has 2^4 (=16) combinations of ASK

bits and a direct calculation leads to 16×16=256. However, some combinations have the same consequence, e.g., (1100:0011) and (0011:1100) make no difference, this leads to a dividing factor of 2. Since the DPSK modulation results in a zero or π phase difference between the two arms, they may interfere constructively or destructively, resulting in a multiplicative factor of 2. These two factors counteract each other leading to a total number of 256.

If a photodiode with a bandwidth of 2.5 GHz is used for the detection of the DPSK label, power levels averaged within one DPSK bit-time will be shown due to the slow response, instead of the subtle ASK structure. The averaged power levels depend on the number of the mark bits involved in the interference of the two arms, but different combinations may have different consequences even with the same number of mark bits. For instance, considering the case of 4 mark bits under constructive interference, three different average power levels result from (1111:0000), (1110:1000) and (1100:1100) according to equation (2), while all other possibilities of combinations do not generate any new levels. This corresponds to the number of different unordered possibilities for filling *r* slots by *n* different elements. The solution for this problem is shown in equation (6.3):

$$A(n,r)={}_{n+r-1}C_r \tag{6.3}$$

In our case, *r* is the number of ASK bits in one DPSK bit-time and equals 4, *n* is the number of levels within one ASK bit-time. As will be shown in Table 6.1, *n* equals 3 for constructive interference and 2 for destructive interference. It is thus found that ${}_6C_2$ (=15) power levels result from constructive interference and ${}_5C_1$ (= 5) power levels from destructive interference.

For the purpose of chirp investigation, however, it is convenient to express the interference on the basis of a single ASK bit. The identification of the various signal levels and the corresponding power are given in Table 6.1. Here P_1 and P_0 denote the optical power of "1" bits and "0" bits of the ASK signal, respectively. The three higher levels form the upper eyelids and the two smaller levels form the lower eyelid. As seen in Table 6.1 only level 2 and level 4 are influenced by chirp-induced phase distortion.

ASK bits		Power	Level
Arm1	Arm2		
0 PSK phase shift between two arms			
1	1	P_1	One
1	0	$\frac{1}{4}P_1+\frac{1}{4}P_0+\frac{1}{2}\sqrt{P_1P_0}\cos\Delta\varphi_{chirp}$	Two
0	1	$\frac{1}{4}P_1+\frac{1}{4}P_0+\frac{1}{2}\sqrt{P_1P_0}\cos\Delta\varphi_{chirp}$	Two
0	0	P_0	Three
π PSK phase shift between two arms			
1	1	0	Five
1	0	$\frac{1}{4}P_1+\frac{1}{4}P_0-\frac{1}{2}\sqrt{P_1P_0}\cos\Delta\varphi_{chirp}$	Four
0	1	$\frac{1}{4}P_1+\frac{1}{4}P_0-\frac{1}{2}\sqrt{P_1P_0}\cos\Delta\varphi_{chirp}$	Four
0	0	0	Five

Table 6.1. Power levels resulted from the DPSK detection.

The calculated internal structure of DPSK eyes under zero chirp is shown in Fig. 6.7 (left), where four ASK bit-times within one DPSK bit-time are depicted. The measured DPSK eye diagrams (right) are also given for a direct comparison. Here, the ER of the ASK signal is taken from experimental data recorded when the DPSK eyes were measured.

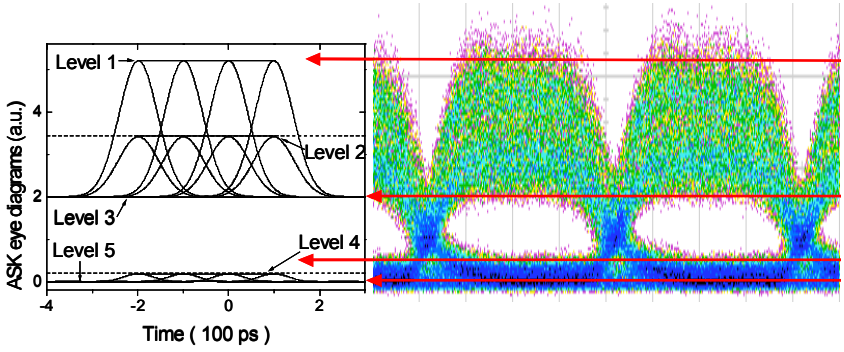

Fig. 6.7. Simulated DPSK internal structure under zero chirp (left) and experimental results (right).

As indicated in Table 6.1, five distinct power levels result due to the interference between the two arms of the DPSK demodulator. However, as seen in the right part of Fig. 6.7, level 2 of the measured DPSK eyes is not distinguished. This is well understood and happens because the DPSK and ASK signals are not synchronized in our set-up. Therefore, only level 4, as one of the chirp-sensitive levels, can be investigated for comparison purposes. A later discussion will reveal that, compared to level 2, the impact of level 4 on the DPSK eyes is more important due to its immediate contribution to the closure of the DPSK eyes. Fig. 6.7 also indicates certain disagreement in level 4 between the left and right parts, suggesting the existence of frequency chirp.

A: Constant chirp α-parameter

To gain a basic understanding of how the frequency chirp influences the DPSK demodulation we first employ the assumption of a constant value for the chirp α-parameter during an ASK pulse. The definition of chirp α-parameter has been given in section 2.3.2.

Since this definition, initially defined for electrical modulation of an EAM, expresses the frequency chirp in terms of optical pulse characteristics (intensity and phase), it can also be used for optical modulation occurring in an EAM, e.g. wavelength conversion.

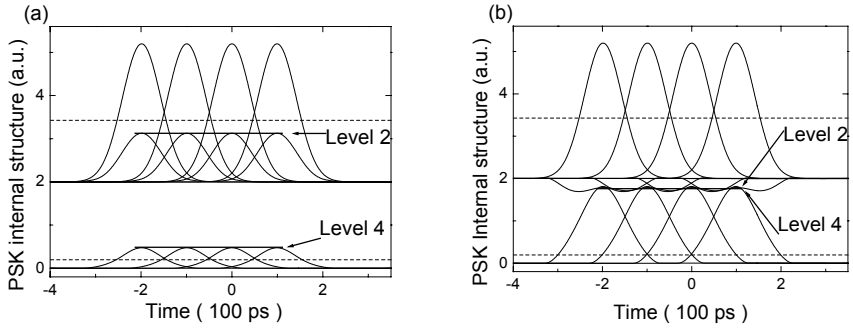

Fig. 6.8. The simulated DPSK internal structure for different values of the chirp-α parameter: (a) 0.26 and (b) 0.68. The upper and lower dashed lines indicate level 2 and level 4 in case of no chirp, respectively.

The simulation results under various constant chirp α values are shown in Fig. 6.8. It is found that in the presence of chirp, level 4

increases and level 2 decreases, corresponding to an "attraction" of the two chirp-sensitive levels. From this observation it becomes apparent that the change of level 4 is dominant in degrading the DPSK eyes, especially under small frequency chirp (Fig. 6.8 (a)) when level 2 has no contribution at all. From Fig. 6.6 we find that the DPSK eyes tend to close as the chirp α-parameter increases. If the absolute value of α reaches 0.68 the DPSK eyes become completely closed, as shown in (b). Then it becomes evident that chirp-induced phase distortion is naturally detrimental to DPSK demodulation and will ultimately make the DPSK signal levels indistinguishable; this also means the chirp must be reasonably small ($|\alpha| < 0.68$) if the DPSK eyes are to be clearly open.

B: Varying chirp α-parameter

Now we consider a more realistic case with the chirp α-parameter varying along the ASK pulses. Our earlier measurement of the chirp induced by optical-to-optical (o/o) modulation in an EAM, as repeatedly shown in Fig. 6.9, suggests a linear variation of the α-parameter for reverse voltages lower than 3 V. In this measurement we modified the fibre response method proposed by Devaux by inserting an EAM-based wavelength converter into the transmission line; then the chirp α-parameter of the converted signal can be measured with the same principle designed for electrical-to-optical modulation. More detail analysis can be found in Chapter 2.

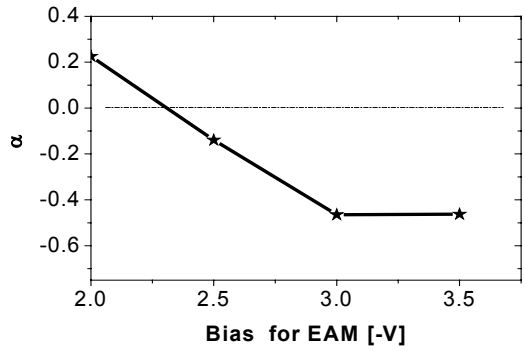

Fig. 6.9. Measured chirp α versus reverse bias for o/o modulation of EAM.

If we assume that the change of the effective field seen by the probe beam instantaneously follows the power change of the pump beam, due to the screening effect of pump-photon-generated carriers, then the small signal α will have a profile similar to the pump pulse. This is illustrated in Fig. 6.10, where the normalized pulse is given for reference.

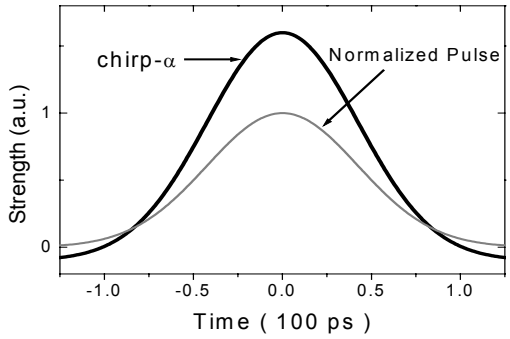

Fig. 6.10. Chirp α profile for ASK signal.

We set the start value of α corresponding to the highest electrical field, i.e. lowest pump power, to be –0.1. Then with the maximum chirp α as a variable parameter, we calculate the internal structure of the DPSK eye diagrams as shown in Fig. 6.11. It is found that a much wider dynamic range of chirp α is allowed than for the case of constant α parameter. Thus, as seen in Fig. 6.11 (b), the DPSK eyes completely close for a maximum α of 3.6, whereas in the case of constant α we obtained 0.68. In case of PRBS where successive "1"s or "0"s may occur with various pattern length, the chirp α-parameters have more complex profiles depending on the patterns. The leading and trailing edges of various patterns still follow the model presented in this sub-section while the flat top regions resulting from more than one mark bit acquire constant chirp α values. However, according to the definition of chirp-α the flat top regions have negligible contribution to the phase change ($\Delta\varphi_{\text{chirp}}$) due to the zero amplitude variation ($dP/dt = 0$). Therefore only the two edges of different patterns need to be considered, as addressed in the above discussion.

Our experimental results are compared to this varying chirp α-parameter model, which applies to an EAM. The fairly good agreement between Fig. 6.11 (a) and the measured DPSK eye diagrams (Fig. 6.7

right part) suggests an approximate range of chirp α from –0.1 to 1.6 for EAM-based wavelength conversion.

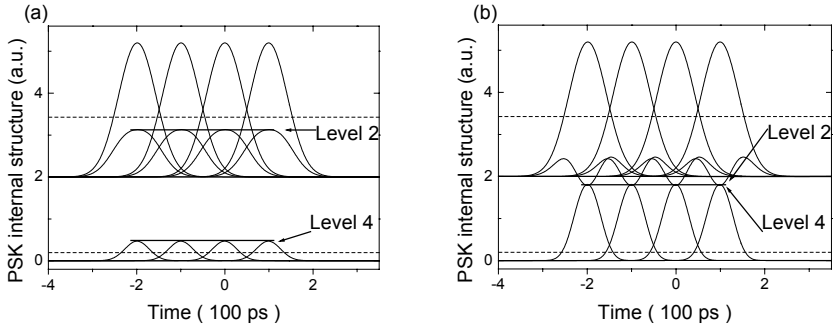

Fig. 6.11. The internal structure of DPSK eye diagrams, with maximum α of (a) 1.6, (b) 3.6. The upper and lower dashed lines indicate level 2 and level 4 in case of no chirp.

Based on the above discussion, we conclude that phase distortion induced by wavelength conversion may be very harmful to DPSK detection of the converted signal. For a constant value of α a restrictedly small value is required. However, in the case of using an EAM, where α varies dynamically along the wavelength-converted pulse, the requirements are relaxed and may be met by a carefully designed EAM.

6.4 Label processing based on ASK/FSK format

In this section we present our experimental investigations on optical label swapping and transmission properties of the labelled signal based on a 10 Gb/s ASK payload and a 312 Mb/s FSK label. Very similar the ASK/DPSK labelling scheme, EAM-based wavelength conversion is employed to transfer the ASK payload information to the FSK-labelled wavelength without distorting the original frequency information owing to its small o/o chirp. The back-to-back performance of the optical packet is presented in the first subsection, where a short description of the optical ASK/FSK transmitter and receiver is given. At the transmitter two EAMs are used for compensation of amplitude variation of the frequency modulator (a DFB laser) and for payload modulation, respectively. The

second subsection is dedicated to the EAM-based optical label insertion, followed by a study of FSK label swapping employing an MZ-SOA for label erasure and 2R regeneration and an EAM for label reinsertion, as will be presented in the third subsection. A complete functionality of a real network node with two-hop transmission and all-optical label swapping of an optically ASK/FSK labelled signal is demonstrated at last.

The experiments were carried out together with my colleagues N. Chi, J. Zhang, P. V. Holm-Nielsen, B. Carlsson, C. Peucheret, P. Jeppesen (Stolas members at Research Center COM, DTU) and the results are published in [180-185].

6.4.1 ASK/FSK back-to-back performance

The optical ASK/FSK transmitter and receiver are shown in Fig. 6.12 [185]. An optical FSK signal can be generated simply by directly modulating the electrical current of a DFB or DBR laser diode. However, the drive current variation also results in a simultaneous intensity modulation of the emitted light. As for the optical labelling, such residual intensity modulation has a detrimental effect on the optical packet when the payload information is added. To overcome this problem, the inverse electrical data is applied to the integrated EAM with appropriate time delay and modulation voltage. In this way, a constant amplitude optical FSK signal at 312 Mb/s (PRBS 2^7-1) is generated.

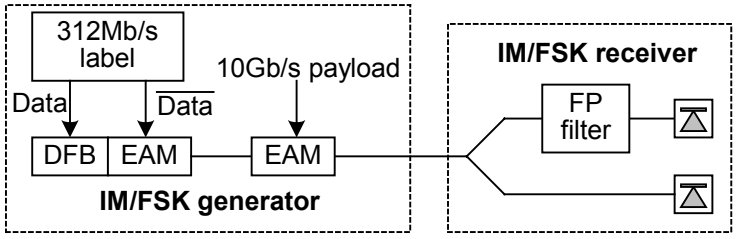

Fig. 6.12. Configuration of the optical ASK(10Gb/s)/FSK(312Mb/s) transmitter and receiver.

Fig. 6.13 shows the measured eye-diagrams and optical spectrum of the FSK modulated signal when the DFB laser was driven with a 90 mA bias current and a 30 mA peak-to-peak modulation current. Without

intensity compensation, nearly 3 dB intensity fluctuation was observed, as shown in Fig. 6.13(a). Both the bias and modulation voltage of the EAM were optimized to compensate for the residual intensity modulation. The final output light had almost constant amplitude, as shown in Fig. 6.13(b). A perfect FSK signal with a peak-to-peak frequency deviation of 20 GHz was finally generated, as indicated by the spectrum in Fig. 6.13(c).

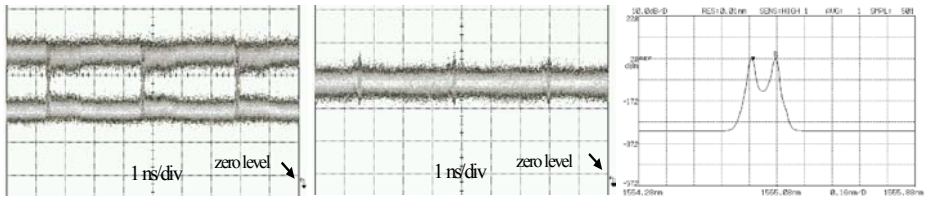

(a) (b) (c)

Fig. 6.13. (a) Direct output eye-diagram at 312 Mb/s of the DFB Laser, (b) output eye-diagram after EA compensation, (c) output spectrum after EA compensation.

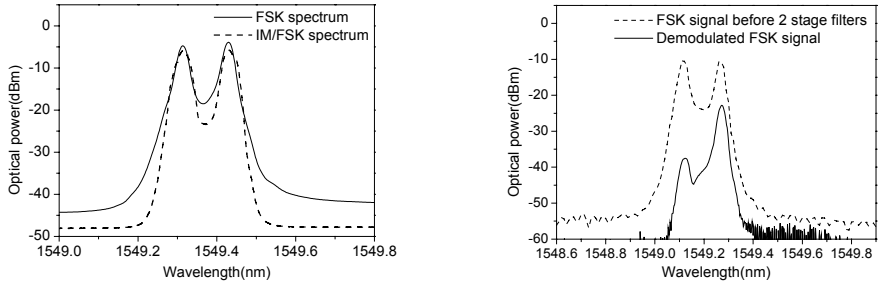

(a) (b)

Fig. 6.14. (a) Optical spectra of the pure FSK and the ASK(10Gb/s)/FSK(312Mb/s) signal, (b) optical spectra of the FSK signal and demodulated FSK signal.

The payload information at 10 Gbit/s (PRBS 2^9-1) is added by a following EAM, thus producing an optically ASK/FSK labeled signal. It should be noted that a limited ASK extinction ratio is necessary for the FSK label detection, but on the other hand this low extinction ratio will deteriorate the payload detection. Therefore, in our experiment, a compromise value of 4.5 dB is selected for the extinction ratio of the ASK payload.

At the receiver node, the labeled signal was split using a 3 dB optical coupler. The output of one arm was directly detected by a photodiode and thus the optical payload was converted into the electrical domain. In the other arm, a fibre-Bragg-grating (FBG) was used to filter only a single lobe of the FSK labelled signal, thus achieving FSK demodulation. The demodulated label was received by an electrical receiver with 1.8 GHz bandwidth. Fig. 6.14 shows the optical spectra of the ASK/FSK signal.

Fig. 6.15 shows the back-to-back eye-diagram of the payload and the label pattern. Clearly, some payload information is superimposed onto the label after the FSK demodulation, however the eye is still open and allows error-free detection. The receiver sensitivities for the back-to-back configuration of the FSK/ASK combined modulation format are -32.6 dBm and -24.2 dBm for the FSK label and ASK payload, respectively.

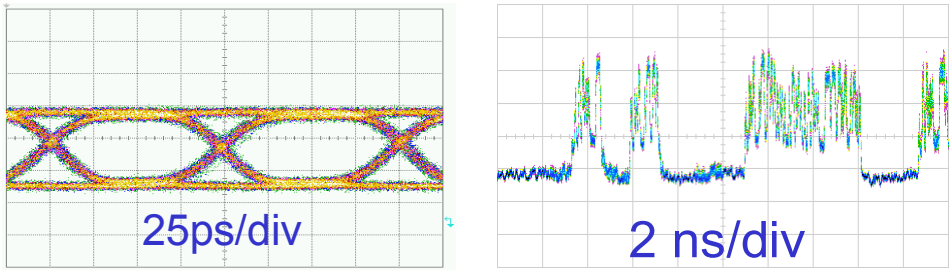

(a) (b)

Fig. 6.15. (a) Back-to-back payload at 10Gb/s, (b) back-to-back label pattern at 312 Mb/s.

6.4.2 Label insertion using an EAM

The experimental set-up for FSK label insertion based on cross-absorption modulation (XAM) in an EAM is shown in Fig. 6.16 [182]. A CW light beam generated by a tuneable laser operating at 1554.1 nm is intensity-modulated in a MZ modulator with a PRBS pattern length of 2^9-1, forming a Non-Return-to-Zero (NRZ) signal at 10 Gbit/s that serves as the pump. Wavelength conversion is performed through XAM induced by the pump beam on a probe FSK signal. The optical FSK modulation is achieved by directly modulating the electrical current of a DFB laser with the data of the label signal (bit rate of 312 Mbit/s, PRBS pattern length of

2^7-1) while feeding the inverted electrical data signal into the following EAM, as previously described. The optical power of the pump and probe beams are 23.5 dBm and 12.5 dBm, respectively. The reverse bias of the EAM is –1 V.

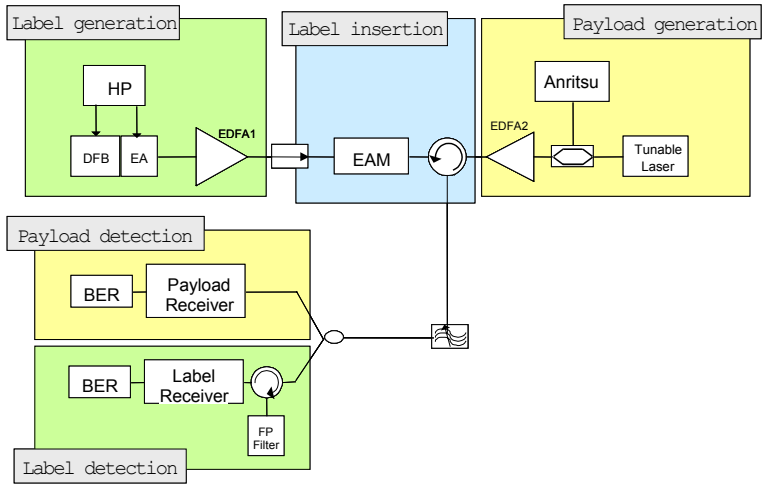

Fig. 6.16. Experimental set-up for FSK label insertion using an EAM.

After wavelength conversion, the probe beam is filtered out through an optical filter with a bandwidth of 1.6 nm. Counter-propagation of the pump and probe was used in our experiment. Using a 3 dB coupler, the converted signal is divided into two arms, one for intensity detection and the other for FSK detection. The frequency discrimination for FSK demodulation is achieved by 2 optical filter stages providing more than 15 dB suppression ratio between the two FSK tones.

Fig. 6.17 depicts the received eye diagrams of the payload and label, clearly showing that the ASK information is successfully duplicated onto the probe beam. Since both mark bits and space bits of the wavelength converted signal carry frequency modulated information, the power level of the space bits should not be too low to facilitate FSK detection. Therefore a relatively low extinction ratio (ER) of the converted signal is required. In this experiment, the input ER is adjusted to be about 4.5 dB. The ER at the output is then around 4 dB.

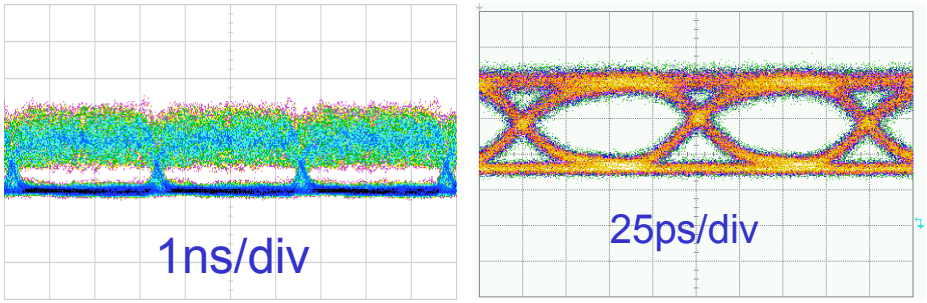

Fig. 6.17. Received eye diagrams of (a) label at 312 Mb/s and (b) payload at 10 Gb/s after label insertion.

6.4.3 Label swapping using an EAM and a MZ-SOA

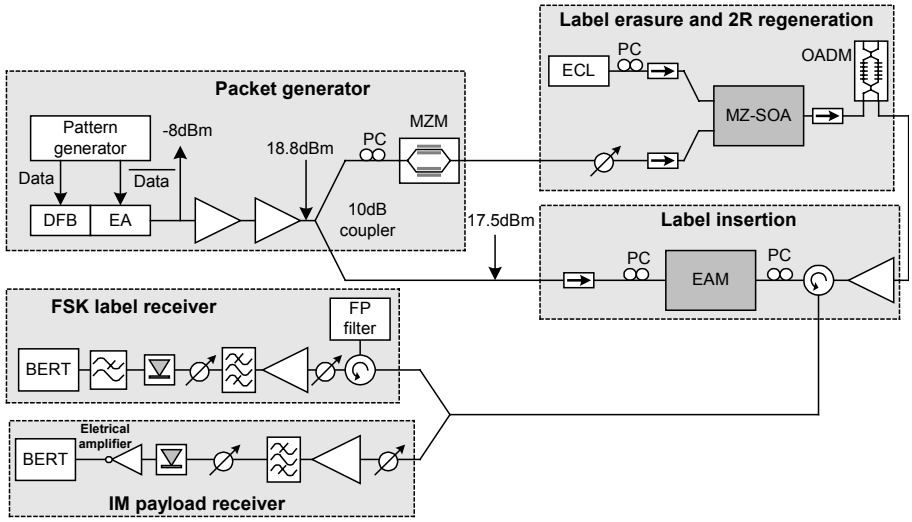

Fig. 6.18. Experimental set-up for cascaded FSK label erasure and insertion.

In a real network, the label of the signal will have to be renewed at every node. Firstly erasing the FSK label through wavelength conversion in a MZ-SOA that will preserve the ASK information and secondly impressing a new FSK label through a second wavelength conversion process in an EAM can achieve this [182]. Fig. 6.18 shows the set-up for this label swapping technique.

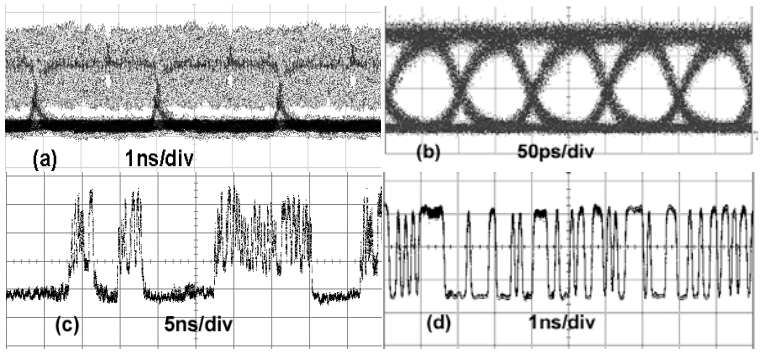

Fig. 6.19. (a) Received eye diagram of the FSK label at 312 Mb/s, (b) eye diagram of the ASK payload at 10 Gb/s, (c) received pattern of the label, (d) received pattern of the payload.

The eye-diagrams and pattern of the updated FSK label and ASK payload are shown in Fig. 6.19. The results of the BER measurements for the FSK and ASK signals after a complete label swapping stage are shown in Fig. 6.20. We can compare these results with the back-to-back measurements presented in subsection 7.4.1. We observe there is no substantial power penalty for both signals (below 0.5 dB).

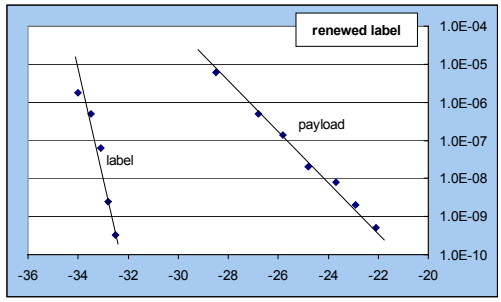

Fig. 6.20. BER versus input power for an ASK(10Gb/s)/FSK(312Mb/s) combined modulation scheme after a complete label swapping stage.

6.4.4 A network node demonstration

A node prototype of the all-optical switching network based on ASK/FSK labelling has also been demonstrated, consisting of two-hop transmission and all-optical FSK label swapping [180]. The experimental set-up is shown in Fig. 6.21. The FSK modulated label at 312 Mbit/s (2^7-1 PRBS) was generated using the previously described DFB/EA technique. The payload information at 10 Gbit/s (PRBS 2^9-1) was added by a following Mach-Zehnder modulator, thus producing an optically ASK/FSK labelled signal. In this experiment a compromise value of 4.3 dB is chosen for the extinction ratio of the ASK payload.

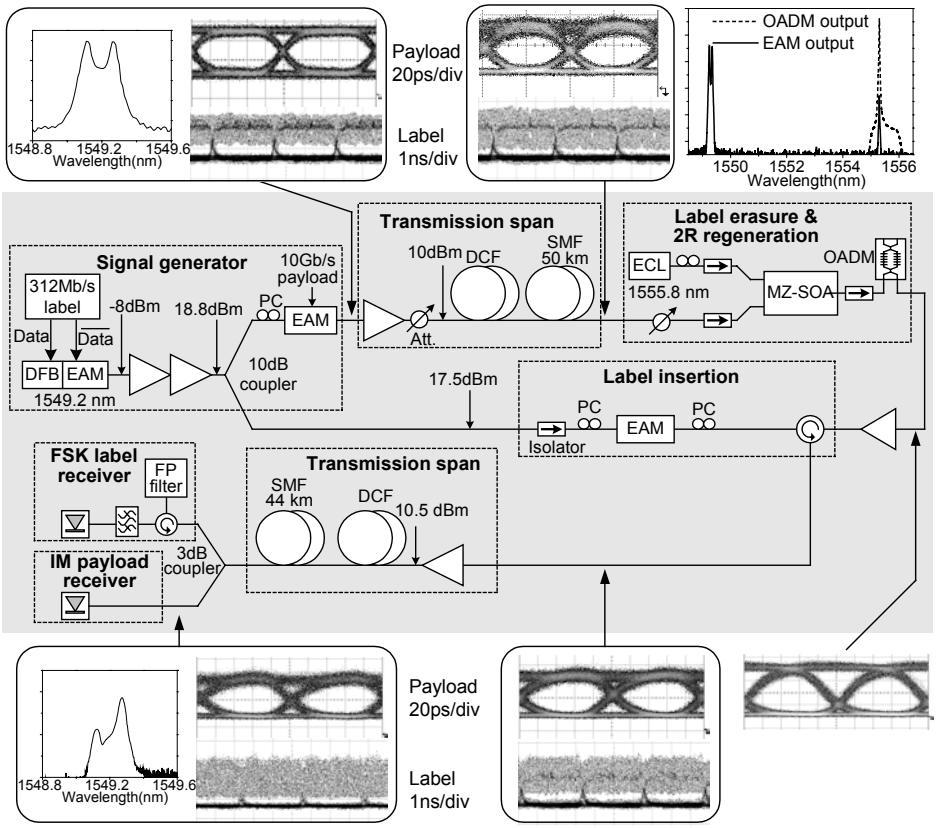

Fig. 6.21. Experimental set-up for two-hop transmission with label swapping.

The first hop consists of 50 km single mode fiber (SMF) with matching length of dispersion compensating fiber (DCF). The dispersion of the SMF and the DCF is 16.9 ps/nm/km and -100 ps/nm/km, respectively. The dispersion slope of the SMF is 0.0578 ps/nm2/km,

against -0.23 ps/nm2/km for the DCF. Simulation results and experimental investigation both reveal that a pre-compensation scheme has better performance than a post-compensation scheme. Hence pre-compensated fibre spans are chosen for both fibre links. After this first stage transmission the optically labelled signal is input to the MZ-SOA for the label erasure and 2R regeneration. Light from a tuneable external cavity laser at 1555.8 nm is used as CW input for the MZ-SOA. Very good label erasure and 2R regeneration can be achieved by the MZ-SOA. Due to its non-linear transfer characteristic, the extinction ratio of the converted signal is greatly improved to 12.9 dB, which leads to a 2 dB improvement of the receiver sensitivity. The regenerated payload is then fed to the EAM as the pump signal for the label insertion process, where the extinction ratio of the label-renewed signal will be adapted to the required value.

The advantage of using the EAM for label reinsertion is the negligible frequency chirp induced by EAM-based wavelength conversion, which is extremely desirable in our orthogonal ASK/FSK labelling scheme.

The initial FSK signal is split into two parts with one of them acting as the second label source for the label insertion module. The non-linear transfer characteristic of the MZ-SOA is beneficial for the output extinction ratio at the cost of some amplitude jitter and eye diagram distortion. It should be noted that the noise imposed onto the EAM output eye diagram (see Fig. 6.21) is due to the fluctuation of the FSK intensity. As mentioned earlier, a limited extinction ratio is obligatory in the orthogonal labelling scheme. This relatively low extinction ratio can be easily accomplished by adjusting the reverse bias of the EAM. The output signal of the label swapper has an extinction ratio of 4.9 dB. The second hop includes 44 km SMF and 6 km DCF. At the receiver, the frequency discrimination for FSK demodulation is achieved by 2 optical filter stages providing more than 15 dB of suppression ratio between the two FSK tones.

Fig. 6.22 shows the BER curves in the back-to-back case, after the first hop, after the label swapper and after the second hop. The inset figures show the patterns for both the payload and the label as detected after two-hop transmission including label swapping.

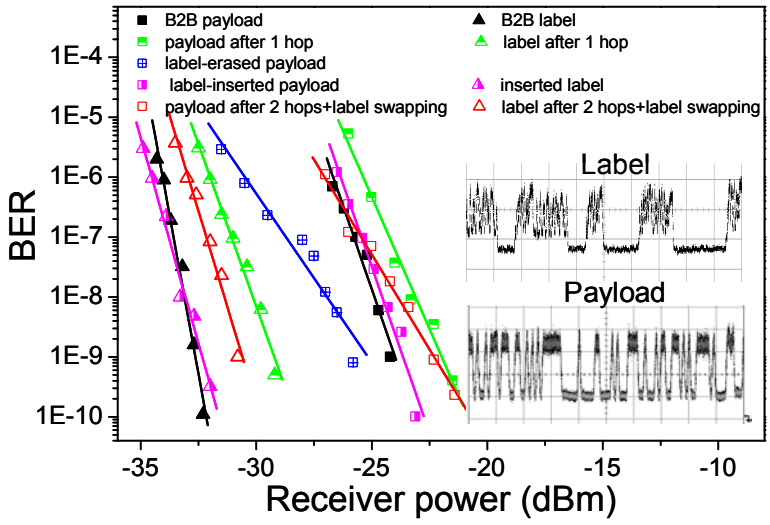

Fig. 6.22. Measured BER results for the payload at 10 Gb/s and label at 312 Mb/s. The inset figures show the received patterns of the payload and label after two-hop transmission and label swapping.

Clearly some payload information is superimposed onto the label after the FSK demodulation. However the eye is still open and allows error-free detection. Compared to the back-to-back case (-24. 2dBm sensitivity) the ASK payload shows 2 dB penalty due to the first hop transmission, 3 dB improvement by SOA-based wavelength conversion used for label erasure and regeneration, 1.4 dB penalty due to EAM-based label reinsertion and 1.5 dB penalty due to the second hop transmission, leading to an overall penalty of 1.9 dB. The FSK label, with a back-to-back sensitivity of –32.6 dBm, shows 3.4 dB penalty stemming from the first hop transmission, 3.1 dB improvement by SOA-EAM and 1.5 dB penalty due to the second hop transmission, generating an overall penalty of 1.8 dB. Hence, the cascaded transmission and label swapping result in 1.9 dB power penalty for the payload and 1.8 dB penalty for the label.

6.5 Label processing based on DPSK/ASK format

As discussed in section 6.2, orthogonal ASK/DPSK optical labelling has been proposed as a competing scheme to sub-carrier multiplexed optical labelling due to compact spectrum, simple label swapping and remarkable scalability to high bit-rates. However, using the DPSK modulation format for the relatively lower bit rate label (typically up to a few Gb/s for compatibility with electronic label processing) will result in a strict requirement on the laser line-width [43]. Moreover, the temperature and mechanical stabilization of the 1-bit delay Mach-Zehnder interferometer used for DPSK demodulation will become a challenge. On the other hand, high speed DPSK will relieve the laser line-width requirement and allow for building more stable integrated DPSK demodulators. Recent experiments [188,189] show that at 40 Gb/s the return-to-zero (RZ) DPSK modulation format is a promising technique to overcome non-linear impairments and to extend transmission distance. Therefore RZDPSK is an advantageous choice for the payload modulation format in next generation networks.

In the first part of this section we discuss a new orthogonal optical labelling scheme using an RZDPSK payload and a superimposed ASK label, namely orthogonal RZDPSK/ASK labelling. This scheme will take advantage of the robust non-linear tolerance during transmission and as already mentioned alleviate laser line-width requirements. An experimental investigation of label insertion, propagation over a 50 km dispersion compensated SMF transmission link and label erasure of an optically RZDPSK/ASK labelled signal consisting of a 40 Gb/s RZDPSK payload and a 2.5 Gb/s ASK label will be presented, which clearly validates this orthogonal RZDPSK/ASK labelling scheme as a potential solution for future high speed optical label switching. NRZDPSK/ASK labelling is also studied and experimental results are presented in the second subsection.

The experiments were carried out together with my colleagues N. Chi, J. Zhang, P. V. Holm-Nielsen, C. Peucheret, P. Jeppesen (Stolas members at Research Center COM DTU), C. Mikkelsen, H. Y. Ou (Glass competence area Research Center COM DTU) and the results are published in [186,187].

6.5.1 RZDPSK/ASK label processing

Set-up

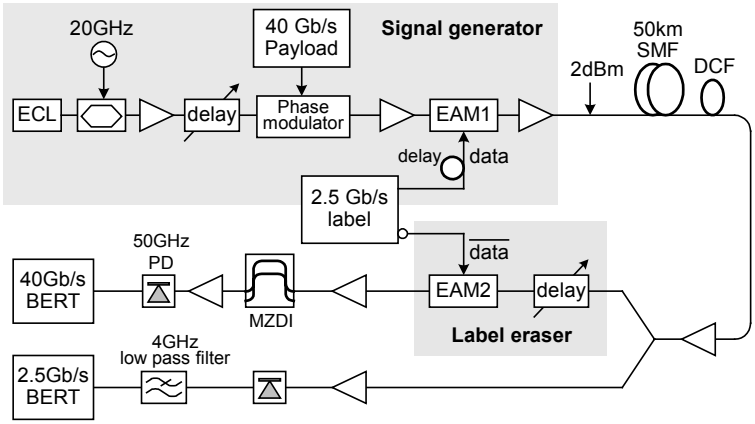

Fig. 6.23. Experimental set-up for RZDPSK(40 Gb/s)/ASK(2.5 Gb/s) labeling signal.

The experimental setup is shown in Fig. 6.23 [186]. The RZDPSK generator consists of an external-cavity laser at 1550 nm, an external dual-drive Mach-Zehnder modulator and a phase modulator. The first modulator generates a 40 GHz RZ pulse train with 33% duty cycle. The modulator is biased at the peak of its transmission curve and differentially driven at twice the switching voltage with an ac-coupled half-bit-rate (20 GHz) sine wave. The phase modulator is driven by a 40 Gb/s (PRBS 2^{23}-1) NRZ data stream. A tuneable optical delay line is inserted in between the two modulators to synchronize the pulse train and the 40 Gb/s data. The label information at 2.5 Gbit/s (PRBS 2^7-1) is added by a following EAM (EAM1), thus producing an optically RZDPSK/ASK labelled signal. As mentioned before the advantage of using the EAM for label insertion is its negligible frequency chirp. It should be noted that the receiver sensitivity of the ASK label improves as the ASK extinction ratio is increased, while the sensitivity of the RZDPSK payload deteriorates due to the reduced signal power when an ASK '0' is transmitted. Therefore, in our experiment a compromise value of 3 dB is selected for the extinction ratio of the ASK label.

The transmission span consists of 50 km standard single mode fibre with matching length of dispersion compensating fibre in post-compensation scheme. The dispersion of the SMF and the DCF is 16.9 ps/nm/km and –100 ps/nm/km, respectively.

At the receiver node, the labelled signal is split using a 3 dB optical coupler. The output of one arm is directly detected by a photodiode and thus the optical label is converted into the electrical domain.

From the second output of the coupler the labelled signal is input to another EAM (EAM2) driven by the inverted label data with suitable delay and amplitude for label erasure. The payload is then input to an integrated Mach-Zehnder delay interferometer (MZDI) to demodulate the RZDPSK signal. The length difference between the two arms of the MZDI is 5.049 mm, corresponding to 25 ps delay. The signal at the output of the MZDI is detected by a 50 GHz photodiode and input to a 40 Gb/s BER test set.

Results

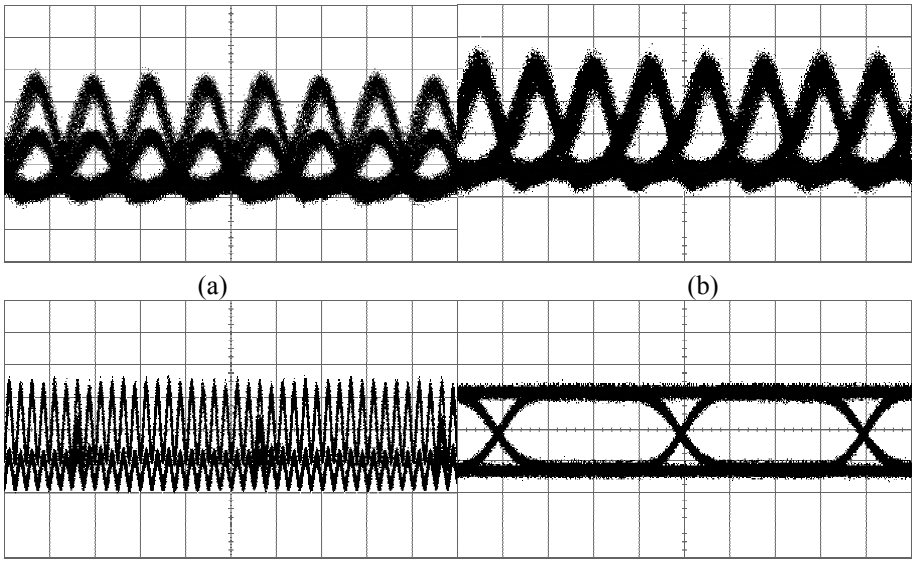

Fig. 6.24. Eye diagrams after transmission for (a) payload at 40 Gb/s without label erasure, (b) payload at 40 Gb/s with label erasure, (c) label at 2.5 Gb/s before the low-pass filter, (d) label at 2.5 Gb/s after the low-pass filter.

The detected RZDPSK eye-diagrams without and with label erasure are shown in Fig. 6.24 (a) and (b), respectively. Obviously, due to the intensity crosstalk from the ASK label, the demodulated RZDPSK payload eye-diagram presents a multi-level structure before label erasure. After label erasure, a good eye pattern of the demodulated payload is received. The received ASK label eye diagrams are shown in Fig. 6.24 (c) and (d). It is worth noting that the payload intensity (40 GHz pulses) is superimposed onto the label (see (c)), therefore a 4 GHz low-pass

electrical filter is applied after the photodiode to remove the 40 GHz RZ pulses. In this way, a very clear and open 2.5 Gb/s label eye-diagram could be obtained, as shown in (d).

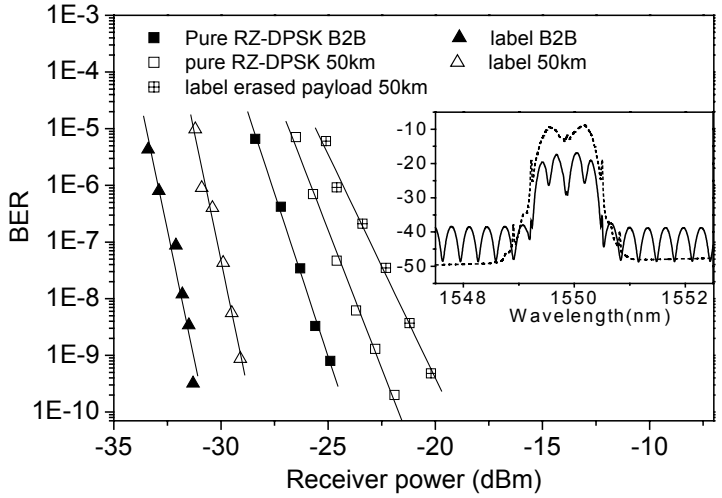

Fig. 6.25. Measured BER results for the payload at 40 Gb/s and label at 2.5 Gb/s. The inset figure shows the optical spectra of the labelled RZDPSK signal (dash line) and after label erasure and demodulation (solid line).

Fig. 6.25 shows the BER curves in the back-to-back case and after transmission over 50 km. For a pure 40 Gb/s RZDPSK signal, the back-to-back sensitivity is –25 dBm and the transmission penalty is 2.2 dB. For the optically labelled RZDPSK signal, the labelling causes an additional 2.3 dB penalty. The back-to-back sensitivity for the label is –31 dBm and the transmission penalty is less than 2 dB. The inset figure shows the optical spectra for the labelled payload and the payload after label erasure and demodulation. It is envisaged that better sensitivity performance could be achieved if a balanced-receiver were applied to the RZDPSK payload.

6.5.2 NRZDPSK/ASK label processing

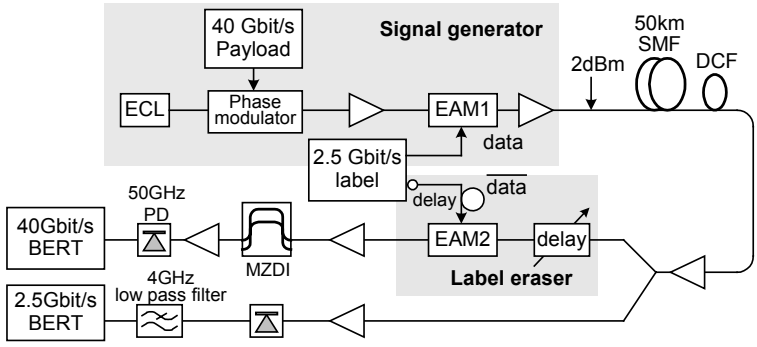

Fig. 6.26. Experimental set-up for NRZDPSK(40Gb/s)/ASK(2.5Gb/s)labeling signal.

The experimental setup is shown in Fig. 6.26 [187]. The NRZDPSK modulation is generated with a phase modulator driven by a 40 Gbit/s (PRBS 2^{23}-1) NRZ data stream. The pre-coder circuit for the NRZDPSK format is not applied in the experiment because the test signal is a PRBS pattern. The label information at 2.5 Gbit/s (PRBS 2^{7}-1) is added by a following EAM, thus producing an optically NRZDPSK/ASK labeled signal. The EAMs used here are multiple-quantum-well (MQW) devices, which are 150 μm long and contain 15 quantum wells. The fiber-to-fiber loss at zero bias is about 10 dB at 1550 nm. The static transfer curve (transmittance as a function of bias) is a quasi-linear curve up to about -2.5 V with a slope of –9 dB/V.

Fig. 6.27 (a) shows the BER curves in the back-to-back case and after transmission over 50 km. The inset figures (i) and (ii) show the detected DPSK eye-diagrams without and with label erasure, respectively. Obviously, due to the intensity crosstalk from the ASK label, the demodulated DPSK payload eye-diagram presents a multi-level structure before label erasure. After label erasure, a good eye pattern of the demodulated payload is received. The received ASK label eye diagrams are shown in Fig. 6.27 (iii).

For a pure 40 Gb/s DPSK signal, the back-to-back sensitivity is 16.5 dBm and the transmission penalty is 2.3 dB. For the optically labeled DPSK signal, the labeling causes an additional 5 dB penalty. The back-to-back sensitivity for the label is –31.1 dBm and the transmission penalty for the label is around 2 dB. It is envisaged that better sensitivity performance could be achieved if a balanced-receiver were applied to the payload.

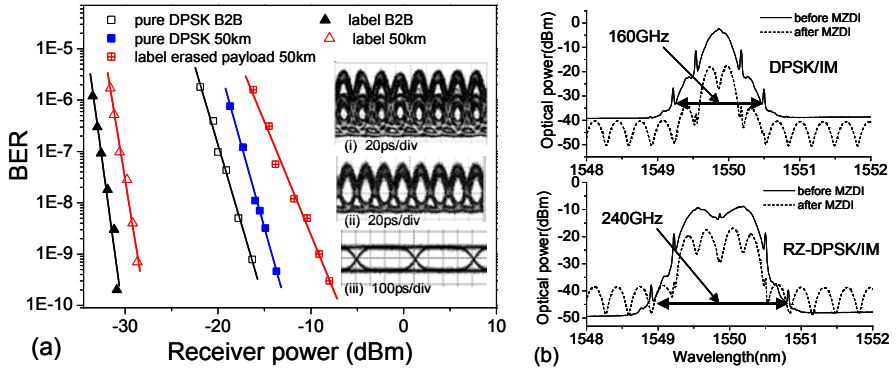

Fig. 6.27. (a) Measured BER results for the payload and label for DPSK(40Gb/s)/ASK(2.5Gb/s) labeling, the inset figures show the eye diagrams for (i) payload without label erasure, (ii) payload with label erasure, (iii) detected label, (b) the optical spectra of the DPSK/ASK labeling (above) and RZDPSK labeling (below).

Compared to our previous results on the RZDPSK/ASK scheme presented in the last subsection, the labelling penalty for the payload is 2.7dB larger, while the label performance is almost the same no matter which kind of payload is used. Fig. 6.27 (b) shows the optical spectra in the DPSK/ASK scheme and RZDPSK/ASK scheme for the labelled payload and the payload after label erasure and demodulation. Although RZDPSK/ASK labelling shows better receiver sensitivity and smaller labelling penalty for the payload, its optical spectrum is 1.5 times wider than the DPSK/ASK labelling, which leads to smaller spectral efficiency in WDM networks. We also compare the optical spectra before and after label encoding and transmission; there is no substantial spectral broadening due to the labelling and transmission.

6.6 Label swapping based on coded-RZASK/DPSK format

As discussed in previous sections a compromise ASK extinction ratios were used for the labelling schemes in order to facilitate the phase/frequency detection. In this section we present a theoretical analysis of the modulation cross talk in the ASK/DPSK format and then

propose a new base band coding scheme for the ASK payload to mitigate this cross talk. We will present our experimental investigations of EAM-based label swapping based on a 40 Gb/s RZASK payload and a 622 Mb/s DPSK label using this new coding scheme.

6.6.1 Modulation cross talk

For easy discussion we only focus on the transmitter and receiver of an optical ASK/DSPK system; the schematic configuration is shown in Fig. 6.28. The laser source is intensity modulated to generate the ASK payload. The DPSK label is then encoded in the subsequent phase modulator. At the receiver, the labelled signal is split using a 3 dB optical coupler. The output of one arm is directly detected by a photodiode and thus the ASK payload is converted into the electrical domain. The other arm is used for the label detection. The DPSK label is either detected by a Mach-Zehnder delay interferometer (MZDI) followed by a photodiode connected to one of the output ports, thus forming a single-ended receiver, or detected by a dual detector receiver connected to both output ports, forming a balanced receiver (see Fig.28).

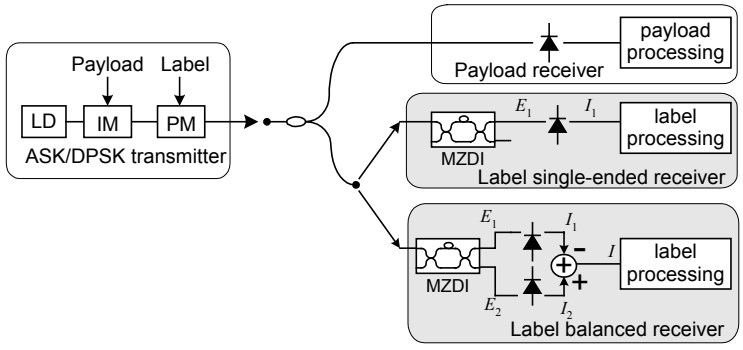

Fig. 6.28. Configuration of the optical ASK/DPSK transmitter and receiver.

The MZDI has a relative time delay between its two arms equal to the label bit period T. The analytical field at the output of the transmitter is given by

$$E_{in}(t) = \sqrt{P}\,A(t)\exp\{j[\omega_c t + \phi(t)]\} \tag{6.4}$$

where P is the average optical power and ω_c is the optical carrier angular frequency. $A(t)$ stands for the modulated amplitude containing the payload data, and $\phi(t)$ is the DPSK modulated phase corresponding to the label information. Assuming the coupling ratio of the two couplers in the MZDI is exactly 3 dB, the output electrical fields of the MZDI $E_1(t)$ and $E_2(t)$ can be obtained by the transformation.

$$\begin{bmatrix} E_1(t) \\ E_2(t) \end{bmatrix} = \begin{bmatrix} 0.5 & 0.5e^{j\pi} \\ 0.5e^{j\pi/2} & 0.5e^{j\pi/2} \end{bmatrix} \cdot \begin{bmatrix} E_{in}(t-T) \\ E_{in}(t) \end{bmatrix} \tag{6.5}$$

A: Single-ended receiver

The responsivity of the photodiode is R; the electrical current $I_1(t)$ of the single-ended receiver after the photodiode is then given by

$$I_1(t) = R\left|E_1(t)\right|^2 = \frac{1}{4}RP\left[A(t-T)^2 + A(t)^2 - 2A(t-T)A(t)\cos\Delta\phi\right] \tag{6.6}$$

where $\Delta\phi = \phi(t) - \phi(t-T_L)$ denotes the phase shift between two neighbouring label bits. The power levels resulting from single ASK bit interference has been previously shown in Section 6.3, Table 6.1. As discussed therein a photodiode with a low bandwidth is usually used for the detection of the DPSK label, thus the power levels averaged within one DPSK bit-time will result due to the slow response, instead of the subtle ASK structure. We have given an analytical expression for the possible power levels for a finite ASK extinction ratio as shown in Eq. (6.3). The averaged power levels correspond to a power density function (PDF) for both mark and space bits. Error probability can then be obtained through setting a threshold and analysing the PDFs.

Here, we assume the payload and label are synchronized and the payload bit rate divided by label bit rate is an integer N, therefore in each DPSK label bit-time N ASK bits of one arm overlap with their counterpart of the other arm, resulting in a total of 2^{2N} combinations. We also use a normalized power and an ideal extinction ratio for the ASK payload, i.e., $P_1=1$ and $P_0=0$. Under these conditions the power levels for the mark bits resulting from the constructive interference are

$$L_{mark}^{S}(j,k)=\frac{4j+k}{4N},\ \ 0\le j\le N,\ \ 0\le k\le \min(3,N-j) \tag{6.7}$$

The probabilities of the power levels shown in Eq. (6.7) are

$$P_{mark}^{S}(j,k)=Ph(4j+k)+u(j-1)\sum_{c=0}^{j-1}Ps(j-c,k+4c) \tag{6.8}$$

$$Ph(x)=\frac{1}{4^N}\sum_{m=0}^{x}\binom{N}{m}\binom{N-m}{x-m} \tag{6.9}$$

$$Ps(x,y)=\frac{1}{4^N}\binom{N}{x}\sum_{d=0}^{y}\binom{N-x}{d}\binom{N-x-d}{y-d} \tag{6.10}$$

$$u(x)=\begin{cases}1 & x\ge 0\\ 0 & x<0\end{cases} \tag{6.11}$$

The corresponding solutions for the space bits are shown in Eqs. (6.12-6.13),

$$L_{space}^{S}(j)=\frac{j}{4N},\ \ 0\le j\le N \tag{6.12}$$

$$\begin{aligned}&P_{space}^{S}(j\ge 1)=\frac{1}{4^N}\Big[\sum_{m=0}^{j}\binom{N}{m}\binom{N-m}{j-m}\Big]\Big[\sum_{k=0}^{N-j}\binom{N-j}{k}\Big],\\ &P_{space}^{S}(j=0)=1-\sum_{j=1}^{N}P_{space}^{S}(j\ge 1)\end{aligned} \tag{6.13}$$

Based on Eqs. (6.7)-(6.13) the impact of the ASK payload on the detection of the DPSK label, i.e., the modulation cross talk, can be studied. The calculated probability density functions (PDF) of the mark and space bits for the single-ended receiver are shown in Fig. 6.29 with *N* being 4, 10, 16 and 32.

It is found that the number of the power levels due to the DPSK detection increases with the bit rate ratio *N*, and the PDFs for the mark and space tend to take a Gaussian-like envelope when *N* is increased. The mark acquires a larger distribution width than the space as can be understood by considering the fact that the constructive interference

generates more levels and larger level separations than the destructive operation as discussed in Section 6.3.

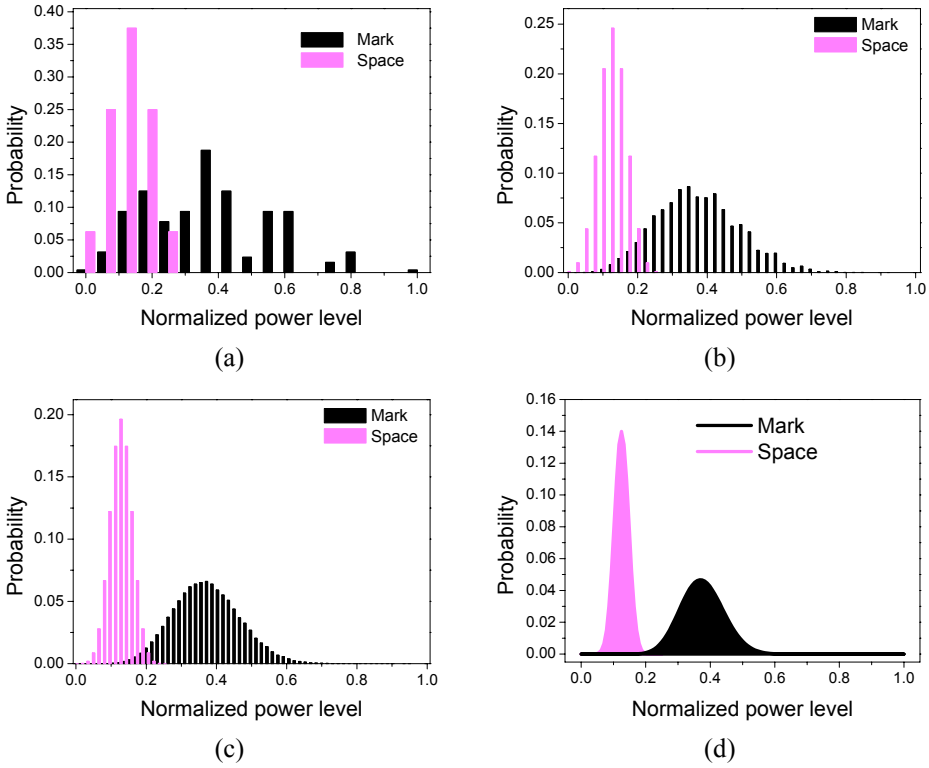

Fig. 6.29. Probability density functions for the single-ended receiver for various N, (a) N=4, (b) N=10, (c) N=16, (d) N=32.

For a small N (e.g., 4) a very large overlapping area between the mark and space is found. The columns in the power range from 0 to 0.25 in Fig. 6.28(a) correspond to the purely orthogonal interference for the mark and partially orthogonal interference for the space. In case of constructive interference, the zero level corresponds to the case that all ASK bits in the two interfering DPSK bits are zeroes and 0.25 results when the interfering ASK-pairs take the form of (10) or equivalently (01) as given by Eg. (6). With the increase of N the overlapping area between the PDFs decreases and hence the bit errors are also expected to be smaller. Fig. 6.28 also suggests a threshold near 0.2 for making decision because this is where the two PDFs intersect.

B: Balanced receiver

For the balanced receiver, the output electrical current can be written as,

$$I(t) = I_2(t) - I_1(t) = RP \cdot A(t-T)A(t)\cos\Delta\phi \tag{6.14}$$

As seen the mark bits and the space bits have the same characteristics in terms of the power levels and the associated occurring probabilities. The analytical solutions are,

$$L^{B}_{space/mark}(j) = \frac{j}{N}, \quad 0 \le j \le N \tag{6.15}$$

$$\begin{aligned} P^{B}_{space/mark}(j \ge 1) &= \frac{1}{4^N}\binom{N}{j}3^{N-j}, \\ P^{B}_{space/mark}(j = 0) &= 1 - \sum_{j=1}^{N} P^{balance}_{space/mark}(j \ge 1) \end{aligned} \tag{6.16}$$

The calculated probability density functions (PDF) of the mark and space bits for the balanced receiver are shown in Fig. 6.30, again with N being 4, 10, 16 and 32. As expected the mark and space in this case have the same distribution except that the power levels of the space has an opposite sign compared to those of the mark. It is also found that a Gaussian-like envelope is developed for larger values of N for both the mark and space.

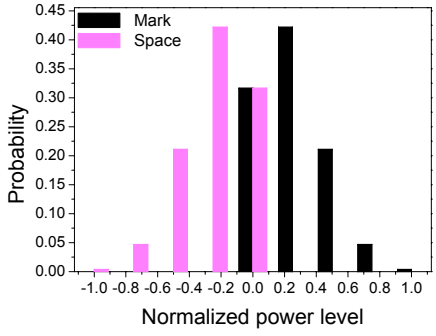

(a)

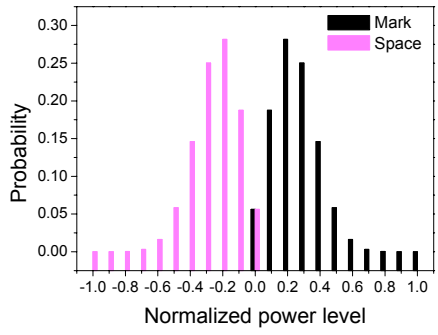

(b)

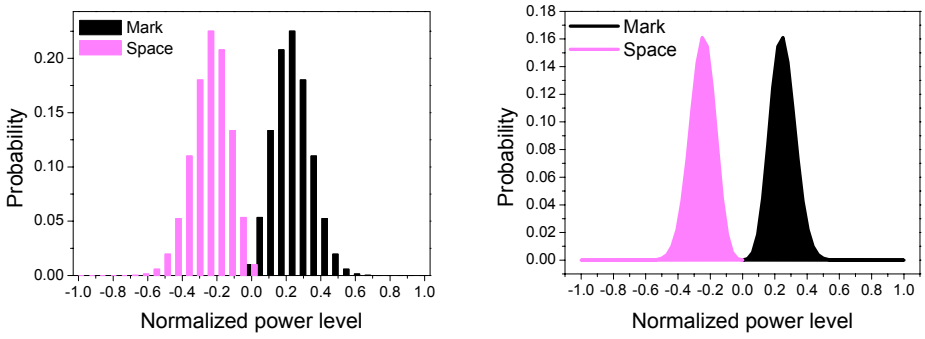

Fig. 6.30. Probability density functions for the balanced receiver for various N, (a) N=4, (b) N=10, (c) N=16, (d) N=32.

C: Error probability

In case of the balanced detection, the mark current $I_1(t) \geq 0$ and the space current $I_0(t) \leq 0$. We set the threshold to zero and interpret the power levels above zero as the mark and those below zero as the space. The error probability can be analytically formulated as shown in Eq. (6.17)

$$P_{error}^{balance} = (\frac{3}{4})^N \tag{6.17}$$

By setting the threshold to 0.2 the error probabilities for the single-ended receiver at various bit rate ratios can be obtained by summing the error columns as shown in Fig. 6.31, where the result for balanced detection is also depicted for comparison and the inset is an enlarged picture for small values of N (<25).

As seen from Fig. 6.31 the error probability decreases as N increases, suggesting that with a fixed payload bit rate the label signals of lower bit rates are more robust to the modulation cross talk. For small values of N (<13) the single-ended receiver has better performance as illustrated by the inset in Fig. 6.31. However, this is not very meaningful because the error probabilities in this range are larger than 10^{-2}, which is not allowed in real systems. The balanced detection generally shows lower error probabilities and a fast decrease with N. When N is larger than 73 for balanced detection and 130 for single-ended detection the error free

operation (BER<10^{-9}) is obtained without considering other system factors such as noise and timing jitter.

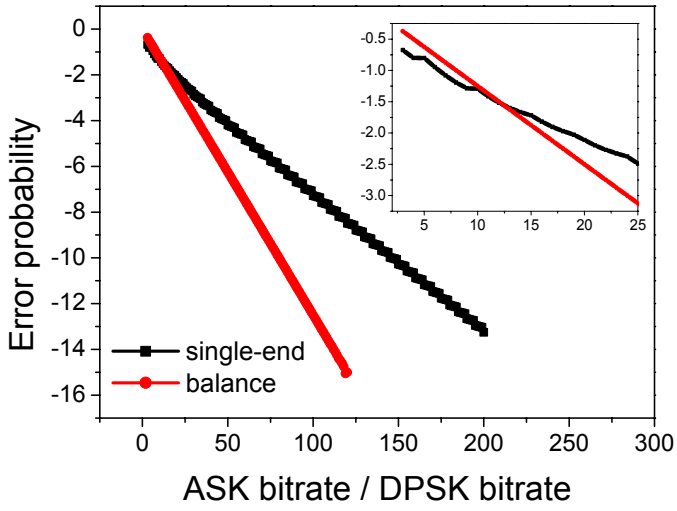

Fig. 6.31. Error probability versus bit rate ratio of the ASK payload to the DPSK label.

This means that for a 40 Gb/s ASK/622 Mb/s DPSK system (N=64) the label is not detectable even with zero noise. In fact, the real system suffers from various noise contributions and timing jitter, which make the label detection more difficult. As seen in Fig. 6.31, by reducing the label bit rate such that N is larger than 100 the error probability for balanced detection is decreased to a level about 10^{-14}, which in principle shouldn't be a problem for real systems. However, using the DPSK modulation format for relatively lower bit rate labels will result in a strict requirement on the laser line-width [43]. Moreover, the temperature and mechanical stabilization of the MZDI used for the DPSK demodulation will become a challenge due to the large delay between the two arms. In practice the maximum acceptable length difference is generally around 10-30 cm, which means that the DPSK bit rate has to be higher than 622 Mb/s. According to our analysis, for a 40 Gb/s payload this label bit rate cannot provide error free operation neither for the single-ended receiver nor the balanced receiver. Therefore without a special coding of the payload, the payload extinction ratio has to be sacrificed.

D: Requirement on the payload extinction ratio

If the payload extinction ratio is a finite value ε, the signal detected by a balanced receiver is in principle detectable because $A(t) > 0$. Based on our previous investigation in [176], the eye-opening Y for a single-ended receiver is given by

$$Y = 10^{-\frac{\varepsilon}{10}} - \frac{1}{4}[1 + 10^{-\frac{\varepsilon}{10}} - 2\sqrt{10^{-\frac{\varepsilon}{10}}}] \tag{6.18}$$

To get Y > 0, ε should be less than 9.5 dB. If the label receiver sensitivity is set to be around the same level as for the payload, and the noise is taken into consideration, the payload extinction ratio has to be further decreased to 3-4 dB as we examined in the earlier experiments. Such low extinction ratio will obviously degrade the system performance and will give rise to problems in multi-hop scalability, and all-optical processing on the payload such as 2R/3R regeneration, and wavelength conversion. Therefore it is critical for the ASK/DPSK labelling to find effective ways to enhance the payload extinction ratio while maintaining the proper DPSK detection at the same time.

6.6.2 Coding scheme

Several coding methods have been proposed to improve the system performance of optical labelling by reducing the modulation crosstalk between the payload and label, including Manchester-coding for ASK/FSK labelling [184], Manchester-coding for sub-carrier multiplexing labelling [192], 8B10B coding for ASK/FSK labelling [190], 8B10B coding for ASK/ASK labelling [193] and interleaved DPSK label for ASK/DPSK labelling [191].

The advantage of the Manchester-coding and 8B10B coding can be understood based on spectrum shaping. In the base band domain, cross talk between the payload and label is generated by overlap of the payload spectrum with the label spectrum. Because the label bit rate is typically much lower than the payload bit rate due to the small amount of control information, the label signal is thus a narrow-band signal. If we shape the payload spectrum by pushing it to higher frequencies and leaving

negligible components in the region of the label spectrum, the cross talk will be suppressed significantly. Several line coding techniques can generate a DC-null spectrum, such as Manchester-coding and 8B10B. The Manchester coding has advantages in clock-recovery and burst-mode data reception, however it doubles the bandwidth requirements on the payload transmitter and receiver and hence the bandwidth efficiency is only 50%. The 8B10B coding is popular in an Ethernet environment and has a relatively high bandwidth efficiency of 80%.

Another kind of coding method, interleaved DPSK label, is best understood in the time domain. Assuming the DPSK bit rate is N times lower than the payload bit rate, a pair of 'mark' bits are inserted every N-2 payload bit-frame. The DPSK label is synchronously modulated on the payload with the edge of the label bits aligned with the middle of the pair of mark bits. To detect the DPSK label a MZDI with a delay matching the payload bit rate has to be used [191]. The bandwidth efficiency of the payload is N-2/N. It has a better bandwidth efficiency than the 8B10B coding when N is larger than 10. However this scheme requires precise synchronization and timing alignment between the inserted payload mark pairs and the label edges. Furthermore, it requires that the transition time (rising and falling edge) of the label bit is very small compared to the payload bit-duration, which results in an extra bandwidth requirement on the label transmitter.

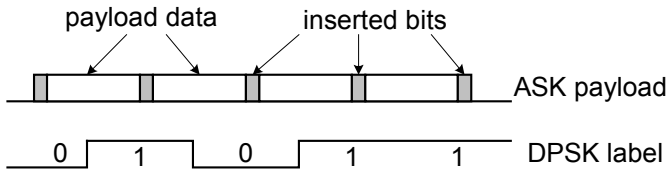

Fig. 6.32. Mark-insertion coding scheme.

We propose a new coding scheme realized in the time domain, hereafter referred to as the mark-insertion coding. The principle of this method is depicted in Fig. 6.32. We insert only one mark for every N-1 bits of the payload. In contrast to the interleaved DPSK label scheme, the DPSK label only needs to be coarsely synchronized with the payload so as to prevent the edge of the label bits from cutting the manually inserted mark. The delay of the label demodulator is equal to the label bit-time. The payload bandwidth efficiency of our scheme is given by N-1/N. For

instance, if the payload is 40 Gb/s ASK and the label is 2.5 Gb/s DPSK, the bandwidth efficiency of the payload is 93.75%. Using this coding scheme the ASK extinction ratio can be very high without affecting the label detection.

6.6.3 Experimental set-up and Results

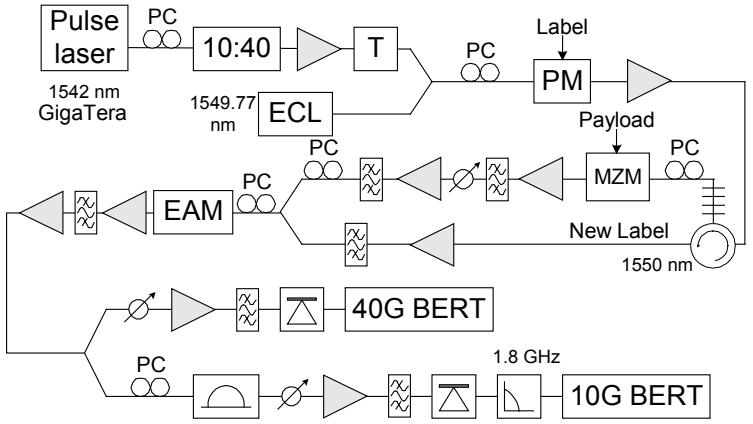

Fig. 6.33. Experimental set-up for label swapping based on RZASK(40Gb/s)/DPSK(2.5Gb/s) labeling scheme using mark-insertion coding.

The experimental set-up is shown in figure 33. An Erbium glass oscillator pulse generating laser (ERGO PGL), operating at 1542 nm, generates a short pulse train at 10 GHz with FWHM pulse width of 1.4 ps, which is optically multiplexed to 40 GHz through fibre-based time interleaving. An external cavity laser (ECL) generates a cw light wave at 1550 nm, which is combined with the short pulse train and injected into a phase modulator (PM), where the label information is encoded. At the output of PM we have two signals at different wavelengths, both having 622 Mb/s label information on the phase. They are separated through an optical add-drop multiplexer (OADM). The cw light wave comes out of the reflection port of the OADM and the pulse train exits from the transmission port. The spectra of the OADM is shown in Fig. 6.34.

The labelled pulse train is then payload-encoded by a Mach-Zehnder modulaor (MZM) through intensity modulation, where an optical time delay (T in the set-up) is employed to optimize the modulation. The labelled signal is then combined with the cw light and inserted into the

EAM, where label swapping is performed through wavelength conversion. The payload information is duplicated onto the cw light wave and the original phase information of the cw light wave, here serving as a new label, almost transparently passes through. As a result we have performed label erasure, label reinsertion and wavelength conversion by an EAM simultaneously. The eye diagrams of the back-to-back payload and label are shown in Fig. 6.35 and those of the swapped signal are shown Fig. 6.36.

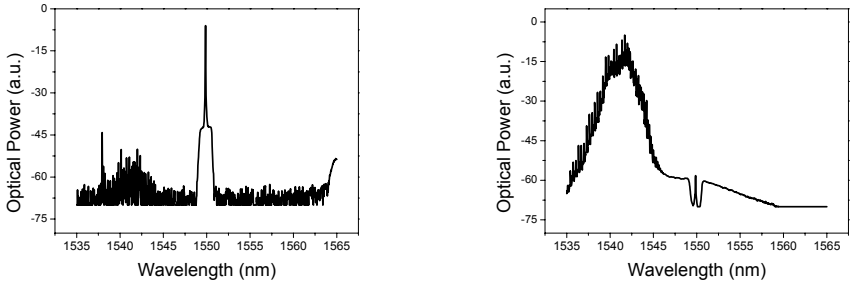

(a) (b)

Fig. 6.34. Spectrum at (a) reflection and (b) transmission port of OADM.

(a) (b)

Fig. 6.35. Eye diagrams of the (a) payload at 40 Gb/s and (b) label at 2.5 Gb/s in back-to-back case.

As seen in Fig. 6.35 the original ASK payload has a very good extinction ratio of ~12 dB, which is otherwise not allowed if the mark-insertion coding wasn't used. The high extinction ratio is very desirable for the detection of high-speed signals (e.g. 40 Gb/s) and for wavelength conversion using EAMs. It is found from Fig. 6.36 that the ASK payload of the wavelength converted signal has very thick eyelids and thus a poor extinction ratio. This is due to the relatively slow response speed and the

moderate static extinction ratio of 5 dB/V of the EAM used. However, the ASK eye is still open and detectable. The eyes of the demodulated DPSK label can be understood by considering the mark-insertion coding scheme we discussed previously. From Fig. 6.36 it is clearly seen that the original phase information of the cw light is well preserved after wavelength conversion.

(a) (b)

Fig. 6.36. Eye diagrams of the (a) payload at 40 Gb/s and (b) at 2.5 Gb/s label after label swapping.

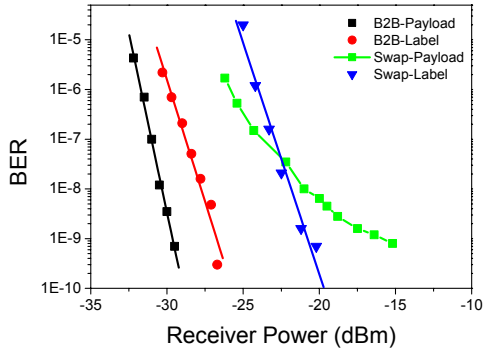

Fig. 6.37. Measured BER curves for the payload at 40 Gb/s and label at .25 Gb/s in back-to-back case and after label swapping.

The measured BER curves are shown in Fig. 6.37. The receiver sensitivities of the payload and label in back-to-back case are –29.6 dBm and –26.7 dBm, respectively. The power penalty of the label after swapping is about 6 dB. As indicated by the green line in Fig. 6.37, the payload achieves error free operation after swapping, however, accompanied by an error floor. According to our previous discussions of wavelength conversion at 40 Gb/s in chapter 4, a much better payload

performance is expected depending on the choice of a well-designed EAM. It should be noted that due to practical reasons our 50 Gb/s test set can not yet measure bit errors of user-defined patterns. The BER results for the payload shown in Fig. 6.37 were measured using a PRBS of pattern length 2^{15} –1. This replacement is justified by considering that the PRBS has more complex pattern structure than the code we used and therefore constitutes a more difficult situation. The coded payload performance is expected to be better.

6.7 Summary

In this chapter we discussed applications of EAMs in optical label processing using various orthogonal labelling schemes.

Through EAM-based wavelength conversion label encoding and recognition are realised for two-level labelled signals consisting of a 10 Gb/s ASK payload and a 2.5 Gb/s DPSK label. The receiver sensitivities for the payload/label in back-to-back case and after label encoding are –25.6/-28.1 dBm and –23.7/-21 dBm, respectively. The results confirm that the ASK and DPSK components of the converted signal can both have BERs as low as 10^{-9}, and optical label encoding/recognition are thus successfully realized. The experiment also provides a simple approach to evaluate the phase distortion and thus the frequency chirp of the converted signal. By comparing the experimental data with simulated results using a simple model for the chirp, we arrive at an estimate of the chirp α-parameter. The influence of dynamic changes of the α-parameter is analysed. In case of using an EAM as a wavelength converter, we found the phase distortion due to chirp to be relatively small. This is attributed to the variation of α with voltage, allowing relatively high values for the maximum value of α.

Using an EAM for optical label insertion and a MZ-SOA for optical label erasure and payload regeneration in the ASK(10 Gb/s)/FSK(312 Mb/s) orthogonal modulation format, the complete functionality of a network node including two-hop transmission and all-optical label swapping is experimentally demonstrated. Compared to the back-to-back case (-24. 2dBm sensitivity) the 10 Gb/s ASK payload shows 2 dB penalty due to the first hop transmission, 3 dB improvement by SOA-

based wavelength conversion used for label erasure and regeneration, 1.4 dB penalty due to EAM-based label reinsertion and 1.5 dB penalty due to the second hop transmission. The 312 Mb/s FSK label, with a back-to-back sensitivity of –32.6 dBm, shows 3.4 dB penalty stemming from the first hop transmission, 3.1 dB improvement by SOA-EAM and 1.5 dB penalty due to the second hop transmission. Hence, the cascaded transmission and label swapping result in 1.9 dB power penalty for the payload and 1.8 dB penalty for the label.

Operating as external modulators, two EAMs are used to encode and erase the optical label in the RZDPSK/ASK and DPSK/ASK format. We experimentally demonstrated label encoding, transmission over a 50 km SMF link, and label erasure of a 40 Gb/s RZDPSK modulated payload with an orthogonal 2.5 Gb/s ASK label. For a pure 40 Gb/s RZDPSK signal, the back-to-back sensitivity is –25 dBm and the transmission penalty is 2.2 dB. For the optically labelled RZDPSK signal, the labelling causes an additional 2.3 dB penalty. The back-to-back sensitivity for the label is –31 dBm and the transmission penalty is less than 2 dB. A similar experiment was carried out for a NRZDPSK/ASK labelled signal. For a pure 40 Gb/s NRZDPSK signal, the back-to-back sensitivity is 16.5 dBm and the transmission penalty is 2.3 dB. For the optically labelled DPSK signal, the labelling causes an additional 5 dB penalty. The back-to-back sensitivity for the label is –31.1 dBm and the transmission penalty for the label is around 2 dB. Compared to the RZDPSK/ASK scheme, NRZDPSK/ASK has a smaller spectrum width and the labelling penalty for the payload is 2.7dB larger while the label performance is almost the same.

The modulation cross talk between the ASK payload and the DPSK label is theoretically analysed. As a result it is found that for a noiseless ASK/DPSK system with an infinite ASK extinction ratio, error free detection of the label can be obtained when the payload bit rate is at least 73 times larger than that of the label in case of balanced detection. For the single-ended DPSK receiver an even larger bit rate ratio (~130) is needed. Since real DPSK systems work at a relatively high bit rate this condition is normally not met. To solve this problem, instead of using a moderate ASK extinction ratio, we introduced a base band coding scheme named mark-insertion coding for the ASK payload and using this coding scheme we realised label swapping based on a RZASK payload at 40 Gb/s and a DPSK label at 622 Mb/s using an EAM as the label swapper.

It should be summarised that the superior chirp property of an EAM is the key to all these applications. An EAM can modulate the intensity (through either e/o or o/o modulation) of a signal with negligible phase interference. In case of the ASK/DPSK or ASK/FSK labelling schemes, EAM-based wavelength conversion can be used for label swapping due to the low o/o chirp. As for the DPSK/ASK labelling scheme, the small e/o chirp of an electrically modulated EAM makes it possible to intensity-modulate a phase-modulated signal without distorting the phase, which is a good way forward to label encoding and erasure.

7

Optical labelling using polarization modulation

In the last chapter we have discussed several orthogonal modulation formats used for optical labelling systems as well as the associated label processing techniques using EAMs. It has been shown that there is an inherent modulation crosstalk between the payload and the label for all the labelling schemes discussed so far, where the payload and the label information are encoded on amplitude and phase/frequency of the optical carrier, respectively. This modulation crosstalk originates from the requirement of the limited extinction ratio (less than 9.5 dB for the single-ended DPSK receiver) of ASK modulation because a certain amount of optical power is necessary to carry the phase/frequency information and thereby enable detection. Base band coding techniques can partially release the restriction of the ASK extinction ratio but increase the signal bandwidth and reduce information carrying efficiency.

We propose a new optical labelling scheme in this chapter, which entirely eliminates the modulation crosstalk suffered by all previous labelling systems. The new modulation format is called DPSK/PolSK labelling, where PolSK stands for polarization shift keying. In this labelling scheme the payload is DPSK modulated on the phase and the label is PolSK modulated on the polarization of an optical carrier.

We will first give an overview of polarization modulation, and then introduce our PolSK system including polarization modulation, detection and erasure. Next we will present our label swapping and transmission experiment based on the DPSK/PolSK scheme proposed. Finally, a discussion of PolSK and a summary will be given.

7.1 Polarization modulation

Optical light has five basic properties that can be modulated to carry data information, i.e., amplitude, phase, frequency, polarization and direction. The first three properties have been extensively studied and widely used for information transmission and optical signal processing. Direction of a light beam more likely belongs to the mechanical region and is mainly used for an optical space switch, e.g., Mach-Zehnder switch [194], directional coupler switch [195] and intersectional switch [196]. Polarization is an intrinsic optical characteristic of a light wave, which has been used for polarization multiplexing to increase the capacity of OTDM systems [e.g., 5] and for optical signal processing, e.g., in ultra-fast non-linear interferometers [35]. Polarization modulation used for data transmission has in the literature been named polarization shift keying and has been extensively studied both theoretically [197-206] and experimentally [207-213]. PolSK was first proposed to achieve high immunity to laser phase noise with a limited penalty with respect to the quantum limit of conventional coherent systems [207,208]. Various detection schemes have been investigated to achieve stable system performance, including amplitude detection [202,205,207,210,213], differential heterodyne detection [208] and Stokes parameters detection, e.g., [197,200,210]. In particular a state of polarization (SOP) and laser phase noise independent PolSK system has been proposed based on detection of Stokes parameters [e.g., 197]. Investigations have predicted that a binary PolSK system is approximately 3 dB better than a conventional ASK system in terms of receiver power [205] but has excess penalty due to polarization mode dispersion (PMD) [212].

Two polarization modulation schemes have been proposed and widely employed. The first scheme is schematically shown in Fig. 7.1.

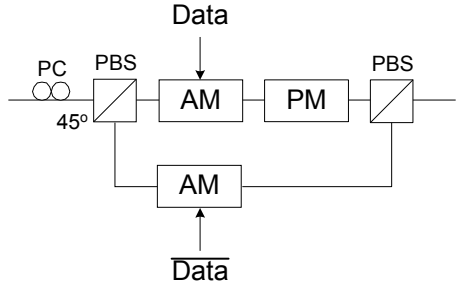

Fig. 7.1. Polarization modulation based on AM and PM.

The input light is launched with a linear polarization at 45^o with respect to the principle axis of a polarization beam splitter (PBS) and two orthogonally polarized fields of equal power are then generated at the two output ports of the PBS. These two fields are inversely modulated by two amplitude modulators (AM) and logic one and zero are then represented by two orthogonal fields. A phase modulator (PM) is used here to compensate the random phase shift between the two arms. This scheme is based on a simple idea but is very complex and it is very difficult to accurately control the phase modulator for phase compensation.

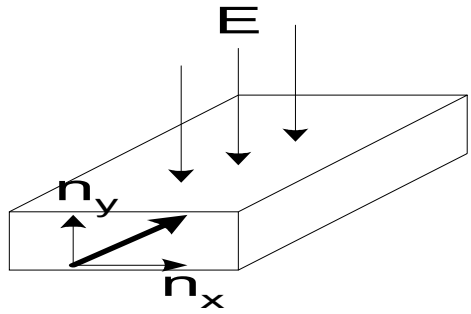

Fig. 7.2. Polarization modulation based on the $LiNbO_3$ waveguide.

Another scheme uses the anisotropy in terms of different electro-optic coefficients of $LiNbO_3$ crystals, as shown in Fig. 7.2. The applied electric field is parallel to one principle axis and obtains more efficient phase modulation of the optical field in this direction (e.g., y). Assuming the phase changes on the two orthogonal directions are $\Delta\varphi_x$ and $\Delta\varphi_y$, and $\Delta\varphi_y - \Delta\varphi_x = \pi$, then at the output the SOP of the modulated signal is rotated 90^o and polarization modulation is thus realized. Although this scheme eliminates the problem of polarization fluctuation due to random phase shift in the first scheme, a residual phase modulation ($\Delta\varphi_x$) exists and may be detrimental for some applications. For instance, for an optical labelling system based on DPSK/PolSK, the quality of the DPSK payload is then degraded by the residue phase noise.

To meet the requirement of a DPSK/PolSK labelling system, a new modulation scheme is proposed that simply uses a normal Mach-Zehnder modulator (MZM), which has been widely used for intensity modulation, phase modulation, optical pulse generation and carrier suppression.

Operating in a special but simple way, a MZM can also work as a polarization modulator.

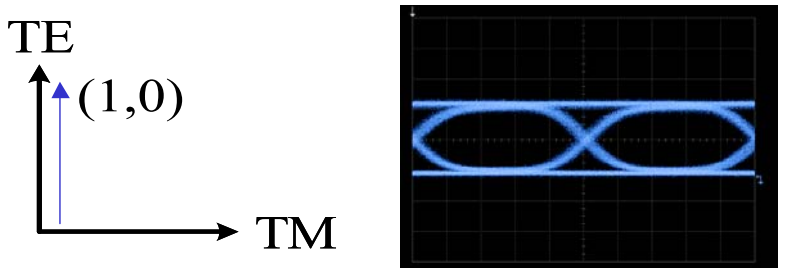

Fig. 7.3. Intensity modulation by a MZM.

The normal intensity modulation by a MZM is illustrated in Fig. 7.3. By optimizing bias, electrical data amplitude and input signal polarization, the intensity-modulated signal is achieved at the output of MZM. We define the optimized input polarization direction as TE mode, which ideally has maximum power transmission for logic "1" and zero power for logic "0", as shown in Table 7.1. It is then clear that in this case the output signal has a uniform polarization for all mark and space bits, as illustrated by the blue line in Fig. 7.3.

	TE	TM
"1"	1	1-α
"0"	0	β

Table 7.1. Power transfer coefficients for the TE and TM modes.

If we rotate the input polarization in clockwise direction to deviate from the TE mode then the TM mode starts to increase. Due to the polarization dependence of the Pockels effect, which is the principle effect used by a $LiNbO_3$ MZM, the TM mode has different power transfer coefficients from that of the TE mode. Since the TE mode is the optimized one the TM mode has the less output power for mark bits and a finite power level for space bits. This is shown in Table 7.1, where α and β are suitable parameters. The values of these two parameters depend on the material used in the MZM, but should in any case fall within the range

from 0 to 1 according to our definition. The direct consequence of the polarization rotation is to decrease the mark output power and to increase the space output. It can be easily seen that the mark and space have almost same output power at a special polarization direction, giving rise to a constant amplitude for the modulated signal, as shown in Fig. 7.4.

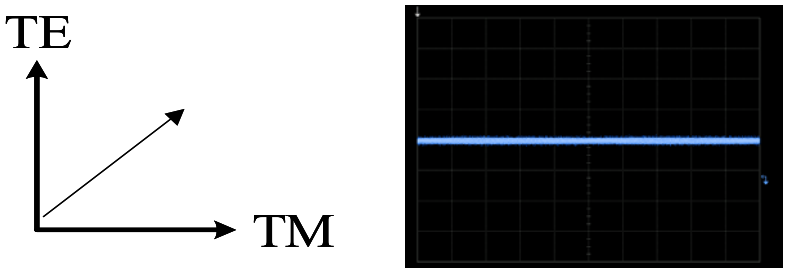

Fig. 7.4. Constant amplitude under special polarization

An implicit consequence of above adjustment is that the mark has both TE and TM mode components while the space is purely TM mode, which leads to a certain angle between polarizations of mark and space, as illustrated in Fig. 7.5.

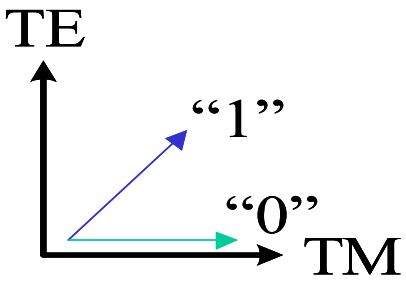

Fig. 7.5. Polarizations of the mark and space at the output of the MZM.

Polarization modulation is therefore achieved and the modulation index is related to the angle formed by mark and space polarizations. It is obvious that compared to traditional modulation schemes our new method has a moderate modulation index, but as will be shown later, the system can still perform quite well. Although constant amplitude output is obtained, intensity modulation is not completely erased. Instead, amplitude variation exists in each mode separately but is blurred when both modes are present. This gives us an indication that PolSK

demodulation can be achieved by simply suppressing one of the modes, as will be discussed next.

7.2 PolSK signal processing

The PolSK signal is easily detected by a combination of a polarization controller and a polarization beam splitter, as shown in Fig. 7.6. It will also be shown that the same set-up can be used for PolSK label erasure.

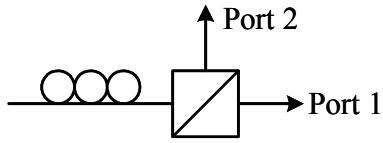

Fig. 7.6. PolSK demodulator and label eraser.

Sending the PolSK signal into the demodulator shown in Fig. 7.6 various functionalities can be realized by adjusting the input polarization controller. As shown in Fig. 7.7 (a) when the angle between the mark polarization and port 2 is equal to the angle between the space polarization and port 1, the demodulated signals exit from both ports. In Fig. 7.7 (b) the top green line is the PolSK signal, the blue and red eye diagrams are the outputs of the two ports of the polarization beam splitter. It is not necessary to specify which one is at port 1 since the same demodulated signal will appear at either port by properly adjusting the input polarization controller.

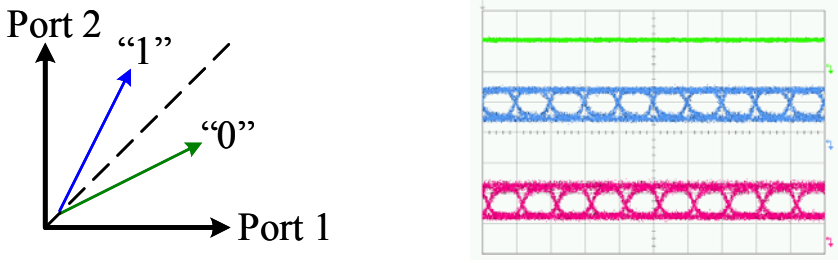

Fig. 7.7. Equal detection of both ports of the PBS. (a) Polarization direction, (b) The PolSK signal (top) and the outputs at Port 2 (middle) and Port 1 (bottom) of the PBS.

Fig. 7.8 shows the patterns of the two outputs recorded simultaneously. As expected it is found that the red trace is an inverted version of the blue one, which can be easily understood by looking at the polarization directions in Fig. 7.7 (a). The time delay between the two demodulated signals is caused by different fibre length. When configured in this way balanced detection can be used to improve system performance, much in the same way that the DPSK signal is detected.

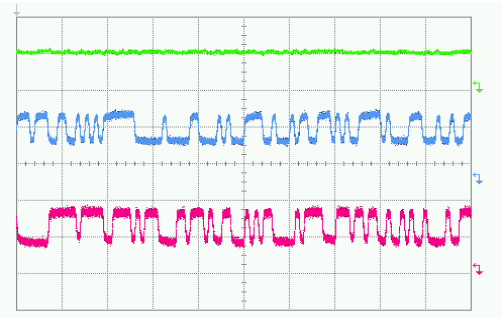

Fig. 7.8. Pattern of the PolSK signal (top), the outputs at Port 2 (middle) and Port 1 (bottom) of the PBS.

Alternatively the output from one port can be optimized by polarizing the input signal in the way shown in Fig. 7.9 (a). The space is polarised parallel to port 1 and thus vertical to port 2. Therefore at port 2 space bits have a zero output and the extinction ratio of the demodulated signal is maximized as illustrated by the middle eye diagram in Fig. 7.9 (b). At the same time a very poor eye diagram is observed due to the projection of the mark signal onto port 1 (bottom Fig. 7.9 (b)). This is the way we demodulate the PolSK signal in our optical label experiment, as will be discussed later.

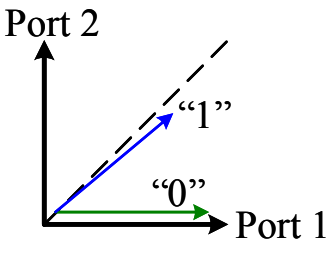

(a)

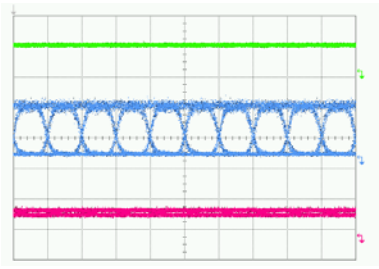

(b)

Fig. 7.9. One output of Port 1 is optimized. (a) Polarization direction, (b) The PolSK signal (top) and the outputs at Port 2 (middle) and Port 1 (bottom) of the PBS.

Since the output of a polarization beam splitter has a uniform linear polarization, label erasure has been done in this sense in previous configurations. However, in order to maintain constant amplitude at the output, a specific input polarization is used as shown in Fig. 7.10. When the angle between the mark polarization and port 2 is equal to the angle between the space polarization and port 2, they have equivalent projections in the direction of port 2 and thus have constant output amplitude (middle Fig. 7.10 (b)). At the same time, the mark and space also have the same projection on port 1 (bottom Fig. 7.10 (b)), however, it is straightforward to see that the mark and space at port 1 has a π phase difference, meaning that a PSK or DPSK signal of constant amplitude is generated. This observation may have applications in some systems, but for our DPSK/PolSK labelling system is purely detrimental and should be avoided. Consequently, only port2 is used in our labelling experiment.

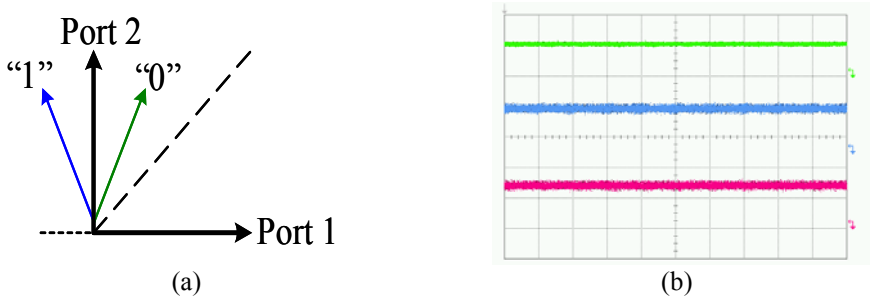

Fig. 7.10. Label erasure. (a) Polarization direction, (b) The PolSK signal (top), the outputs at Port 2 (middle) and Port 1 (bottom) of the PBS.

7.3 DPSK/PolSK labelling system

The experimental set-up for the DPSK/PolSK labelling system is shown in Fig. 7.11. An external cavity laser (ECL) generates a cw light at 1545 nm that is DPSK modulated by a phase modulator (PM) with payload data at 40 Gb/s. The DPSK signal is then amplified to a power level of 15 dBm and afterwards passes through a 3.5 nm optical band pass filter before coming into a polarization modulator (MZM1), where PolSK label at 2.5 Gb/s is encoded generating a DPSK/PolSK dually modulated signal. The label swapper performs two basic functions, i.e., label erasure

and label reinsertion. The DPSK/PolSK signal is first launched into the label eraser that is made up of a polarization controller (PC) and a polarization beam splitter (PBS), where the old polarization label is removed, yet maintaining constant amplitude. The new label is encoded in another polarization modulator (MZM2) through PolSK modulating the incoming pure DPSK signal. Label swapping is thus accomplished. The label-swapped signal is then amplified to a power level of 5 dBm and transmitted along a 40 km SMF and the corresponding DCF. Label detection is implemented by the same device as that for label erasure and a 1.8 GHz electrical low pass filter is used to suppress high frequency noises. The DPSK payload is detected by a balance detector, which comprises an optical delay interferometer and a two-port electrical amplifier.

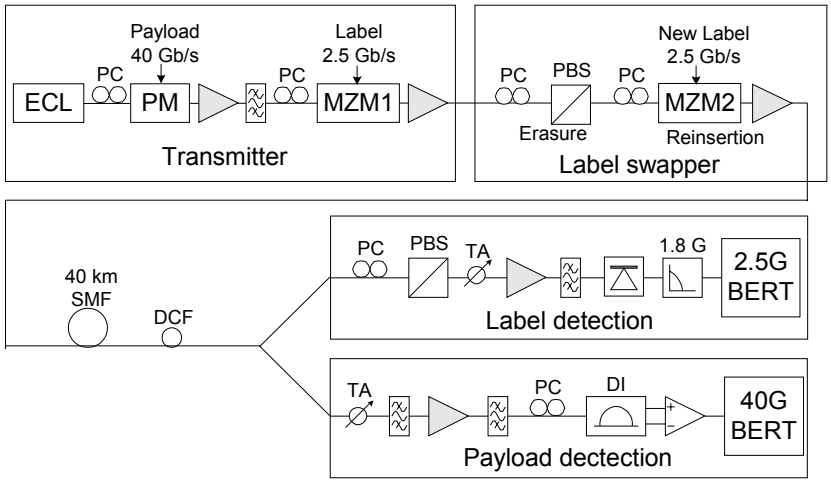

Fig. 7.11. Set-up of DPSK (40Gb/s) /PolSK(2.5 Gb/s) labelling system.

Back-to-back

The eye diagrams of the labelled signal, the detected label and the detected payload in back-to-back case are shown in Fig. 7.12. The top line in (a) is the DPSK/PolSK labelled signal, below which is the eye diagram of the demodulated label. The detected DPSK payload is displayed in (b). To investigate the transmission suitability of this new labelling format transmission along 40 km SMF with DSF is first carried out before

investigation of label swapping. The eye diagrams after transmission are shown in Fig. 7.13. The measured BER curves for the payload and the label in back-to-back case and after transmission are depicted in Fig. 7.14.

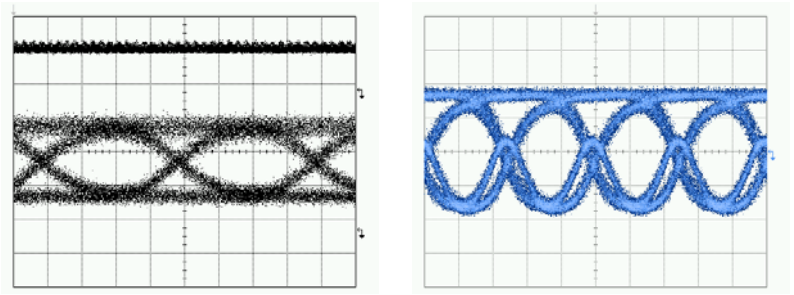

(a) (b)

Fig. 7.12. Eye diagrams of the labelled signal (a, upper) and the detected label at 2.5 Gb/s (a, lower) and the detected payload at 40 Gb/s in back-to-back case.

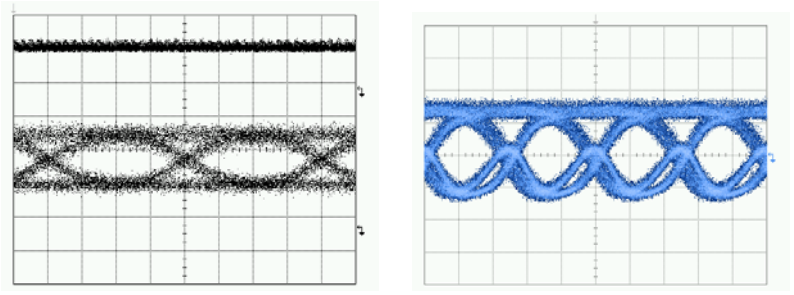

(a) (b)

Fig. 7.13. Eye diagrams of the labelled signal (a, upper) and the detected label at 2.5 Gb/s (a, lower) and the detected payload at 40 Gb/s after transmission of 40 km SMF.

In case of back-to-back receiver sensitivities of the DPSK payload and the PolSK label are –20 and –24 dBm, respectively. After 40 km transmission power penalties for the payload and the label are 0.52 and 0.96 dB, respectively, as illustrated in Fig. 7.14. It is then clear that our newly proposed labelling format works quite well and is certainly suitable for transmission.

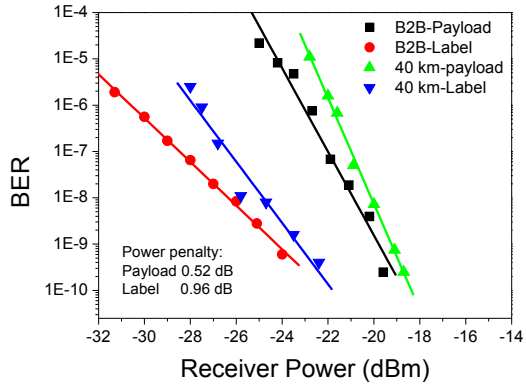

Fig. 7.14. BER curves of DPSK payload (40 Gb/s) and PolSK label (2.5 Gb/s) for Back-to-back and 40 km transmission.

Label swapping

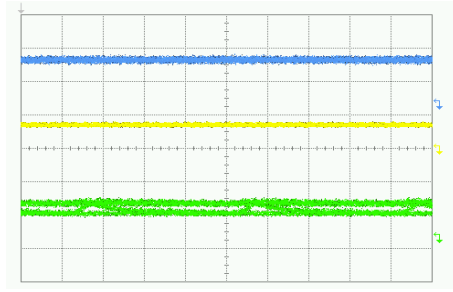

Fig. 7.15. Waveforms of the original labelled signal (top), label-erased signal (middle) and label-swapped signal (bottom) based on 40 Gb/s DPSK payload and 2.5 Gb/s PolSK label.

The signal waveforms recorded during label swapping are shown in Fig. 7.15. The top blue line is the old PolSK labelled DPSK signal. The middle yellow one is the pure DPSK payload after label erasure. The green one at the bottom is the output of the label swapper containing the old DPSK payload and the new PolSK label. It is seen that the amplitude of labelled swapped signal is not perfectly constant, which is due the imbalance between the mark and space.

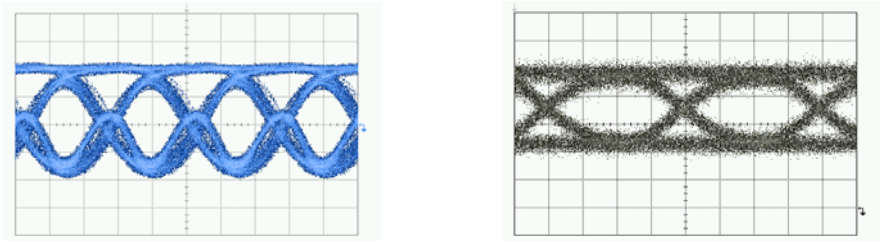

(a) (b)

Fig. 7.16. Eye diagrams of DPSK payload at 40 Gb/s (a) and PolSK label at 2.5 Gb/s (b) after label swapping.

The eye diagrams of the detected payload and label after label swapping are shown in Fig. 7.16. The measured BERs are depicted in Fig. 7.17, where BERs of back-to-back are also shown for comparison. It is found that power penalties for the payload and the label due to label swapping are 0.15 dB and 0.6 dB, respectively.

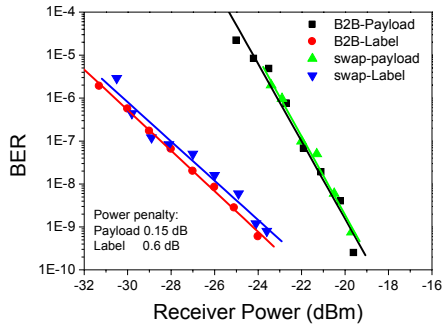

Fig. 7.17. BER curves of DPSK payload (40 Gb/s) and PolSK label (2.5 Gb/s) after label swapping.

Swapping and transmission

After label swapping the new labelled signal is transmitted along a 40 km SMF that is dispersion compensated by DCF. The eye diagrams and BER curves in this case are shown in Fig. 7.18 and 19. Receiver power penalties for the DPSK payload and the PolSK label due to label swapping and transmission are 2.2 dB and 2.9 dB, respectively.

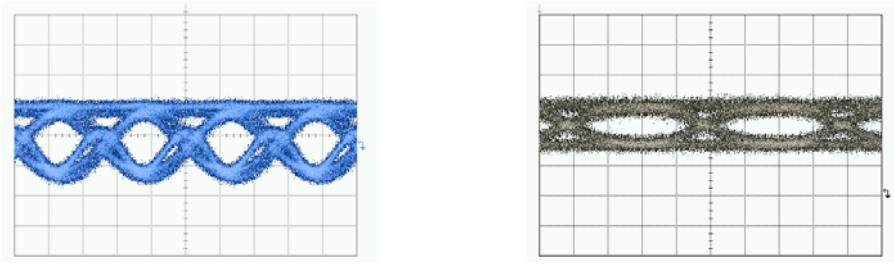

(a) (b)

Fig. 7.18. Eye diagrams of DPSK payload at 40 Gb/s (a) and PolSK label at 2.5 Gb/s (b) after label swapping and 40 km SMF transmission.

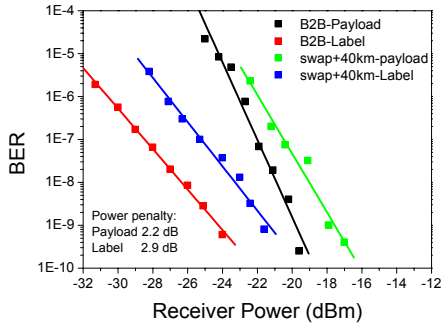

Fig. 7.19. BER curves of DPSK payload at 40 Gb/s and PolSK label at 2.5 Gb/s after label swapping and 40 km SMF transmission.

7.4 Discussion

Three-dimensional orthogonality

In chapter 6 we have shown that amplitude modulation is orthogonal to phase/frequency modulation in the sense that they can be demodulated independently of each other. Likewise, polarization modulation is orthogonal to all known modulation formats and we can construct a three-dimensional orthogonality picture as shown in Fig. 7.20.

In the plane defined by amplitude and phase/frequency there is an inherent modulation crosstalk, resulting in a limitation of the extinction ratio of the ASK format to allow for phase/frequency detection. In addition, signal crosstalk is also caused by fibre-mediated interactions

between ASK and DPSK/FSK due to chromatic dispersion and non-linearities of the optical fibre. However, PolSK is more attractive since the modulation crosstalk is eliminated and the signal crosstalk is expected to be much weaker.

Fig. 7.20. Three-dimensional orthogonality.

The three-dimensional orthogonal relation shown in Fig. 7.20 suggests that more labelling formats using PolSK are possible, e.g., ASK/PolSK. The ASK/ PolSK labelling scheme has recently been proposed and experimentally demonstrated in [214], where the PolSK label is modulated by a $LiNbO_3$-based phase modulator, erased by a polarization insensitive SOA-based wavelength converter and detected by an injection-locked Fabry-Perot laser diode. Like other orthogonal modulation formats discussed in chapter 6 the scheme in [214] has an inherent modulation crosstalk and a low ASK extinction ratio of 2.4 dB was used.

Isolation between DPSK and PolSK

To explain the isolation between DPSK and PolSK modulation a simple model of a MZM is employed as shown in Fig. 7.21. The input signal is divided into two arms with a field split ratio of k_1 for the upper arm and $\sqrt{1-k_1^2}$ for the lower arm. The signals propagating in the two arms experience a phase change of $\Delta\varphi_1$ and $\Delta\varphi_2$, respectively, before combining through the optical coupler at the output. The field transfer coefficients of the two arms of the coupler at the output are k_2 and $\sqrt{1-k_2^2}$, respectively.

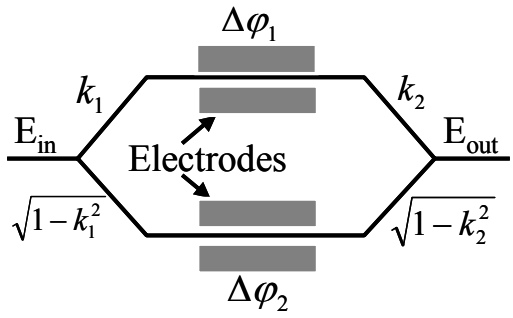

Fig. 7.21. MZM modulation model.

The input field that contains the DPSK information is given in Eq. (7.1),

$$E_{in} = \sqrt{P}\exp(-i\varphi_{DPSK}) \tag{7.1}$$

where P is optical power and φ_{DPSK} the phase information resulting from the DPSK modulation. The output signal is easily obtained and is given in Eq. (7.2),

$$\begin{aligned} &E_{out} = \sqrt{P}\exp(-i\varphi_{DPSK})\bullet \\ &[k_1k_2\exp(-i\Delta\phi_1 - \frac{\alpha_1}{2}L) + \sqrt{1-k_1^2}\sqrt{1-k_2^2}\exp(-i\Delta\phi_2 - \frac{\alpha_2}{2}L)] \end{aligned} \tag{7.2}$$

where transmission power loss on the two arms is represented by α_1 and α_2, respectively. For simplicity and without loss of generality we assume two 3 dB couplers are used in the MZM and we omit the transmission loss, meaning that $k_1^2 = k_2^2 = \frac{1}{2}$ and $\alpha_1 = \alpha_2 = 0$. Then a simplified result is obtained as shown in Eq. (7.3).

$$E_{out} = \sqrt{P}\exp(-i\varphi_{DPSK})\exp[-i(\frac{\Delta\varphi_1 + \Delta\varphi_2}{2})]\cos(\frac{\Delta\varphi_1 - \Delta\varphi_2}{2}) \tag{7.3}$$

With Eq. (7.3) we can now discuss the interactions between DPSK and PolSK modulation at the transmitter. Firstly, although intensity

modulation in a MZM is achieved through phase modulation, the DPSK information of the input signal doesn't disturb owing to the interferometric operation of the dual-drive MZM. Mathematically, the DPSK phase term that exists for both arms can be factored out as illustrated in Eq. (7.2). Secondly, a dual-drive MZM using a push-pull driving mechanism can in principle generate a chirp-free signal, meaning that $\Delta\varphi_1 = -\Delta\varphi_2$ and thus there is no residual phase modulation and the DPSK information is safely preserved. Based on the above discussion it is then clear that using the MZM-based polarization modulation scheme the DPSK payload and the PolSK label are completely isolated and thus no modulation crosstalk or limitation of the extinction ratio exist.

At the receiver we obtain amplitude detection of the PolSK label by use of a PBS that performs the conversion from polarization modulation to amplitude modulation. The detected label signal is then passed through a low pass filter that suppresses frequency components higher than the label bit rate. Therefore the DPSK information has no impact on the label detection. As to the detection of DPSK payload, a label eraser can be employed to remove polarization modulation that may possibly influence the DPSK detection since DPSK demodulators are in most cases based on fibre and are polarization sensitive to some degree. Hence, the DPSK payload and the PolSK label can be detected independently without any interactions.

Based on the above considerations a general argument is thus that DPSK and PolSK are isolated from each other and no crosstalk or interaction is allowed. This argument also applies for RZ-DPSK/PolSK and FSK/PolSK modulation formats. However, in case of ASK (NRZ/RZ)/PolSK, modulation crosstalk does exist limiting the maximum ER of the ASK signal [214], similar to that of ASK/DPSK.

Ideal polarization modulation

In the first section of this chapter we have related the PolSK modulation index to the relative polarization angle between the mark and space. The maximum modulation index, i.e. unity, then corresponds to a right angle. To achieve this a special set of power transfer coefficients for the TE and TM modes are needed, as shown in Table 7.2. If the input signal is launched at 45^o with respect to the TE mode as shown in Fig. 7.22, maximum polarization modulation is then obtained. With balanced

polarization detection all transmitted power is then used for carrying information and the system performance is highly improved.

	TE	TM
“1”	1	0
“0”	0	1

Table 7.2. Power transfer coefficients for the ideal polarization modulation.

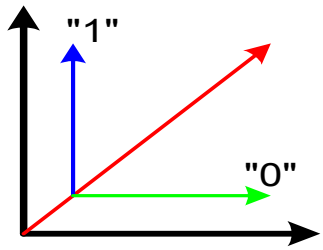

Fig. 7.22. Optimum polarization modulation.

Polarization control

As discussed previously the PolSK label encoding, erasure and detection rely on the precise control of the signal polarization, which is implemented by manual operation in the lab. At the transmitter the signal polarization at the input of the MZM can be manually optimised and needn’t further adjustment in most cases. However, when the signal is transmitter over a certain length of fibre the polarization varies randomly and slowly. It was reported in [215] that the rate of polarization fluctuations on installed optical fibre cables is in the order of hours to days and the fluctuation in the polarization angle is typically in the range of 2^0-10^0 each day, with some changes of up to about 25^0. Hence, slow dynamic polarization control can be used to compensate for the fibre-induced polarization variations. The general principle is shown in Fig. 7.23. A polarization analyzer generates an error signal by comparing the polarization at the output of the polarization controller with the polarization needed for the PolSK label erasure or detection. Based on this error signal a feedback controller generates a control signal that is

sent to the polarization controller to adjust the polarization state. In this way an automatic tracking and control of the polarization state of the received signal can be realised [216-221].

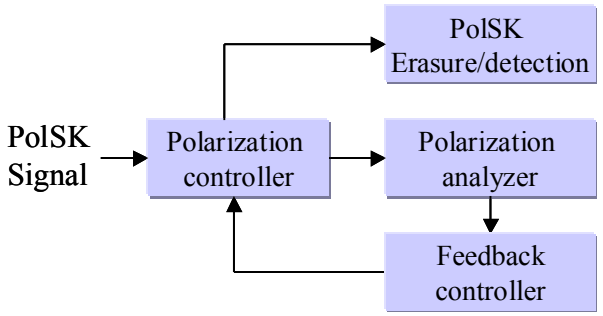

Fig. 7.23. Polarization control.

7.5 Summary

In this chapter we proposed a new polarization modulation scheme and demonstrated various signal processing functions based on PolSK modulation format. Polarization modulation is implemented by a normal MZM operating in a special but simple way. Detection and erasure of polarization information are realised by a device that is comprised of a polarization controller and a polarization beam splitter. All functions are achieved in a very simple way and using mature devices.

A new orthogonal labelling scheme based on a 40 Gb/s DPSK payload and a 2.5 Gb/s PolSK label is proposed and experimentally demonstrated. The most striking feature of this new labelling format is that there is no modulation crosstalk between the payload and the label, in contrast with all previous orthogonal modulation formats. Swapping penalties are 0.15 dB and 0.6 dB for the payload and the label respectively. Penalties due to swapping and 40 km SMF transmission are 2.2 dB and 2.9 dB for the payload and the label respectively.

We have also discussed three-dimensional orthogonality of PolSK to other modulation formats and we conclude that, in principle, PolSK can be used to form an orthogonal modulation pair with any existing modulation format. An analytical explanation for the isolation between DPSK and PolSK is given, which emphasises the use of a dual-drive MZM for the polarization modulation we proposed.

8

Conclusion

All-optical networks are a promising solution for future high-speed transparent WDM/OTDM optical communications systems. A number of network node functions need to be realized in the optical domain, preferably by use of semiconductor devices. Made of III-V group materials, electroabsorption modulators have proven to be a versatile component for all-optical networks, as manifested by its applications in integrated optical modulators, wavelength converters, demultiplexers, regenerators, optical labelling circuits, optical pulse generators and clock recovery circuits.

This thesis has presented theoretical and experimental investigations of EAMs used for all-optical signal processing and labelling.

Single and multiple channel wavelength conversion at 40 Gb/s have been experimentally demonstrated based on XAM in a single EAM. The influence of some basic characteristics, including pump light power, reverse bias of the converter and probe light wavelength, was experimentally investigated on both the wavelength-converted light itself and its chirp performance. As a result of this investigation a higher pump power (up to 20 dBm) and a relatively larger reverse bias (-2.5 V) were found to be preferable for obtaining both larger extinction ratio and lower chirp of the converted signal. As to the probe wavelength, which is as a starting point optional within the whole C-band, conversion to shorter wavelength relative to the pump showed lower frequency chirp. In the 8 × 40 Gb/s multiple channel wavelength conversion experiment, the receiver sensitivity for the back-to-back case was –33 dBm and the average power penalty for the eight converted channels was 9.2 dB. The best channel at 1555.7 nm had a power penalty of 8 dB. We explained the wavelength dependence of the power penalty by studying the impact of the extinction ratio and the average power of the converted signal on the Q parameter. In another similar system configuration, where the original data signal was a 40 Gb/s base rate signal at 1555 nm, simultaneous 7 × 40 Gb/s wavelength conversion in RZ format was realized. The receiver sensitivity for the back-to-back case was –27.3 dBm and the average

receiver power penalty for the eight converted channels was 7.4 dB. The best channel at 1554.12 nm had a power penalty of 6 dB. These experimental results suggest that EAM can be used for broadcasting in future WDM networks. A XAM model was used to simulate carrier dynamics in an EAM. Based on this model we gave physical explanations for the optimum pump power and device length, considering impacts on the extinction ratio, average power and pulse width of the wavelength-converted signal. We also briefly discussed some other wavelength conversion schemes such as fibre-based XPM and optical filtering, fibre-based Kerr switch, fibre-based FWM and SOA-based XGM. As a result of the comparison it is suggested that fibre-based solutions have relatively lower power penalties and have great potential for ultra-high speed operation while single semiconductor devices can so far operate at 40 Gb/s and are more attractive in terms of compactness, stability and integration. An important advantage of the EAM-based wavelength conversion scheme is that the frequency chirp of the converted signal is very small, which is desirable for long distance transmission and optical labelling systems.

We have experimentally demonstrated all-optical demultiplexing from a 160 Gb/s aggregated OTDM data signal to 10 Gb/s using a single EAM with a very simple waveguide structure. All 16 demultiplexed OTDM tributary channels were error free with an average receiver sensitivity of –25.3 dBm. We furthermore demonstrated an improvement up to 6 dB of the receiver sensitivity by regeneration of the demultiplexed channel by an additional EAM acting as a saturable absorber. This scheme is very promising due to the possibility of simple monolithic integration of two cascaded EAMs. We also discussed, from a system point of view, the main factors affecting the quality of the demultiplexing sub-system such as the choice of wavelength and the dependence on the pump power. An optimum pump power was found by evaluating the eye opening and the suppression of neighbour channels. Shorter wavelength for the control signal is generally preferred and the choice of the data signal wavelength depends on the trade-off between the ER and the insertion loss. A discussion about 2R regeneration based on a non-linear intensity transfer function was given. It is reiterated that a 2R regenerator can't reduce the BER but can inhibit its accumulation. The non-linear transfer function of an EAM is frequency dependent and the main improvement from an EAM-based regenerator is the enhancement of the ER and the suppression of the noise in a space.

Through EAM-based wavelength conversion label encoding and recognition were realised for two-level labelled signals consisting of a 10 Gb/s ASK payload and a 2.5 Gb/s DPSK label. The receiver sensitivities for the payload/label in back-to-back case and after label encoding were –25.6/-28.1 dBm and –23.7/-21 dBm, respectively. The results confirmed that the ASK and DPSK components of the converted signal can both have BERs as low as 10^{-9}, and optical label encoding/recognition were thus successfully realized. The experiment also provided a simple approach to evaluate the phase distortion and thus the frequency chirp of the converted signal. By comparing the experimental data with simulated results using a simple model for the chirp, we arrived at an estimate of the chirp α-parameter. The influence of dynamic changes of the α-parameter was analysed. In case of using an EAM as a wavelength converter, we found the phase distortion due to chirp to be relatively small. This was attributed to the variation of α with voltage, allowing relatively high values for the maximum value of α.

Using an EAM for optical label insertion and a MZ-SOA for optical label erasure and payload regeneration in the ASK(10 Gb/s)/FSK(312 Mb/s) orthogonal modulation format, the complete functionality of a network node including two-hop transmission and all-optical label swapping was experimentally demonstrated. The cascaded transmission and label swapping resulted in 1.9 dB power penalty for the payload and 1.8 dB penalty for the label.

Operating as external modulators, two EAMs were used to encode and erase the optical label in the RZDPSK/ASK and DPSK/ASK format. We experimentally demonstrated label encoding, transmission over a 50 km SMF link, and label erasure of a 40 Gb/s RZDPSK modulated payload with an orthogonal 2.5 Gb/s ASK label. Compared to the back-to-back case the penalties for the payload and label were 4.5 dB and 2 dB, respectively. A similar experiment was carried out for a NRZDPSK/ASK labelled signal. Compared to the RZDPSK/ASK scheme, NRZDPSK/ASK had a smaller spectrum width and the labelling penalty for the payload was 2.7dB larger while the label performance was almost the same.

The modulation cross talk between the ASK payload and the DPSK label was theoretically analysed. As a result, it was found that for a noiseless ASK/DPSK system with an infinite ASK extinction ratio, error free detection of the label can be obtained when the payload bit rate is at least 73 times larger than that of the label in case of balanced detection.

For the single-ended DPSK receiver an even larger bit rate ratio (~130) is needed. Since real DPSK systems work at a relatively high bit rate this condition is normally not met. To solve this problem, instead of using a moderate ASK extinction ratio, we introduced a base band coding scheme named mark-insertion coding for the ASK payload and using this coding scheme we realised label swapping based on a RZASK payload at 40 Gb/s and a DPSK label at 622 Mb/s using an EAM as the label swapper. It should be emphasized that the superior chirp property of an EAM is the key to all these applications. An EAM can modulate the intensity (through either e/o or o/o modulation) of a signal with negligible phase interference. In case of the ASK/DPSK or ASK/FSK labelling schemes, EAM-based wavelength conversion can be used for label swapping due to the low o/o chirp. As for the DPSK/ASK labelling scheme, the small e/o chirp of an electrically modulated EAM makes it possible to intensity-modulate a phase-modulated signal without distorting the phase, which is a good way forward to label encoding and erasure.

Finally we proposed a new polarization modulation scheme and demonstrated various signal processing functions based on PolSK modulation format. Polarization modulation was implemented by a normal MZM operating in a special but simple way. Detection and erasure of polarization information were realised by a device that was comprised of a polarization controller and a polarization beam splitter. All functions were achieved in a very simple way using mature devices. A new orthogonal labelling scheme based on a 40 Gb/s DPSK payload and a 2.5 Gb/s PolSK label was proposed and experimentally demonstrated. The most striking feature of this new labelling format is that there is no modulation crosstalk between the payload and the label, in contrast with all previous orthogonal modulation formats. Swapping penalties were only 0.15 dB and 0.6 dB for the payload and label respectively. Penalties due to swapping and 40 km SMF transmission were 2.2 dB and 2.9 dB for the payload and label respectively. We also discussed three-dimensional orthogonality of PolSK to other modulation formats and we concluded that, in principle, PolSK can be used to form an orthogonal modulation pair with any existing modulation format. An analytical explanation for the isolation between DPSK and PolSK was given, which emphasised the use of a dual-drive MZM for the polarization modulation we proposed.

In summary, we have experimentally verified that EAMs can realize several all-optical functions, such as 40 Gb/s wavelength conversion (up to eight channels), 160 Gb/s demultiplexing and optical label swapping

with payloads up to 40 Gb/s using orthogonal modulation. The advantages of using EAMs for optical signal processing are low frequency chirp, simple structure, compactness, stability, suitability for integration and low power consumption. Based on our investigations it can be concluded that EAMs, which have been commercialized and widely employed as external optical modulators, can also be used to realize various all-optical functions such as wavelength conversion, demultiplexing, regeneration and optical labelling, and thus will be a very useful components for future all-optical WDM/OTDM telecommunication networks.

However, there are still some areas that are not covered in this thesis, which need to be addressed to improve the performance of EAMs. Firstly, rather high power was used in our wavelength conversion and demultiplexing experiments. The lower power operation can be achieved by reducing the coupling loss, e.g. using spot size converters [52], which results in more signal energy launched into the active layer of EAM. The required saturation power can also be reduced by optimization of the composition and well width of the quantum wells [136]. Secondly, the devices we used were MQW-EAMs that are usually polarization dependent. The signal polarization in real systems varies randomly, which will then have a detrimental impact on the EAM-based sub-systems like wavelength converters. Polarization insensitive EAMs have been demonstrated using either a bulk structure [58] or tensile-strained quantum wells [56,57]. It would be worth investigating the applications of these devices in all-optical signal processing. As to the operation speed travelling-wave electrodes have been used for e/o modulation in EAMs. Excellent performance at 50 Gb/s has been demonstrated and the extrapolated 3dB bandwidth approached 100 GHz [222]. It would be interesting to use the TW-EAMs for signal processing through o/o modulation. Finally, in most of our experiments single EAMs were used. It is however more attractive to use EAMs integrated with other semiconductor devices like SOAs [51,52,171] to achieve better and more complex functions.

List of abbreviations

AON	All-Optical Network
AM	Amplitude Modulator
ASK	Amplitude Shift Keying
ATM	Asynchronous Transfer Mode
AWG	Arrayed-Waveguide Grating
BER	Bit-Error-Ratio
CW	Continuous Wave
DBR	Distributed Bragg Reflector laser
DFB	Distributed FeedBack laser
DI	Delay Interferometer
DILM	Dispersion Imbalanced Loop Mirror
DM	Directly Modulated diode
DPSK	Differential Phase Shift Keying
DUT	Device Under Test
E/O	Electrical-to-Optical
EAM	ElectroAbsorption Modulator
ECL	External Cavity Laser
EDFA	Er-Doped Fibre Amplifier
ERGO-PGL	Erbium Glass Oscillator Pulse Generating Laser
ER	Extinction Ratio
FBG	Fibre Bragg Grating
FEC	Forward Error Correction
FKE	Franz-Keldysh Effect
FP	Fabry-Pérot
FSK	Frequency Shift Keying
FWHM	Full Width Half Maximum
FWM	Four Wave Mixing
HN-DSF	Highly Non-linear Dispersion-Shifted Fibre
HNLF	Highly Non-Linear Fibre
IM	Intensity Modulation
IP	Internet Protocol
ISI	Inter-Symbol Interference

LN	Lithium Niobate
ML-FRL	Mode-Locked Fibre Ring Laser
MQW	Multiple Quantum Well
MZDI	Mach-Zehnder Delay Interferometer
MZI	Mach-Zehnder Interferometer
MZM	Mach-Zehnder Modulator
NA	Network Analyser
NOLM	Non-linear Optical Loop Mirror
NRZ	Non-Return-to-Zero
O/O	Optical-to-Optical
OADM	Optical Add-Drop Multiplexer
OGB	Optical Guard Band
OTDM	Optical Time Division Multiplexing
PBS	Polarization Beam Splitter
PC	Polarization Controller
PD	PhotoDiode
PDF	Probability Density Functions
PM	Phase Modulator
PMD	Polarization Mode Dispersion
PolSK	Polarization Shift Keying
PRBS	PseudoRandom Bit Sequence
QCFK	Quantum-Confined Franz-Keldysh effect
QCSE	Quantum-Confined Stark Effect
RZ	Return-to-Zero
S.W.	Switching Window
SCOOP	Semiconductor COmponents for Optical signal Processing
SDH	Synchronous Digital Hierarchy
SMF	Single Mode Fibre
SNR	Signal-to-Noise Ratio
SOA	Semiconductor Optical Amplifier
SOP	State Of Polarization
TA	Tuneable Attenuator
TCP	Transmission Control Protocol
TL	Tuneable Laser
TW	Travelling Wave

UNI	Ultra-fast Non-linear Interferometer
WDM	Wavelength Division Multiplexing
XAM	Cross Absorption Modulation
XGM	Cross Gain Modulation
XPM	Cross Phase Modulation

References

[1] Kiyoshi Fukuchi, Tadashi Kasamatsu, Masao Morie, Risato Ohhira, Toshiharu Ito, Kayato Sekiya, Daisaku Ogasahara, and Takashi Ono, "10.92-Tb/s (273 x 40-Gb/s) triple-bandultra-dense WDM optical-repeatered transmission experiment", *in Proceedings of OFC'01*, paper PD24, 2001

[2] M. Nakazawa, et al, "1.28 Tbit/s –70km OTDM transmission using third- and fourth-order simultaneous dispersion compensation with a phase modulator", *Electron. Lett*., vol. 36, no. 24, pp. 2027-2029, 2000

[3] G. C. Gupta, et al., "3.2 Tbit/s (40 × 80 Gb/s) transmission over 1000 km with 100 km span (25 dB loss) and 0.8 bit/s/Hz of spectral efficiency", *in Proceedings of OFC'02*, paper TuA5, 2002

[4] S. Kawanishi, et al., "3 Tbit/s (160 Gbit/s x 19 ch) OTDM/WDM transmission experiment", *in Proceedings of OFC'99*, paper PD1, 1999

[5] A. Suzuki, et al., "10x320Gb/s (3.2Tb/s) DWDM/OTDM transmission in C-band by semiconductor-based devices", *in Proceedings of ECOC'04*, paper Th4.1.7, 2004

[6] L. Gillner, "Transmission limitations in the all-optical network", *in Proceedings of ECOC'96*, paper TuB.2.3, 1996

[7] S. Watanabe, S. Takeda, G. Ishikawa, H. Ooi, J. G. Nielsen, and C. Sonne, "Simultaneous wavelength conversion and optical phase conjugation of 200 Gbit/s (5 x 40 Gbit/s) WDM signal using a highly nonlinear fiber four-wave mixing," *in Proceedings of ECOE'97*, Paper TH3A1-4, pp. 1525–1529, 1997

[8] C. Kolleck and U. Hempelmanann, "All optical wavelength conversion of NRZ and RZ signals using a nonlinear optical loop mirror," *J. Lightwave Technol*., vol. 15, pp. 1906–1913, Oct. 1997

[9] K. A. Rauschenbach, K. L. Hall, J. C. Livas, and G. Raybon, "All-optical pulse width and wavelength conversion at 10 Gbit/s using a nonlinear optical loop mirror," *IEEE Photon. Technol. Lett*., vol. 6, no. 9, pp. 1130–1132, 1994.

[10] Jianjun Yu, Xueyan Zheng, Christophe Peucheret, Anders T. Clausen, Henrik N. Poulsen, and Palle Jeppesen, Member, IEEE, "All-Optical Wavelength Conversion of Short Pulses and NRZ Signals Based on a Nonlinear Optical Loop Mirror", *J. Lightwave Technol*., vol. 18, no. 7, pp. 1007–1017, 2000

[11] Jianjun Yu, Xueyan Zheng, Christophe Peucheret, Anders T. Clausen, Henrik N. Poulsen, and Palle Jeppesen, Member, IEEE, "40-Gb/s All-Optical Wavelength Conversion Based on a Nonlinear Optical Loop Mirror", *J. Lightwave Technol*., vol. 18, no. 7, pp. 1001–1006, 2000

[12] Nan Chi, Lin Xu, Kim S. Berg, Torger Tokle and Palle Jeppesen, "All-optical Wavelength Conversion and Multi-channel 2R Regeneration Based on Highly Nonlinear Dispersion-Imbalanced Loop Mirror", *IEEE Photonics Technology Letters*, vol. 14, no. 11, pp. 1581-1583, 2002

[13] C. Schubert, R. Ludwig, S. Watanabe, F. Futami, C. Shmidt, J. Berger, C. Boerner, S. Ferber, H. G. Weber, "160 Gbit/s wavelength conversion with 3R-regenerating capacity", *Electro. Lett*., vol. 38, no. 16, pp. 903-904, 2002

[14] T. Durhuus, et al, "All-optical wavelength conversion by semiconductor optical amplifier", *J. Lightwave Technol*., vol. 14, no. 6, pp. 942–954, 1996

[15] M. Asghari, et al, "Wavelength conversion using semiconductor optical amplifier", *J. Lightwave Technol*., vol. 15, no. 7, pp. 1181-1190, 1997

[16] J. M. Wiesenfeld, B. Glance, J. S. Perino, and A. H. Gnauck, "Wavelength conversion at 10 Gbit/s using a semiconductor optical amplifier," *IEEE Photon. Technol. Lett.*, vol. 5, pp. 1300–1303, Nov. 1993

[17] C. Joergensen, S. L. Danielsen, and M. Vaa et al., "40 Gbit/s all-optical wavelength conversion by semiconductor optical amplifiers," *Electron. Lett*., vol. 32, no. 4, pp. 367–368, 1996

[18] S. Y. Set, R. Girardi, and E. Riccardi, "40 Gbit/s field transmission over standard fiber using midspan spectral inversion for dispersion compensation," *Electron. Lett.*, vol. 35, no. 7, pp. 581–582, 1997

[19] M. F. C. Stephens, D. Nesset, R. V. Penty, I. H. White, and M. J. Fice, "Wavelength conversion at 40 Gbit/s via four wave mixing in semiconductor optical amplifier with integrated pump laser," *Electron. Lett*., vol. 35, no. 3, pp. 420–421, 1999

[20] A. E. Kelly, D. D. Marcenac, and D. Nesset, "40 Gbit/s wavelength conversion over 24.6 nm using FWM in a semiconductor optical amplifier with an optimized MQW active region," *Electron. Lett*., vol. 33, no. 25, pp. 2123–2124, 1997

[21] B. Mikkelsen, M. Vaa, H. N. Poulsen, S. L. Danielsen, C. Joergensen, A. Kloch, A. P. B. Hansen, K. E. Stubkjaer, K. Wunstel, K. Daub, E. Lach, G. Laube,W. Idler,M. Schilling, and S. Bouchoule, "40 Gbit/s alloptical wavelength converter and RZ-NRZ format adapter realized by monolithic integrated active Michelson interferometer," *Electron. Lett*., vol. 33, no. 2, pp. 133–134, 1997

[22] T. Fjelde, D. Wolfson, P. B. Hansen, A. Kloch, C. Janz, A. Coquelin, I. Guillemot, F. Gaborit, F. Poingt, B. Dagens, and M. Renaud, "20 Gbit/s optical wavelength converison in all-active Mach-Zehnder interferometer," *Electron. Lett*., vol. 35, no. 11, pp. 913–914, 1999

[23] B. Mikkelsen, et al, "All-optical wavelength converter scheme for high speed RZ signal formats", *Electron. Lett*., vol. 33, no. 25, pp. 2137–2139, 1997

[24] S. Nakamura, Y. Ueno, K. Tajima, "168-Gb/s All-Optical Wavelength Conversion With a Symmetric-Mach–Zehnder-Type Switch", *IEEE Photon. Technol. Lett*., vol. 13, no. 10, pp. 1091–1093, 2001

[25] A. E. Kelly, et al, "80Gbit/s all-optical regenerative wavelength conversion using semiconductor optical amplifier based interferometer", *Electron. Lett*., vol. 35, no. 17, pp. 1477–1478, 1999

[26] T. Yamanoto, et al, "Ultrafast nonlinear optical loop mirror for demultiplexing 640 Gbit/s TDM signals", *Electron. Lett*., vol. 34, no. 10, pp. 1013-1014,1998

[27] H. Sotobayashi, C. Sawaguchi, Y. Koyamada, and W. Chujo, "Ultrafast walk-off-free nonlinear optical loop mirror by a simplified configuration for 320-Gbit/s

time-division multiplexing signal demultiplexing", *Optics Letters*, vol. 27, no. 17, pp. 1555-1557, 2002

[28] B. E. Olsson and D. J. Blumenthal, "All-Optical Demultiplexing Using Fibre Cross-Phase Modulation (XPM) and Optical Filtering", *IEEE Photon. Technol. Lett.*, vol. 13, no. 8, pp. 875-877, 2001

[29] J. Li, B. Olsson, M. Karlsson, P. Andrekson, "OTDM Demultiplexer Based on XPM-Induced Wavelength Shifting in Highly Nonlinear Fibre", *in Proceedings of OFC'03*, paper TuH6, pp. 198-200, 2003

[30] I. Tomkos, Student Member, IEEE, I. Zacharopoulos, D. Syvridis, R. Calvani, F. Cisternino, and E. Riccardi, "All-Optical Demultiplexing/Shifting of 40-Gb/s OTDM Optical Signal Using Dual-Pump Wave Mixing in Bulk Semiconductor Optical Amplifier", *IEEE Photon. Technol. Lett.*, vol. 11, no. 11, pp. 1464-1466, 1999

[31] T. Morioka, et al, "Polarization-Independent all-optical demultiplexing up to 200 Gbit/s using four-wave-mixing in a semiconductor optical amplifier", *Electron. Lett.*, vol. 32, no. 9, pp. 840-842, 1996

[32] R. Hess, et al, "All-Optical Demultiplexing of 80 to 10 Gb/s Signals with Monolithic Integrated High-Performance Mach–Zehnder Interferometer", *IEEE Photon. Technol. Lett.*, vol. 10, no. 1, pp. 165-167, 1998

[33] Tetsuya Miyazaki and Fumito Kubota, Member IEEE, "Simultaneous Demultiplexing and Clock Recovery for 160-Gb/s OTDM Signal Using a Symmetric Mach–Zehnder Switch in Electrooptic Feedback Loop*", IEEE Photon. Technol. Lett.*, vol. 15, no. 7, pp. 1008-1010, 2003

[34] S. Nakamura, Y. Ueno, and K. Tajima, "Error-free all-optical demultiplexing at 336 Gb/s with a hybrid-integrated symmetric-Mach-Zehnder switch", *in Proceedings of OFC'02*, paper PD3, 2002

[35] C. Schubert, J. Berger, U. Feiste, R. Ludwig, C. Schmidt, and H. G. Weber, "160-Gb/s Polarization Insensitive All-Optical Demultiplexing Using a Gain-Transparent Ultrafast Nonlinear Interferometer (GT-UNI)", *IEEE Photon. Technol. Lett.*, vol. 13, no. 11, pp. 1000-1002, 2001

[36] C. Guilemot, et al, "Transparent optical packet switching: The european ACTS KEOPS project approach", *J. Lightwave Technol.*, vol. 16, pp. 2117-2134, 1998

[37] B. E. Olsson, et al, "Wavelength routing of 40 Gb/s packets with 2.5 Gb/s header erasure/rewriting using all-fiber wavelength converter", *Electron. Lett.*, vol. 31, no. 4, pp. 345-347, 2000

[38] P. Gambini, et al, "Transparent optical pachet switching: Network architecture and demonstrators in the KEOPS project", *IEEE J. Select. Areas Commun.*, vol. 16, pp. 1245-1259, 1998

[39] A Budman, et al, "Multigigabit optical packet switch for self-routing networks with subcarrier addressing", *in Proceedings of OFC'92*, pp. 90-91, 1992

[40] D. J. Blumenthal, P. R. Prucnal and J. R. Sauer, "Photonic packet switches: Architectures and experimental implementations", *in Proceedings of IEEE*, vol. 82, no. 11, pp. 1650-1667, 1994

[41] Nan Chi, Jianfeng Zhang, and Palle Jeppesen, "All-optical sub-carrier labelling based on the carrier suppression of the payload," *IEEE Photon. Technol. Lett.*, vol. 15, no. 5, pp. 781-783, 2003

[42] T. Koonen, et al, "Optical packet routing in IP-over-WDM networks deploying two-level optical labelling*", in Proceedings of ECOC'01*, paper Th.L.2.1, pp. 608-609, 2001

[43] N. Chi, B. Carlsson, J. Zhang, P. V. Holm-Nielsen, C. Peucheret, P. Jeppesen, "Transmission Performance of All-optically labelled Packets using ASK/DPSK Orthogonal Modulation," *in Proceedings of LEOS 2002*, paper MF3, vol.1, pp.51-53, 2002

[44] Y. Furushima, et al., "1560 to 1610 –nm wavelength EA-modulator integrated DFB-LDs for extended-band 2.5-Gb/s/ch and 10-Gb/s/ch WDM systems", *in Proceedings of OFC'99*, paper WH2, pp. 131-133, 1999

[45] H. Kawanishi, et al., "Over-40-GHz modulation bandwidth of EAM-integrated DFB laser modules", *in Proceedings of OFC'01*, paper MJ3, 2001

[46] H. Feng, et al., "40 Gb/s electro-absorption modulator integrated DFB laser with optimized design", *in Proceedings of OFC'02*, paper WV4, pp. 340-341, 2002

[47] H. Kawanishi, et al., "1.3 μm EAM-integrated DFB lasers for 40 Gb/s very-short-reach application", *in Proceedings of OFC'03*, paper TuP4, pp. 270-271, 2003

[48] H. Takeuchi, et al., "High-speed electroabsorption modulators with travelling-wave electrodes", *in Proceedings of OFC'02*, paper WV1, pp. 336-337, 2002

[49] L. J. P. Ketelsen, et al., "Electro-absorption modulated 1.55 μm wavelength selectable DFB array using hybrid integration", *in Proceedings of OFC'99*, paper PD40, 1999

[50] K. Kudo, et al., "1.55- μm wavelength-selectable microarray DFB-LD's with integrated MMI combiner, SOA, and EA-modulator", *in Proceedings of OFC'00*, paper TuL5, 2000

[51] J. R. Burie, et al. "50 Gb/s capability of a new zero loss integrated SOA/EA modulator", *in Proceedings of ECOC'00*, pp. 43-44, 2000

[52] A. Ougazzaden, et al., "40 Gb/s tandem electro-absorption modulator", *in Proceedings of OFC'01*, paper PD14, 2001

[53] A. Ramdane, et al., "Identical active layer monolithic integration of DBR laser-EA modulator with quasi constant chirp over 7.4 nm", *in Proceedings of ECOC'99*, vol. II, pp. 250-251, 1999

[54] B. Mason, et al., "Characteristics of sampled grating DBR lasers with intergrated semiconductor optical amplifiers and electroabsorption modulators", *in Proceedings of OFC'00*, paper TuL6, 2000

[55] Y. A. Akulova, et al., "Widely-Tunable electroabsorption modulated sampled grating DBR laser integrated with semiconductor optical amplifier", *in Proceedings of OFC'02*, paper ThV1, pp. 536-537, 2002

[56] M. Kato, et al., "Enlargement of polarization-insensitive operation wavelength range in MQW-EA modulator by tensile strained pre-biased quantum well", *in Proceedings of ECOC'99*, vol. II, pp. 72-73, 1999

[57] K. Tsuzuki, et al., "Four-channel polarization independent EA modulator array with an IPF carrier operating at 10 Gbit/s", *in Proceedings of ECOC'02*, vol. II, pp. 80-81, 1999

[58] K. Prosyk, et al., "Low loss, low chirp, low voltage, polarization independent 40 Gb/s bulk electro-absorption modulator module", *in Proceedings of OFC'03*, paper TuP3, 2003
[59] N. Edagawa, et al., "Novel wavelength converter using electroabsorption modulator", *IEICE Trans. Electron*., vol. E81-C, no. 8, pp. 1251-1257, 1998
[60] L. K. Oxenløwe, et al., "Wavelength conversion in an electroabsorption modulator", *in Proceedings of ECOC'00*, paper 9.4.4, 2000
[61] H. Tanaka, et al., "60Gbit/s WDM-OTDM transmultiplexing using an electro-absorption modulator", *in Proceedings of OFC'01*, paper ME4, 2001
[62] K. Nishimura, et al., "Wavelength conversion with no pattern effect at 40 Gbps using an electroabsorption waveguide as a phase modulator", *in Proceedings of OFC'01*, paper WK5, 2001
[63] K. Nishimura, et al., "Delayed-interferometric wavelength converter using electroabsorption modulator with optimized bandgap wavelength", *in Proceedings of ECOC'02*, paper 2.3.7, 2002
[64] K. Nishimura, et al., "80 Gb/s wavelength conversion by MQW electroabsorption modulator with delayed-interferometer", *in Proceedings of OFC'03*, paper TuP5, 2003
[65] K. Shimomura, et al., "A simple optical demultiplexing method using saturable absorption of EA modulator", *in Proceedings of ECOC'00*, pp. 305-307, 2000
[66] V. Kaman, et al., "Electroabsorption modulator as a compact OTDM demultiplexing receiver", *in Proceedings of ECOC'00*, pp. 309-310, 2000
[67] K. Schuh, et al., "4x160 Gbit/s DWDM/OTDM transmission over 3x80km TeraLight reverse Teralight fibre", *in Proceedings of ECOC'02*, paper 2.1.2, 2002
[68] M. Schmidt, et al., "8x160 Gbit/s (1.28 Tbit/s) DWDM transmission with 0.53 bit/s/Hz spectral efficiency using single EA-modulator based RZ pulse source and demux", *in Proceedings of ECOC'03*, paper 3.6.5, 2003
[69] B. Mikkelsen, et al., "160 Gbit/s single-channel transmission over 300 km nonzero-dispersion fiber with semiconductor based transmitter and demultiplexer", *in Proceedings of ECOC'99*, paper PD2-3, 1999
[70] H. Murai, et al., "Single channel 160 Gbit/s carrier-suppressed RZ transmitter over 640 km with EA modulator based OTDM module", *in Proceedings of ECOC'03*, paper 3.6.4, 2003
[71] H. Chou, et al., "160Gb/s to 10Gb/s OTDM demultiplexing using a travelling-wave electroabsorption modulator", *in Proceedings of OFC'03*, paper ThX2, 2003
[72] S. Kodama, et al., "160-Gbit/s error-free demultiplexing operation by a monolithic PD-EAM optical gate", *in Proceedings of OFC'02*, paper TuU2, 2002
[73] S. Kodama, et al., "320-Gbit/s error-free demultiplexing operation of a monolithic PD-EAM optical gate", *in Proceedings of OFC'03*, paper ThX5, 2003
[74] L. K. Oxenløwe, et al., "Characterization of a MQW electroabsorption modulator as an all-optical demultiplexer", *in Proceedings of LEOS'01*, paper ME2, 2001
[75] L. K. Oxenløwe, et al., "All-optical demultiplexing and wavelength conversion in an electroabsorption modulator", *in Proceedings of ECOC'01*, paper Th.B.2.5, 2001

[76] E. Hilliger, et al., “EAM with Improved switching performance by self cascading”, *in Proceedings of OFC’03*, paper TuP2, 2003

[77] E. S. Awad, et al., “Characterization of four-wave mixing in electroabsorption modulator and its application to high-speed optical demultiplexing”, *in Proceedings of OFC’04*, paper MF46, 2004

[78] E. S. Awad, et al., “Simultaneous optical demultiplexing and clock recovery using four-wave mixing and timing extraction inside a single electroabsorption modulator”, *in Proceedings of OFC’04*, paper ThN5, 2004

[79] T. Miyazaki, et al., “Novel optical-regenerator using electroabsorption modulators”, *in Proceedings of OFC’99*, paper WM53, 1999

[80] T. Otani, et al., “20 Gbit/s optical regenerator using electroabsorption modulators for all-optical network application”, *in Proceedings of OFC’99*, vol. I, pp. 250-251, 1999

[81] T. Otani, et al., “40 Gbit/s signal transmission using optical 3R regenerator based on electroabsorption modulators”, *in Proceedings of OFC’03*, paper ThP3, 2003

[82] P. S. Cho, et al., “All-optical 2R regeneration of 10 Gb/s RZ data transmitted over 30,000 km in a dispersion-managed system using an electroabsorption modulator”, *in Proceedings of OFC’00*, paper WM22, 2000

[83] E. S. Awad, P. S. Cho, C. Richardson, N. Moulton, J. Goldhar, “Optical 3R regeneration with all-optical timing extraction and simultaneous wavelength conversion using a single Electro-Absorption Modulator”, *in Proceedings of ECOC’02*, paper 6.3.2, 2002

[84] M. D. Pelusi, Y. Matsui, and A. Suzuki, “Femtosecond optical pulse generation from an electroabsorption modulator with repetition rate and wavelength tuning”, *in Proceedings of ECOC’99*, vol. II, pp. 26-27, 1999

[85] H. F. Chou, et al., “40 GHz optical pulse generation using travelling-wave electroabsorption modulator”, *in Proceedings of OFC’02*, paper WV2, 2002

[86] L. K. Oxenløwe, et al., “A novel 160 Gb/s receiver configuration including a glass crystal pulsed laser, photonic crystal fibre and a simple dynamic clock recovery scheme”, *in Proceedings of ECOC’03*, paper Th2.5.3, 2003

[87] J. C. Cartledge, and G. S. Burley, "The effect of laser chirping on lightwave system performance", *J. Lightwave Technol*., vol. 7, no. 3, pp. 568-573, 1989

[88] R. A. Linke, "Modulation induced transient chirping in single frequency lasers", *J. Quantum Electron.,* vol. QE-21, no. 6, pp. 593-597, 1985

[89] Ioannis Tomkos, Robert Hesse, Rich Vodhanel, and Aleksandra Boskovic, “Metro Network Utilizing 10-Gb/s Directly Modulated Lasers and Negative Dispersion Fiber”, *IEEE Photon. Technol. Lett*., vol. 14, no. 3, pp. 408-410, 2002

[90] A. Filios, et al., “16 channel, 10 Gb/s DWDM transmission of directly modulated lasers with 100 GHz channel spacing over 100 km of negative dispersion fiber”, *in Proceedings of LEOS’01*, paper. ThK3, 2001

[91] P. Paoletti, et al., “10 Gbit/s ultra-low chirp 1.55 μm directly modulated hybrid fiber grating – semiconductor laser source”, *in Proceedings of ECOC’97*, pp. 107-110, 1997

[92] F. N. Timofeev, et al., “Low-chirp, 2.5 Gbit/s directly modulated fiber grating laser for WDM networks”, *in Proceedings of OFC’97*, paper ThM1, 1997

[93] S. Mohrdiek, H. Burkhard and H. Walter, "Chirp reduction of directly modulated semiconductor lasers at 10 Gb/s by strong CW light injection", *J. Lightwave Technol*., vol. 12, no. 3, pp. 418-442, 1994
[94] J. Kondo, et al., "Low-drive-voltage 40 Gb/s modulator on X-cut LiNbO3 wafer", *in Proceedings of ECOC'01*, paper We.F.3.3, 2001
[95] M. Sugiyama, et al., "Drive-less 40 Gb/s LiNbO3 modulator with sub-1 V drive voltage", *in Proceedings of OFC'02*, paper FB6-1, 2002
[96] L. A. Coldren, and S. W. Corzine, *Diode Lasers and Photonic Integrated Circuits*, John Willey & Sons, New York, 1995
[97] Koichi Wakita, *Semiconductor optical modulators*, Kluwer Academic Publishers
[98] T. H. Wood, " Multiple Quantum Well(MQW) Waveguide Modulators ", *J. Lightwave Technol.*, vol. 6, pp. 743-757, 1988
[99] W. Franz, *Z. Naturforsch*. 13a, 484, 1958
[100] L. V. Keldysh, *Zh. Eksp. Teor. Fiz*. 34, 1138, 1958 [Sov. Phys.- JETP 7, 788, 1958]
[101] J. D. Dow and D. Redfield, "Toward a unified theory of Urbach's rule and exponential absorption edges", *Phys. Rev. B*, vol. 5, no. 2, pp. 594-610, 1972
[102] K. Tharmalingam, "Optical absorption in the Presence of a uniform field", *Phys. Rev.*, vol. 130, no. 6, pp. 2204-2206, 1963
[103] D. A. B. Miller, et al., "Relation between electroabsorption in bulk semiconductors and in quantum wells: The quantum-confined Franz-Keldysh effect", *Phys. Rev. B*, vol. 33, pp. 6976-6982, 1986
[104] J. D. Dow and D. Redfield, "Electroabsorption in semiconductors: The excitonic absorption edge", *Phys. Rev. B*, vol. 1, no. 8, pp. 3358-3371, 1970
[105] T. H. Wood, C. A. Burrus, D. A. B. Miller, D. S. Chemla, T. C. Damen, A. C. Gossard, and W. Wiegmann, "High-speed optical modulation with GaAs/GaAlAs quantum wells in a p-I-n diode structure", *Appl. Phys. Lett*., vol. 44, no. 1, pp. 16-18, 1984
[106] D. A. B. Miller, et al., "Band-edge electroabsorption in quantum well structures: The Quantum-confined stark effect", *Phys. Rev. Lett*., vol. 53, pp. 2173-2176, 1984
[107] D. A. B. Miller, et al., "Electric field dependence of optical absorption near the band gap of quantum-well structures", *Phys. Rev. B*, vol. 32, pp. 1043-1060, 1985
[108] F. Koyama, and K. Iga, "Frequency chirping in external modulators", *J. Lightwave Technol.*, vol. 6, no. 1, pp. 87-92, 1988
[109] J. S. Weiner, D. A. B. Miller, and D. S. Chemla, "Quadratic electro-optic effect due to the quantum-confined Stark effect in quantum wells", *Appl. Phys. Lett*., vol. 50, no. 13, pp. 842-844, 1987
[110] J. E. Zucker, T. L. Hendrickson, and C. A. Burrus, "Electro-optic phase modulation in GaAs/AlGaAs quantum well waveguides", *Appl. Phys. Lett*., vol. 52, no. 12, pp. 945-947, 1988
[111] M. Suzuki, Y. Noda, Y. Kushiro, and S. Akiba, "Dynamic spectral width of an InGaAsP/InP electroabsorption light modulator under high-frequency large-signal modulation", *Electron Lett*., vol. 22, pp. 312-313, 1986

[112] C. Harder, K. Vahala, A. Yariv, "Measurement of the linewidth enhancement factor a of semiconductor lasers", *Appl. Phys. Lett*., vol. 42, no. 4, pp. 328-330, 1983

[113] F. Koyoma and Y. Suematsu, "Analysis of Dynamic spectral width of dynamic-single-mode (DSM) lasers and related transmission bandwidth of single-mode fibers", *IEEE J. Quantum Electron*., vol. QE-21, pp. 292-297, 1985

[114] F. Devaux, Y. Sorel, J. F. Kerdiles, "Simple Measurement of Fiber Dispersion and of Chirp Parameter of Intensity Modulated Light Emitter", *J. Lightwave Technol*., vol. 11, pp. 1937-1940, 1993

[115] D. D. Curtis, and E. E. Ames, "Optical test set for microwave fiber-optic network analysis", *IEEE Transactions On Microwave Theory and Techniques*, vol. 38, no. 5, pp. 552-559, 1990

[116] F. Romstad, D. Birkedal, J. Mørk, and J. M. Hvam, "Measurement of the amplitude and phase transfer functions of an optical modulator using a heterodyne technique", *in Proceedings of LEOS'01*, paper ME1, 2001

[117] F. Dorgeuille, and F. Devaux, "On the transmission performances and the chirp parameter of a multiple-quantum-well electroabsorption modulator", *IEEE J. Quantum Electron*., vol. 30, no. 11, pp. 2565-2572, 1994

[118] Govind P. Agrawal, *Nonlinear fiber optics*, Third Edition, Academic Press, 2001

[119] D. S. Chemla and D. A. B. Miller, "Room-temperature excitonic nonlinear-optical effects in semiconductor quantum-well structures", *J. Opt. Soc. Amer. B*, vol. 2, no. 7, pp. 1155-1173, 1988

[120] H. Haug and S. Schmitt-Rink, "Basic mechanisms of the optical nonlinearities of semiconductors near the band edge", *J. Opt. Soc. Amer. B*, vol. 2, no. 7, pp. 1135-1142, 1988

[121] P. J. Bradley, C. Rigo, and A. Stano, "Carrier induced transient electric fields in a p-I-n InP-InGaAs multiple-quantum-well modulator", *IEEE J. Quantum Electron*., vol. 32, no. 1, pp. 43-52, 1996

[122] T. H. Wood, J. Z. Pastalan, C. A. Burrus, Jr., B. C. Johnson, B. I. Miller, J. L. deMiguel, U. Koren, M. G. Young, "Electric field screening by photogenerated holes in multiple quantum wells: A new mechanism for absorption saturation", *Appl. Phys. Lett*., vol. 57, no. 11, pp. 1081-1083, 1990

[123] R. Sauer, K. Thonke, and W. T. Tsang, "Photoinduced space-charge buildup by asymmetric electron and hole tunnelling in coupled quantum wells", *Phys. Rev. Lett*., vol. 61, no. 5, pp. 609-612, 1988

[124] M. Suzuki, H. Tanaka, S. Akiba, "Effect of hole pile-up at heterointerface on modulation voltage in GaInAsP electroabsorption modulators", *Electro. Lett*., vol. 25, no. 2, pp. 88-89, 1989

[125] M. Asada and Y. Suematsu, "Density matrix theory of semiconductor lasers with relaxation broadening model-gain and gain-suppression in semiconductor lasers", *IEEE J. Quantum Electron*., vol. QE-21, pp. 434-441, 1985

[126] N. Ogasawara and R. Ito, "Longitudinal mode competition and asymmetric gain saturation in semiconductor injection lasers. II. Theory", *Jap. J. Appl. Phys*., vol. 27, pp. 615-626, 1988

[127] A. Uskov, J. Mørk and J. Mark, "Wave mixing in semiconductor laser amplifiers due to carrier heating and spectral-hole burning", *IEEE J. Quantum Electron*., vol. 30, pp. 1769-1781, 1994

[128] W. W. Chow, S. W. Koch and M. Sargent, *Semiconductor-Laser Physics*, Berlin: Spring-Verlag, 1994

[129] H. Hang and S. W. Koch, *Quantum theory of the optical and electronic properties of semiconductors*, Singapore: World Scientific, 1990

[130] C. Ell, H. Huang and S. W. Koch, "Many-body effects in gain and refractive-index spectra of bulk and quantum-well semiconductor lasers", *Opt. Lett*., vol. 14, pp. 356-358, 1989

[131] K. Henneberger, F. Herzel, S. W. Koch, R. Binder, A.E. Paul and D. Scott, "Spectral holeburning and gain saturation in short-cavity semiconductor lasers", *Phy. Rev. A*, vol. 45, pp. 1853-1859, 1992

[132] J. Mørk and J. Mark, "Time-resolved spectroscopy of semiconductor laser devices: Experiments and modelling", *in Proceedings of SPIE*, vol. 2399, pp. 146-159, 1995

[133] J. Feldmann, et al., "Fast escape of photocreated carriers out of shallow quantum wells", *Appl. Phys. Lett*., vol. 59, no. 1, pp. 66-68, 1991

[134] S. Højfeldt, S. Bischoff and J. Mørk, "All-Optical wavelength conversion and signal regeneration using an electroabsorption modulator", *J. Lightwave Technol*., vol. 18, no. 8, pp. 1121-1127, 2000

[135] S. Bischoff, *Modelling colliding-pulse mode-locked semiconductor lasers*, ph.d theis, Research Center COM, Technical University of Denmark,1997

[136] R. Y. F. Yip, et al., "Band alignment engineering for high speed, low drive field quantum-confined Stark effect devices", *J. Appl. Phys.*, vol. 83, no. 3, pp. 1758-1769, 1998

[137] L. K. Oxenløwe, *Optical signal processing with semiconductor components*, Ph.D Thesis, Research Center COM, Technical University of Denmark, 2002

[138] A. B. Carlson, P. B. Crilly, and J. C. Rutledge, *Communication Systems An Introduction to Signals and Noise in Electrical Communication*, fourth edition, McGraw-Hill, 2002

[139] B. Mukherjee, *Optical Communication Networks*, New York: McGraw-Hill, 1997.

[140] S. L. Danielsen, P. B. Hansen, and K. E. Stubkjaer, "Wavelength conversion in optical packet switching", *J. Lightwave Technol*. vol. 16, no. 12, pp. 2095-2108, 1998

[141] J. M. Gabriagues and J. B. Jacob, "Exploitation of the wavelength domain for photonic switching in IBCN," *in Proceedings of ECOC*'91, vol. 2, pp. 59–66, 1991

[142] S. L. Danielsen, et al., "10 Gb/s operation of a multiple wavelength buffer architecture employing a monolithically integrated all-optical inteferometric Michelson wavelength converter", *IEEE Photon. Technol. Lett*., vol. 8, pp. 434-436, 1996

[143] R. A. Barry, and P. A. Humblet, "Models of blocking probability in all-optical networks with and without wavelength changers", *IEEE J. Select. Areas Commun*., vol. 14, pp. 858-867, 1996

[144] S. J. B. Yoo, "Wavelength conversion technologies for WDM network applications", *J. Lightwave Technol*. vol. 14, pp. 955-966, 1996

[145] J. M. H. Elmirghani, and H. T. Mouftah, "All-optical wavelength conversion: Technologies and applications in DWDM networks", *IEEE Commun. Mag*., vol. 38, no. 3, pp. 86-92, 2000

[146] S. L. Danielsen, et al., "WDM packet switch architectures and analysis of the influence of tuneable wavelength converters on the performance", *J. Lightwave Technol*. vol. 15, no. 2, pp. 219-227, 1997

[147] A. Bononi, et al., "Analysis of Hot-Potato optical networks with wavelength conversion", *J. Lightwave Technol*. vol. 17, no. 4, pp. 525-534, 1999

[148] T. Sakamoto, F. Futami, K. Kikuchi, S. Takeda, Y. Sugaya, S. Watanabe, "All-optical wavelength conversion of 500-fs pulse trains by using a nonlinear-optical loop mirror composed of a highly nonlinear DSF", *IEEE Photon. Technol. Lett*., vol. 13, no. 5, pp. 502-504, 2001

[149] M. Hayashi, H. Tanaka, K. Ohara, T. Otani, M. Suzuki, "OTDM Transmitter Using WDM-TDM Conversion With an Electroabsorption Wavelength Converter", *J. Lightwave Technol*., vol. 20, pp. 236-242, 2002

[150] L. Xu, L.K. Oxenløwe, N. Chi, F. P. Romstad, K. Yvind, J. Mørk, P. Jeppesen, K. Hoppe and J. Hanberg, "Bandwidth and chirp characterisation of wavelength conversion based on electroabsorption modulators", *in Proceedings of ECOC'02*, paper P1.26, 2002

[151] L. Xu, L.K. Oxenløwe, N. Chi, J. Mørk, P. Jeppesen, K. Hoppe and J. Hanberg, "Experimental characterisation of wavelength conversion at 40Gb/s based on electroabsorption modulators", *in Proceedings of IEEE LEOS'02*, paper MM3, 2002

[152] L. Xu, N. Chi, K. Yvind, L.J. Christiansen, L.K. Oxenløwe, J. Mørk, P. Jeppesen and J. Hanberg, "8×40 Gb/s RZ all-optical broadcasting utilizing an electroabsorption modulator", *in Proceedings of OFC'04*, paper MF71, 2004

[153] L. Xu, N. Chi, K. Yvind, L.J. Christiansen, L.K. Oxenløwe, J. Mørk, P. Jeppesen and J. Hanberg, "7 × 40 Gb/s base-rate RZ all-optical broadcasting utilizing an electroabsorption modulator", *Optics Express*, vol. 12, no. 3, pp. 416-420, 2004

[154] Agrawal, G. P., *Fiber-Optic Communication Systems*, Third Edition, John Wiley & Sons, New York, 2002

[155] N. A. Olsson, "Lightwave systems with optical amplifiers", *J. Lightwave Technol*., vol. 7, no.7, pp.1071-1082, 1989

[156] P. Őhlén, B. E. Olsson and D. J. Blumenthal, "Wavelength dependence and power requirements of a wavelength converted based on XPM in a dispersion-shifted optical filber", *IEEE Photon. Technol. Lett*., vol. 12, no. 5, pp. 522-524, 2000

[157] B. E. Olsson, P. Őhlén, L. Rau, and D. J. Blumenthal, "A simple and robust 40-Gb/s wavelength converter using fiber cross-phase modulation and optical filtering", *IEEE Photon. Technol. Lett*., vol. 12, no. 7, pp. 846-848, 2000

[158] P. Őhlén, B. E. Olsson and D. J. Blumenthal, "All-optical header erasure and penalty-free rewriting in a fiber-based high-speed wavelength converter", *IEEE Photon. Technol. Lett*., vol. 12, no. 6, pp. 663-665, 2000

[159] J. S. Perino, J. M. Wiesenfield and B. Glance, "Fibre transmission of 10 Gb/s signals following wavelength conversion using a travelling-wave semiconductor optical amplifier", *Electron. Lett*., vol. 30, no. 3, pp. 256–257, 1994

[160] L. Xu, N. Chi, L.J. Christiansen, K. Yvind, L.K. Oxenløwe, J. Mørk and P. Jeppesen, "160 to 10 Gb/s all-optical demultiplexing using a single electroabsorption modulator", *in Proceedings of ECOC*'04, paper We1.5.3, 2004

[161] K. R. Tamura, M. Nakazawa, "A Polarization-Maintaining Pedestal-Free femtosecond Pulse Compressor Incorporating an Ultrafast Dispersion-Imbalanced Nonlinear Optical Loop Mirror," *IEEE photon. Technol. Lett.*, vol.13, no.5, pp.526-528, 2001

[162] Y. Khrushchev, "Picosecond pulse source for OTDM/WDM applications based on arrayed waveguide grating," *in Proceedings of OFC*'99, ThT5, pp. 296-298, 1999

[163] I.Y. Khrushchev, "OTDM applications of dispersion-imbalanced fibre loop mirror," *Electron. Lett.*, vol.35, no.14 , pp. 1183-1185,1999

[164] W. S. Wong, "In-band amplified spontaneous emission noise filtering with a dispersion -imbalanced non-linear loop mirror," *J. Lightwave Technol.*, vol.16, no.10 , pp. 1768-1772,1998

[165] W. S. Wong, "Self-switching of optical pulses in dispersion-imbalanced non-linear loop mirrors," *Opt. Lett.*, vol.22, no.15, pp. 1150-1152, 1997

[166] N. Chi, S. Chen, L. Xu, j. Qi, Y. Qiao, Y. Zheng, "A new scheme of cross-gain modulation wavelength converter with good perfermance on extinction ratio," *Optics Comm.*, vol. 189/4-6, pp.235-239, 2001

[167] N. Chi, B. Carlsson, and P. Jeppesen, "2R Regeneration Based on Dispersion-Imbalanced Loop Mirror and Its Applications in WDM systems," *J. Lightwave Technol.*, vol.20, no.10, pp.1809-1818, 2002

[168] M. Matsumoto, T. Ohishi, "Dispersion-imbalanced nonlinear optical loop mirror with lumped dispersive elements," *Electron. Lett.*, vol.34, no.11, pp. 1140-1141,1998

[169] J. Mørk, F. Öhman and S. Bischoff, "Analytical expression for the bit-error-rate of cascaded all-optical regenerators", *IEEE Photon. Technol. Lett.*, vol. 15, no. 10, pp. 1479-1481, 2003

[170] P. Őhlen, and E. Berglind, "Noise accumulation and BER estimates in concatenated nonlinear optoelectronic repeaters", *IEEE Photon. Technol. Lett.*, vol. 9, no. 7, pp. 1011-1013, 1997

[171] F. Őhman, S. Bischoff, B. Tromborg and J. Mørk, "Noise and regeneration in semiconductor waveguides with saturable gain and absorption", *IEEE J. Quantum Electron.*, vol. 40, no. 3, pp. 245-255, 2004

[172] D. J. Blumental, B. Olsson, G. Rossi, T. E. Dimmick, L. Rau, M. Masanovic, O. Lavrova, R. Doshi, O. Jerphagnon, J. E. Bowers, V. Kaman, L. A. Coldren, J.

Barton, “All-optical label swapping networks and technologies”, *J. Lightwave Technol.*, vol. 18, no. 12, pp. 2058-2075, 2000

[173] N. Ghani, “Lambda-labeling: a framework for IP-over-WDM using MPLS”, *Optical Networks Magazine*, v1, pp. 45-58, 2000

[174] A. Viswanathan, N. Feldman, Z. Wang and R. Callon, “Evolution of multiprotocol label switching”, *IEEE Commun. Mag.*, vol. 36, pp. 165-173, 1998

[175] L. Xu, N. Chi, L.K. Oxenløwe, K. Yvind, J. Mørk, P. Jeppesen and J. Hanberg, “Optical label encoding using electroabsorption modulators and investigation of chirp properties”, *J. Lightwave Technol.*, vol. 21, no. 8, pp. 1763-1769, 2003

[176] N. Chi, B. Carlsson, P. V. Holm-Nielsen, C. Peucheret, P. Jeppesen, “Dispersion management for two-level optically labeled signals in IP-over-WDM net-works,” *in proceeding of ECOC*’02, paper 5.5.1, vol. 2, 2002

[177] N. Chi, L. Xu, L. Chritiansen, K. Yvind, J. Zhang, P. Holm-Nielsen, C. Peucheret, C. Zhang, P. Jeppesen, “Optical label swapping and packet transmission based on ASK/DPSK orthogonal modulation format in IP-over-WDM networks”, *in Proceedings of OFC*’03, paper FS2, 2003.

[178] N. Chi, J. Zhang, P. V. Holm-Nielsen, C. Peucheret, and P. Jeppesen, “Transmission and Transparent Wavelength Conversion of an Optically Labelled Signal Using ASK/DPSK Orthogonal Modulation,” *IEEE Photon. Technol. Lett.*, vol. 15, no. 5, pp. 760-762, 2003.

[179] Nan Chi, Birger Carlsson, Jianfeng Zhang, Pablo V. Holm-Nielsen, Christophe Peucheret, Palle Jeppesen, “Transmission properties for two-level optically labeled sig-nals using ASK/DPSK orthogonal modulation in IP-over-WDM networks”, *J. Optical networking*, vol. 2, no. 2, pp.46-54, 2003

[180] N. Chi, J. Zhang, P. V. Holm-Nielsen, L. Xu, I. T. Monroy, C. Peucheret, K. Yvind, L. J. Christiansen and P. Jeppesen, "Experimental demonstration of cascaded transmission and all-optical label swapping of orthogonal IM/FSK labelled signal", *Electron. Lett.*, vol. 39, no. 8, pp. 676-678, 2003

[181] N. Chi, B. Kozicki, J. Zhang, P. V. Holm-Nielsen, C. Peucheret and P. Jeppesen, "Trans-mission properties of an all-optical labelled signal using orthogonal IM/FSK modulation format", in Proceedings European Conference on Optical Communication, in *Proceedings of ECOC*'03, Rimini, Italy, paper Tu4.4.1 (invited), vol. 2, pp. 300-303, 2003

[182] N. Chi, L. J. Christiansen, P. Jeppesen, I. T. Monroy, P. V. Holm-Nielsen, C. Peucheret, K. Yvind, L. Xu, J. Zhang, “Optical label switching in telecommunication using semicon-ductor lasers, amplifiers and electro-absorption modulators,” in *Laser Optics'03*, paper WeR3-05, St.Petersburg, Russia, 2003

[183] J. Zhang, N. Chi, P. V. Holm-Nielsen, C. Peucheret and P. Jeppesen, "10 Gbit/s Manchester encoded FSK-labelled optical signal transmission link", *Electron. Lett.*, vol. 39, no. 16, pp. 1193-1194, 2003

[184] J. Zhang, N. Chi, P. V. Holm-Nielsen, C. Peucheret and P. Jeppesen, "Performance of Manchester-coded payload in an optical FSK labeling scheme", *IEEE Photon. Technol. Lett.*, vol. 15, no. 8, pp. 1174-1176, 2003

[185] J. Zhang, N. Chi, P. V. Holm-Nielsen, C. Peucheret and P. Jeppesen, "An optical FSK transmitter based on an integrated DFB laser-EA modulator and its application in optical labeling", *IEEE Photon. Technol. Lett*., vol. 15, no. 7, pp. 984-986, 2003

[186] Nan Chi, Christian Mikkelsen, Lin Xu, Jianfeng Zhang, Pablo V. Holm-Nielsen, Haiyan Ou, Jorge Seoane, Christophe Peucheret, and Palle Jeppesen,"Transmission and label en-coding/erasure of an orthogonally labelled signal using a 40 Gb/s RZ-DPSK payload and a 2.5 Gb/s IM label", *Electron. Lett.*, vol. 39, no. 18, pp. 1335-1337, 2003

[187] Nan Chi, Lin Xu, Jianfeng Zhang, Pablo V. Holm-Nielsen, Christophe Peucheret, Chris-tian Mikkelsen, Haiyan Ou, Jorge Seoane, Palle Jeppesen, " Orthogonal optical labeling based on a 40 Gbit/s DPSK payload and a 2.5 Gbit/s IM label", in *Proceedings of OFC*'04, paper FO6, 2004

[188] T. Tsuritani, et al., "70GHz-spaced 40 x 42.7Gbit/s transmission over 8700km using CS-RZ DPSK signal, all-raman repeaters and symmetrically dispersion-managed fiber span", *in Proceedings of OFC'03*, paper PD23, 2003

[189] G. Charlet, et al., "One-hundred WDM-channel transatlantic transmission experiment at 43 Gbit/s using Raman repeaters with large 65 km spacing", *in Proceedings of ECOC'03*, Post deadline paper Th4.3.3, 2003

[190] J. Zhang, P. V. Holm-Nielsen, N. Chi, C. Peucheret and P. Jeppesen, "DC-balanced line encoding for optical labeling scheme using orthogonal modulation", in Technical Digest Optical Fiber Communication Conference, in *Proceedings of OFC*04, Los Angeles, California, U.S.A., paper WF2, 2004

[191] W. Hung, C. Chan, L. Chen, "A novel optical packet labelling scheme using interleaved low-speed DPSK labels," *IEEE Photon. Technol. Lett.*, vol. 16, no. 2, pp. 698-700, 2004

[192] M.C. Ho, C. L. Lu, R. T. Hofmeister, L. G. Kazovsky, "Nonlinear cross-talk reduction by spectrum shaping in subcarrier signalling WDM networks," in in *Proceedings of CLEO'98*, Paper CMG6, 1998

[193] Y. Lin, M. C. Yuang, S. Lee, W. Way, "Using superimposed ASK label in a 10 Gb/s multihop all-optical label swapping system," *J. Lightwave Technol.*, vol.22, no.2, pp.351-353, 2004

[194] J. E. Zucker, K. L. Jones, T. H. Chin, B. Tell and K. Brown-Goebeler, "Strained

quantum wells for polarization-independent electrooptic waveguide switches", *IEEE J. Lightwave Technol.*, vol. 10, no. 12, pp. 1926-1930, 1992

[195] K. Kawano, et al., "4*4 InGaAlAs/lnAlAs MQW directional coupler waveguide switch modules integrated with spot-size converters and their 10 Gbit/s operation", *Electron. Lett.*, vol. 31, no. 2, pp. 96-97, 1995

[196] K. G. Ravikumar, et al., "Switching operation in intersectional type field effect MQW optical switch", *Electron. Lett.*, vol. 24, no. 7, pp. 415-416, 1988

[197] S. Betti, F. Curti, B. Daino, G. De. Marchis and E. Iannone, "State of polarization and phase noise independent coherent optical transmission system based on Stokes parameter detection", *Electron. Lett*., vol. 24, no. 23, pp. 1460-1461, 1988

[198] S. Betti, F. Curti, G. De. Marchis and E. Iannone, "Phase noise and polarization state insensitive optical coherent systems", *IEEE J. Lightwave Technol.*, vol. 8, no. 5, pp. 756-767, 1990

[199] S. Benedetto and P. Poggiolini, "Performance evaluation of multilevel polarization shift keying modulation schemes", *Electron. Lett*., vol. 26, no. 4, pp. 244-246, 1990

[200] S. Betti, F. Curti, G. De. Marchis and E. Iannone, "Multilevel coherent optical system based on Stokes parameters modulation", *IEEE J. Lightwave Technol.*, vol. 8, no. 7, pp. 11271136, 1990

[201] S. Betti and P. Poggiolini, "Theory of polarization shift keying modulation", *IEEE Trans. on Commun.*, vol. 40, no. 4, pp. 708-721, 1992

[202] S. Betti, G. De Marchis and E. Iannone, "Polarization modulated direct diction optical transmission systems", *IEEE J. Lightwave Technol.*, vol. 10, no. 12, pp. 1985-1997, 1992

[203] S. Benedetto and P. Poggiolini, "Multilevel polarization shift keying: Optimum receiver structure and performance evaluation", *IEEE Trans. on Commun.*, vol. 42, no. 2/3/4, pp. 1174-1186, 1994

[204] S. Benedetto, R. Gaudino and P. Poggiolini, "Performance of coherent optical polarization shift keying modulation in the presence of phase noise", *IEEE Trans. on Commun.*, vol. 43, no. 2/3/4, pp. 1603-1612, 1995

[205] S. Benedetto, R. Gaudino and P. Poggiolini, "Direct detection of optical digital transmission based on polarization shift keying modulation", *IEEE J. on Select. Areas on Commun.*, vol. 13, no. 3, pp. 531-542, 1995

[206] R. J. Blaikie, D. P. Taylor and P. T. Gough, "Multilevel differential polarization shift keying", *IEEE Trans. on Commun.*, vol. 45, no. 1, pp. 95-102, 1997

[207] E. Dietrich, B. Enning, R. Gross and H. Knupke, "Heterodyne transmission of a 560 Mb/s optical signal by means of polarisation shift keying", *Electron. Lett*., vol. 23, no. 8, pp. 421-422, 1987

[208] R. Calvani, R. Caponi and F. Cisternino, "Polarization phase-shift keying: A coherent transmission technique with differential heterodyne detection", *Electron. Lett*., vol. 24, no. 10, pp. 642-643, 1988

[209] S. Betti, et al., "Experimental antipotal stokes parameters shift keying transmission system at a laser linewidth exceeding the bit rate", *in Proceedings of ECOC'90*, 1990

[210] S. Benedetto, et al., "Coherent and direct-detection polarization modulation system experiments", *in Proceedings of ECOC'94*, pp. 68-71, 1990

[211] S. Benedetto, et al., "Multilevel polarization modulation using a specifically designed LiNbO3 Device", *IEEE Photon. Technol. Lett*., vol. 6, no. 8, pp. 949-951, 1994

[212] J. J. Lepley, et al., "Excess penalty impairments of polarization shift keying transmission format in presence of polarization mode dispersion", *Electron. Lett*., vol. 36, no. 8, pp. 736-737, 2000

[213] E. S. Hu, et al., "4-Level direct-detection polarization shift keying (DD-PolSK) system with phase modulators", *in Proceedings of OFC'94*, paper FD2, pp. 647-649, 2003

[214] C. W. Chow, C. S. Wong, and H. K. Tsang, "Optical packet labelling based on simultaneous polarization shift keying and amplitude shift keying", *Optics Letters*, vol. 29, no. 16, pp. 1861-1863, 2004

[215] G. Nicholson, and D. J. Temple, "Polarization fluctuation measurements on installed single-mode optical fiber cables", *IEEE J. Lightwave Technol.*, vol. 7, no. 8, pp. 1197-1200, 1989

[216] R. Noé, H. Heidrich, and D. Hoffmann, "Endless polarization control systems for coherent optics", *IEEE J. Lightwave Technol.*, vol. 6, no. 7, pp. 1199-1208, 1988

[217] H. Shimizu, S. Yamazaki, T. Ono, and K. Emura, "Highly practical fiber squeezer polarization controller", *IEEE J. Lightwave Technol.*, vol. 9, pp. 1217-1224, 1991

[218] T. Okoshi, "Polarization-state control schemes for heterodyne or homodyne optical fiber communications", *IEEE J. Lightwave Technol.*, vol. 3, pp. 1232-1237, 1985

[219] F. Heismann and M. S. Whalen, "Broadband reset-free automatic polarization controller", *Electron. Lett*., vol. 27, pp. 377-379, 1991

[220] F. Heismann and M. S. Whalen, "Fast automatic polarization control system", *IEEE Photon. Technol. Lett*., vol. 4, no. 5, pp. 503-505, 1992

[221] M. Tseylin, O. Ritterbush, and A. Salamon, "Digital endless polarization control for polarization multiplexed fiber-optic communications", *in Proceedings of OFC'03*, paper MF83, pp. 103-104, 2003

[222] R. Lewén, S. Irmscher, U. Westergren, L. Thylén, and U. Eriksson, "Travelling-wave electrode electroabsorption modulators toward 100 Gb/s", *in Proceedings of OFC'04*, paper FL1, 2004